Politecnico di Torino

Master of Science in Mechanical Engineering

Adjoint-based optimization of a rib roughened internal cooling channel for gas turbine applications

Candidate: Cristian Pautasso s295041

Supervisors: Prof. Daniela Anna Misul
Prof. Simone Salvadori
PhD. Rosario Nastasi

Academic Year 2024/25

Abstract

Nowadays, gas turbines are among the most widespread energy sources for both energy production and aircraft propulsion. Over the last decades, the turbine has undergone strong improvements in efficiency thanks to the higher turbine inlet temperatures, which easily exceed the material's allowable temperature. Consequently, cooling systems play a key role in protecting the turbine components from high thermal stresses. Rib roughened internal cooling channels are one of the most consolidated cooling technologies in gas turbine blades.
In this context, this activity aims to study the cooling performance of a traditional rib roughened internal cooling channel using numerical CFD simulations. Subsequently, the original channel shape was optimized to improve the wall heat transfer coefficient. During the first step of the activity, numerical results were validated with experiments available in the literature under two different flow conditions (Re=21500, 42000). The effect of the turbulence models and the grid size was estimated by comparing the numerical results of the heat transfer coefficient and friction factor with the experimental correlations. Then, an Adjoint optimization method was adopted to obtain the rib and channel shape that maximizes the convective heat transfer coefficient. Adjoint-based optimization is a class of gradient-based optimization algorithms that uses the so-called adjoint equations to calculate the gradients of the objective functions. This information is later used to deform the mesh in the direction of the optimal solution. In this activity, the optimization was performed on a simplified domain, extracted from the entire channel length, to obtain accurate results with lower computational resources. At the end of the optimization, each rib assumed a unique shape that adapts to the coolant flow to achieve the best thermal performance. The optimized ribs are characterized by a w-shape that promotes the generation of counter-rotating vortices and enhances the fluid interaction with the walls. Moreover, the channel cross-section was also modified, resulting in a further contribution to the optimal cooling performance. The impact of the main geometrical features that emerged during optimization was extensively discussed during a CFD postprocessing step. Finally, the error induced by the mesh deformation was quantified and corrected through a remeshing operation on the optimized geometry.

Acknowledgements

I express my sincere gratitude to my supervisors, Prof. Daniela Misul and Prof. Simone Salvadori, for their guidance and knowledge. I would like to thank my direct supervisor, PhD Rosario Nastasi, who introduced me to this topic and followed me throughout the thesis activity, for his constant support and helpful insights.

An heartfelt thanks to my family and friends. I dedicate this work to my parents for their invaluable support and encouragement.

Contents

List of Figures

List of Tables

1 Introduction

A properly dimensioned cooling system is fundamental in modern gas turbine blades to decrease the metal temperature below the melting point and prevent failure during operation. In fact, the advancement in materials is not sufficient to permit high efficiency, because no existing metal alloy could withstand the extremely high temperatures reached at the turbine inlet without severe damage. The melting point is always lower than the temperature reached by the gases at the turbine inlet, so a proper cooling configuration is required. Especially in the aviation sector, due to strict security regulations, the life of gas turbine components has to be virtually infinite, and safety has to be guaranteed in any flight condition.

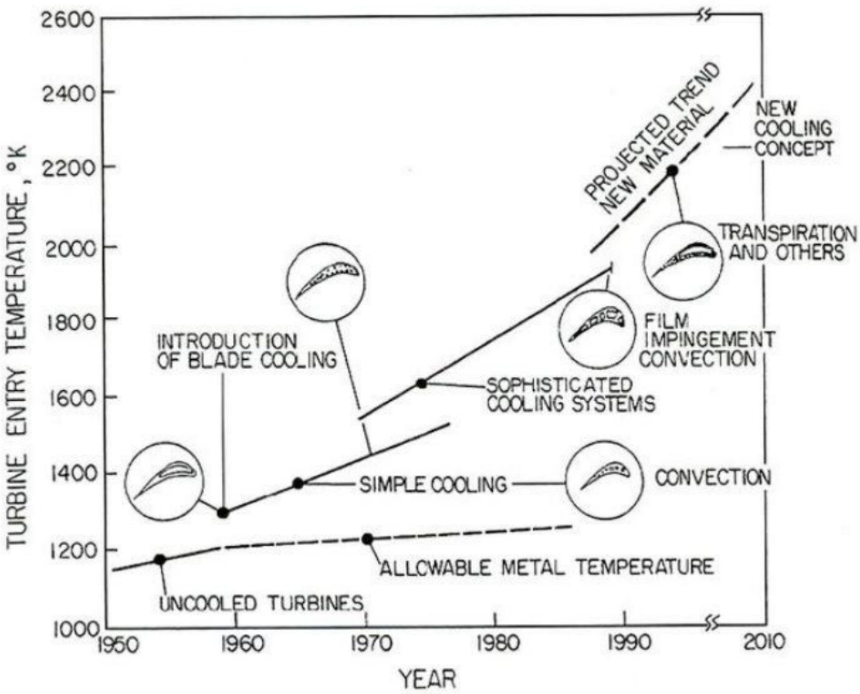

Figure 1.1: Blade temperature evolution and cooling technology development through the years [2]

In Figure 1.1, the evolution of the turbine inlet temperature over the years is shown; it has exponentially increased from 1300 K in 1960 to about 2000 K and more nowadays. Meanwhile, the allowable metal temperature has increased very slightly as a consequence of the intrinsic limit of the materials. Therefore, new cooling systems have been studied to compensate for this gap.
One of the most consolidated cooling methods is internal cooling, which consists of designing internal channels inside the blade where a flow of air exports heat from the blade surface in contact with hot gases from the combustor outlet. In this activity, the focus is on the rib roughened internal cooling.
In the literature, many authors have studied this particular technology since the 1970s. Han et al. [3-4] considered a straight channel with smooth walls and studied heat transfer and friction factor, which is an index of pressure loss. The channel walls were then roughened by placing square ribs in two opposite walls. This resulted in

an enhancement of heat transfer and an even larger increase in friction losses. In the following years, more geometries and configurations of the ribs were investigated, different rib shapes and orientation angles relative to the main flow.
Ribbed channels provide better heat transfer by means of the generation of secondary flows and eddies near the walls. These eddies increase convection by slowing and keeping the coolant near the walls for a longer time span, but at the same time are an obstacle to the main flow. Therefore, it is important to examine several configurations to find the best trade-off between heat transfer and pressure loss. Pressure losses need to be limited for downstream film cooling, because air from the internal channels is often regulated to exit from film cooling holes, thus providing a film in the blade external surfaces. The protective film must be attached to the external surface of the blade to prevent direct contact with hot gases; for this reason, the coolant must maintain sufficient pressure.

1.1 Thermodynamic cycle and efficiency

The classical configuration of a gas turbine power plant or engine consists of: a compressor, where the air enters from the external environment and it is brought at a higher pressure; a combustor, where the compressed air is mixed with fuel, the combustion happens and the resulting gases have high energy in thermal form; a turbine where the thermal energy of the hot gases from the combustor is transformed into kinetic energy in order to thrust an airplane in a gas turbine engine or the kinetic energy is further transformed into electric energy with a generator in a gas turbine power plant. The general scheme is shown in Figure 1.2.

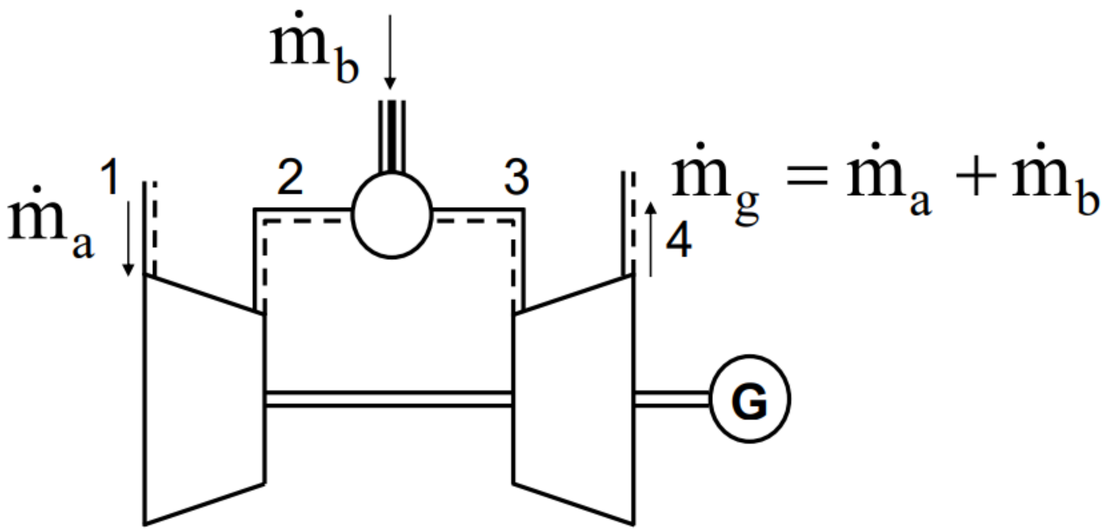

Figure 1.2: Schematic of the classic version of a gas turbine. $\dot{m}_a$ is the air mass flow rate, $\dot{m}_b$ or $\dot{m}_f$ is the fuel mass flow rate, and $\dot{m}_g$ is the burned gases mass flow rate

Generally, in gas turbine power plants and gas turbine engines, the goal is to reach the ideal Brayton-Joule cycle to have the highest efficiency and power output. But in reality losses of different types are unavoidable, for example heat dissipation and pressure losses. The cycle efficiency and power output are strictly dependent on the turbine inlet temperature T_3: generally the higher T_3, the higher the engine efficiency and power output. For this reason, over the years the turbine inlet temperature has increased drastically.

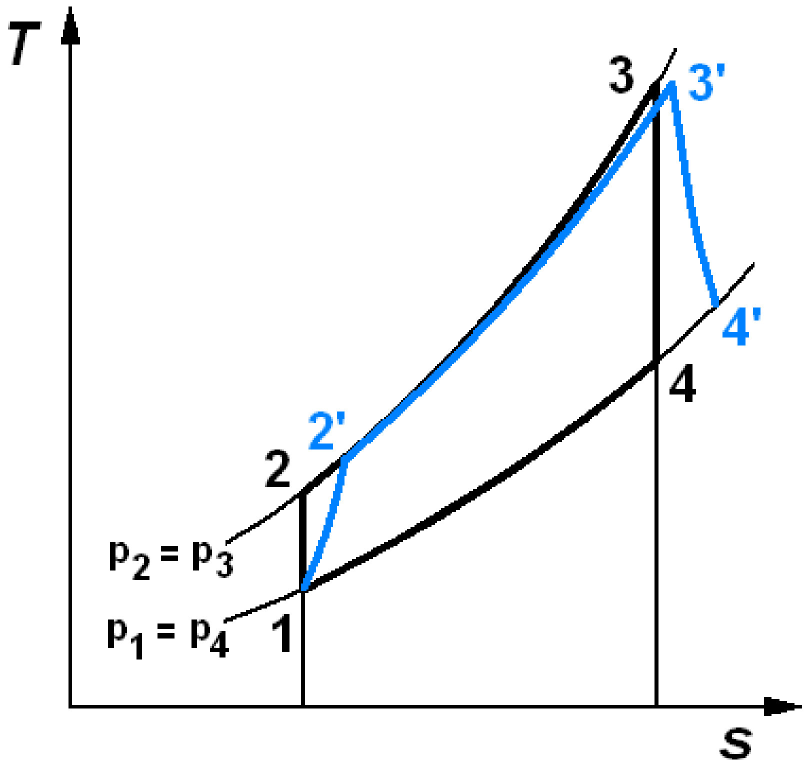

Figure 1.3: Brayton-Joule cycle in T-s diagram, ideal (black) and real case (blue)

As seen in Figure 1.3, the ideal cycle has four phases:

- 1-2 isentropic compression
- 2-3 heat introduced at constant pressure
- 3-4 isentropic expansion
- 4-1 heat removed at constant pressure

The real cycle is not a closed cycle, as the ideal cycle, but an open cycle because the fluid exits the turbine at point 4, and a new fluid is introduced at point 1. The compression and the expansion, 1-2' and 3'-4' respectively, are not isentropic in the real cycle, because there are heat losses and the entropy rises. The real point 3' at the end of the combustion is not coincident with the ideal point 3 for the pressure drop that occurs in the combustor.
The net power output is

$$P_u = \eta_0(P_{i,t} - P_{i,c})$$

where η_0 is the organic efficiency, $P_{i,t}$ is the power generated by the turbine and $P_{i,c}$ is the power requested by the compressor. Expressing the power the equation becomes:

$$P_u = \eta_0(\dot{m}_g L_t - \dot{m}_a L_c)$$

$$P_u = \dot{m}_a \eta_0 (\frac{1+\alpha}{\alpha} L_t - L_c)$$

where $\dot{m}_a$ is the air mass flow rate, $\dot{m}_g$ is the mass flow rate of the burned gases, L_t is the specific work of the turbine, L_c is the specific work of the compressor, $\alpha = \frac{\dot{m}_a}{\dot{m}_f}$ is the air fuel ratio.
The useful work can be defined as

$$L_u = \eta_0 (\frac{1+\alpha}{\alpha} L_t - L_c)$$

Then $P_u = \dot{m}_a L_u$.
The global efficiency of the plant can be calculated as:

$$\eta_g = \frac{P_u}{\dot{m}_f H_i}$$

where $\dot{m}_f$ is the fuel mass flow rate and H_i is the lower heating value of the fuel.
The turbine work can be expressed as:

$$L_t = \eta_t c'_p T_3 (1 - \frac{1}{\beta_t^{\frac{k'-1}{k'}}}) = c'_p T_3 (1 - \frac{1}{\beta_t^{\frac{k'-1}{k}\eta_{yt}}})$$

where η_t is the isentropic efficiency of the turbine, η_{yt} is the hydraulic efficiency of the turbine, T_3 is the turbine inlet temperature, $\beta_t = \frac{p_3}{p_1}$ is the expansion ratio and k' is the adiabatic coefficient of the burned gases.
The compressor work is:

$$L_c = \frac{1}{\eta_c} c'_p T_1 (\beta_c^{\frac{k-1}{k}} - 1) = c'_p T_1 (\beta_c^{\frac{k-1}{k}\frac{1}{\eta_{yc}}})$$

where η_c is the isentropic efficiency of the compressor, η_{yc} is the hydraulic efficiency of the compressor, T_1 is the air temperature at the compressor inlet, $\beta_c = \frac{p_2}{p_1}$ is the compressor ratio and k is the adiabatic coefficient of the air.
The previous equations highlights that:

$$L_u = L_u(\beta_c, T_3)$$

and

$$\eta_g = \eta_g(\beta_c, T_3)$$

These dependencies are clearer in Figures 1.4, 1.5 and 1.6. Generally, the value of β_c cannot overcome a threshold of about $40 \div 50$ to obtain a proper cycle efficiency; in fact, the real cycle efficiency curve has two zero points at the extremes and a relatively flat region in the middle, where its value remains nearly constant with the variation of the compressor ratio β_c. Most gas turbine plants operate in this range of β_c. Meanwhile, the net work L_u has a maximum for a lower value of β_c than the global efficiency, then it decreases until it reaches zero. For this reason, the compressor ratio β_c cannot be chosen too high to not penalize L_u.

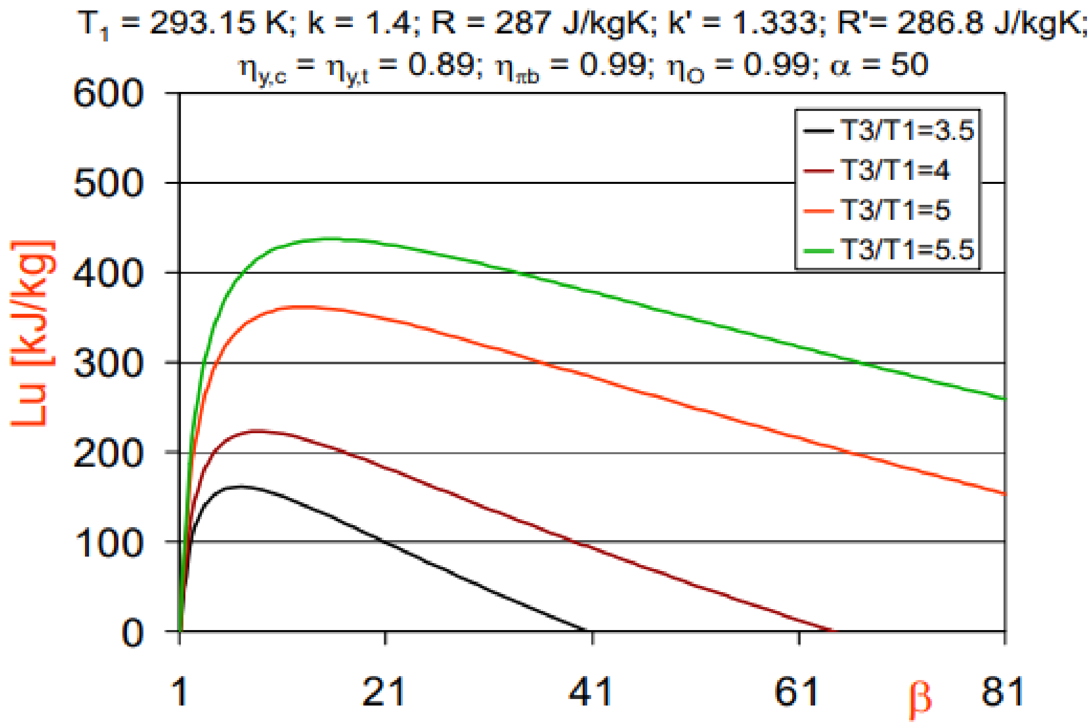

Figure 1.4: L_u dependence on the compressor ratio and turbine inlet temperature

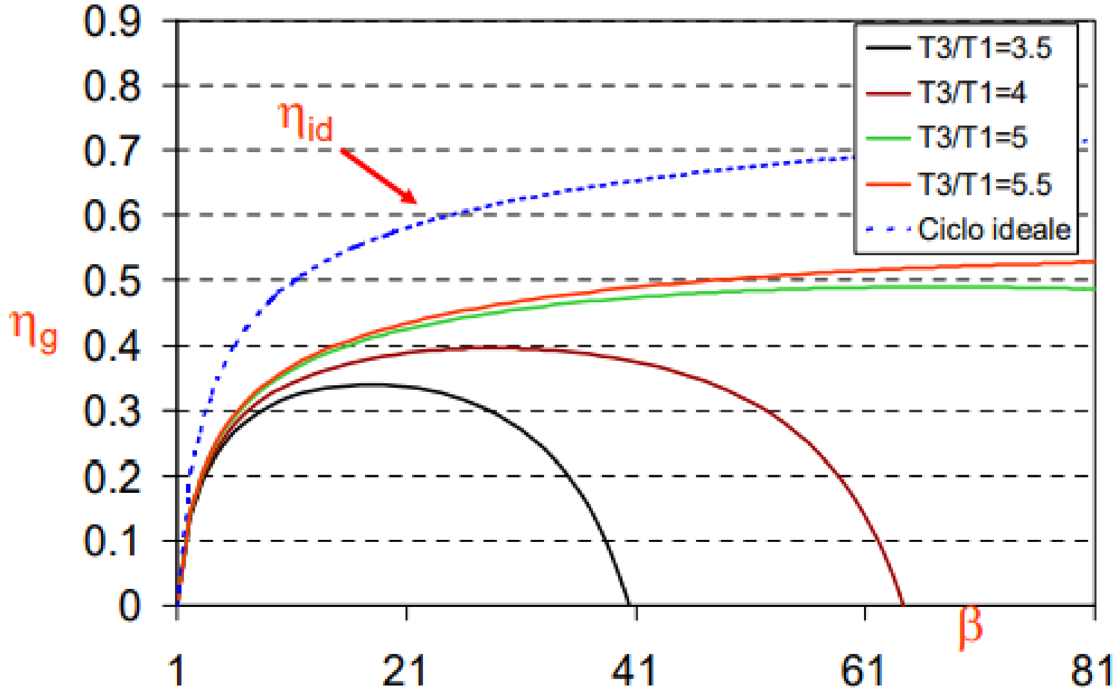

Figure 1.5: η_g dependence on the compressor ratio and turbine inlet temperature

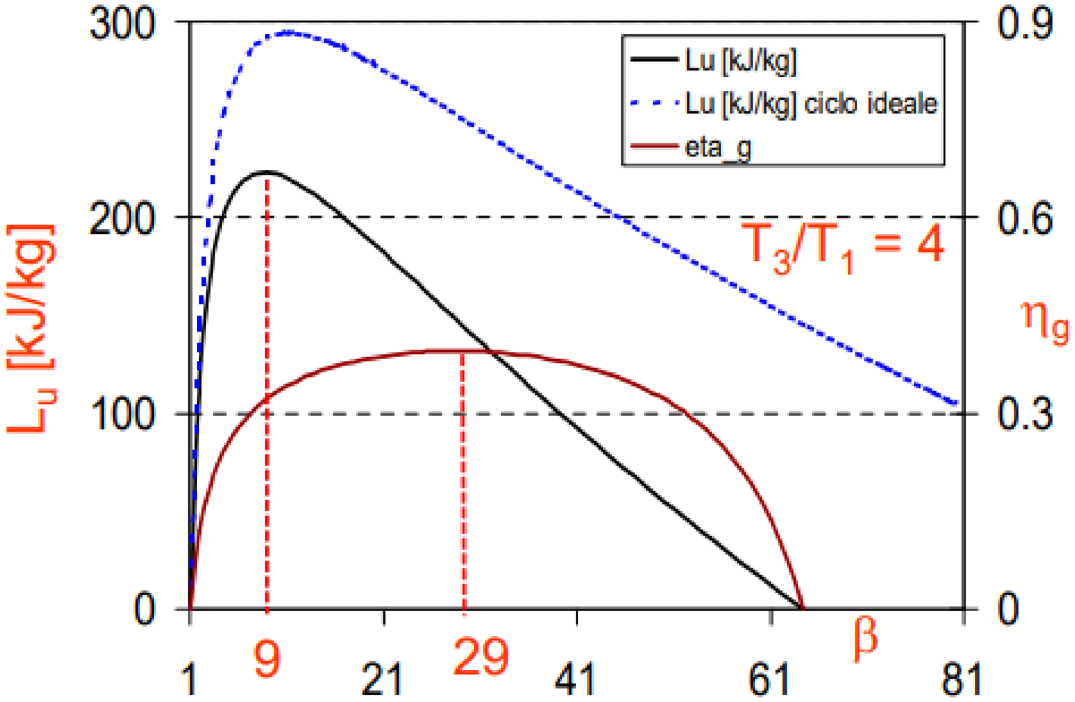

Figure 1.6: Compressor ratio trade-off between maximizing L_u and η_g

2 Cooling of turbine blades

In the last decades, the research has almost reached a plateau in the increase of the turbine inlet temperature at the inlet of the turbine vane, and consequently efficiencies cannot be improved anymore with large percentage variations. In order to reach higher efficiencies, blade materials and cooling techniques are studied extensively, and the rising in gas temperature over the years has led designers and researchers to develop new cooling systems to reduce the blade temperature below the melting point. To avoid premature failure, engineers must accurately identify the local hot spots on the blade and the temperature gradients. The cooling techniques for gas turbines can be divided into two great categories:

- external cooling (or film cooling)
- internal cooling

2.1 Film cooling

External cooling is most commonly known as film cooling. It is performed by introducing holes in the blade leading edge. The coolant enters the blade from the airfoil root, then exits from holes in the external surface of the blade and creates a film around the blade. This thin film isolates the blade surface from the hot gases that flow from the combustor through the turbine stages. A simple scheme is shown in Figure 2.1.

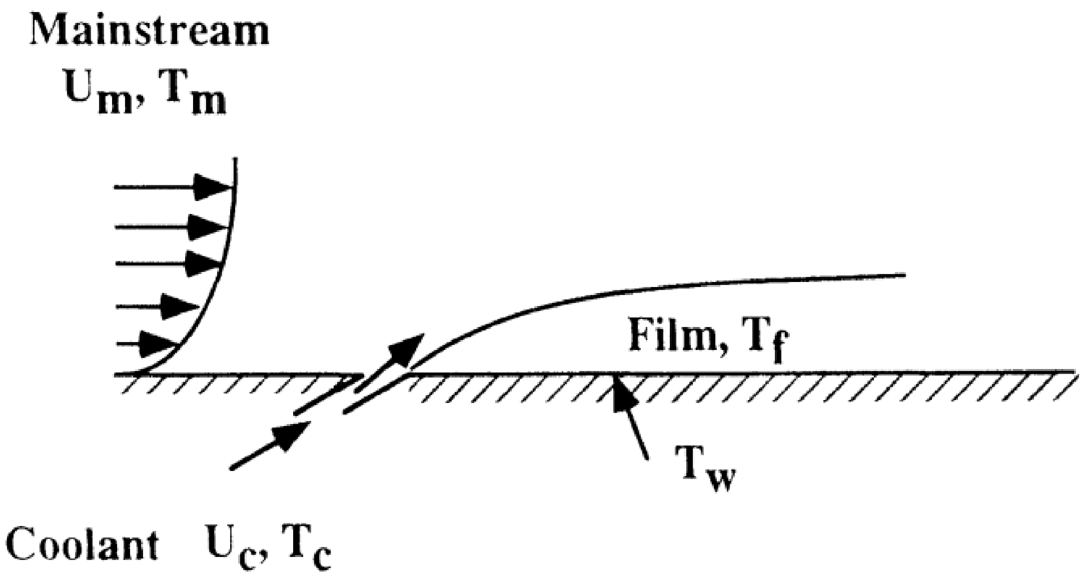

Figure 2.1: Schematic of film cooling, the protective film is generated downstream the hole exit [5]

The main parameters are: coolant to hot mainstream pressure ratio; temperature ratio; film hole size, location and configuration relative to the mainstream. These parameters are optimized to reach the best film cooling effectiveness under engine operating conditions. The objective is to achieve the highest cooling effectiveness with the lowest penalty on the thermodynamic cycle efficiency. For example, the higher the coolant to hot mainstream pressure ratio, the higher the film cooling effectiveness; but increasing too much the pressure ratio could lead to jet penetration into the hot gases, therefore the jet separation from the blade external surface.

2.2 Internal cooling

One of the most diffused cooling methods is internal cooling, which is achieved by a cold fluid, usually air at lower temperature spilled from the compressor stages, which flows through channels obtained inside the blade. The convective heat transfer between the air and the blade metal reduces the metal temperature and maintains it below its melting point, thus preventing the failure of the component due to high thermal stresses.
Internal cooling is obtained with different strategies (as shown in Figure 2.2), depending on the three different blade zones: leading edge, middle region and trailing edge. Rib roughened internal channels are realized in the middle portion because the transversal area is larger than in the leading edge and trailing edge, so it allows adequate heat exchange. The ribs are always placed on the internal face of the pressure and suction sides of the blade, which are in contact with the hot gases, so the heat transfer is amplified because of the higher temperature gradients. Instead, in the leading edge and trailing edge different technologies are implemented to achieve the best thermal exchange in accordance with the geometry limitations, for example pin fins in the trailing edge. In the following paragraphs, a brief description of the main internal cooling technologies adopted for gas turbine blades is presented.

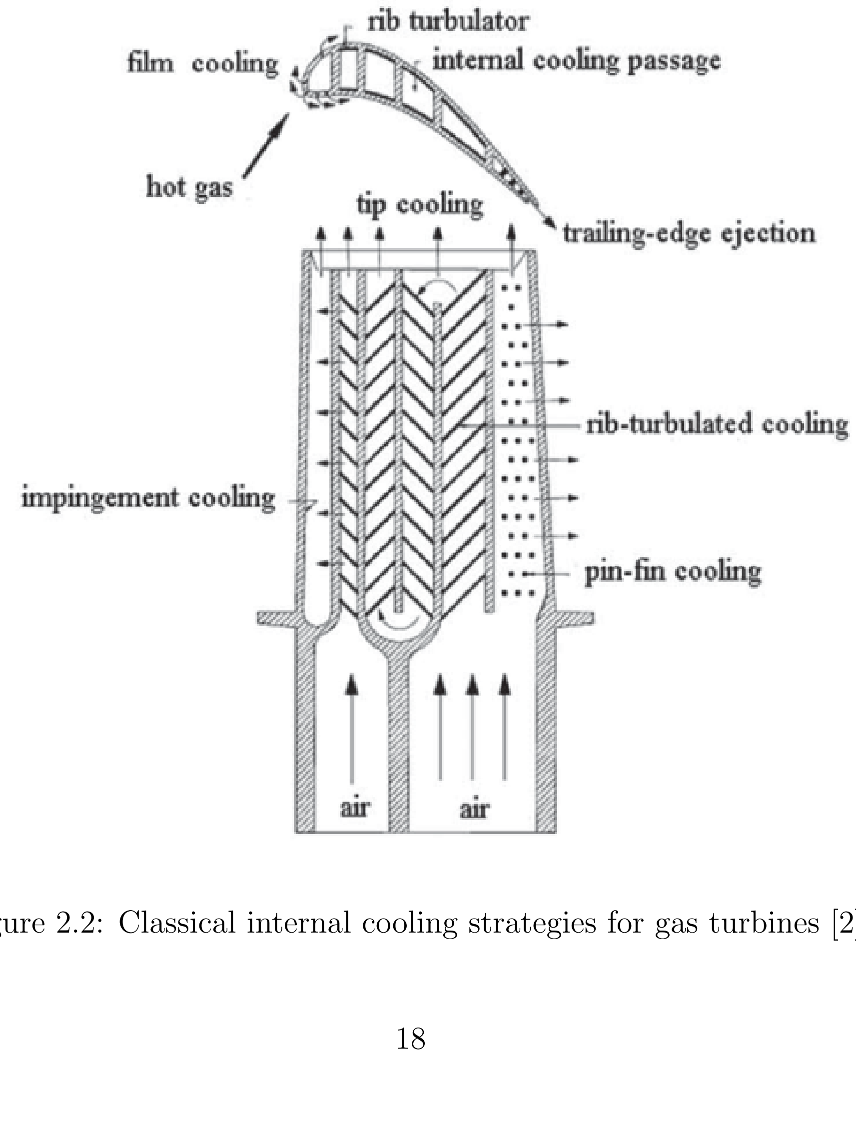

Figure 2.2: Classical internal cooling strategies for gas turbines [2]

2.2.1 Impingement cooling

Impingement cooling is the technique of ejecting a fluid onto a surface to heat or cool it. The jet can be singular or multiple jets can be realized with a more complex design. The impingement jets exit from the inner blade body and impinge on the inner surface of the outer blade body. Figure 2.3 shows a brief visualization. This solution is useful in limited regions at very high temperature; the jet is directed to the zones at hot temperature where the risk of failure is greater. It is important to contrast hot spots on the blade and maintain even temperature across it in order to avoid excessive temperature gradients that lead to thermal stresses. Generally, the leading edge of the blade is subject to higher temperatures; especially near the stagnation point, impingement cooling is required. Furthermore, this type of cooling is not realizable in other portions of the blade for structural problems, because the regions thinner in section cannot have holes with large diameter.

Impingement cooling is more effective in a confined space, it is widely used to cool combustor liners and high-pressure turbine stages, in particular for first-stage vanes. The main parameters of this cooling method are: impinging jet Re number; hole size and distribution; cooling channel cross section; target surface extension and shape; jet-to-target distance; spent air cross-flow interaction with the jet in the multiple jet design. These parameters are optimized to reach the best cooling efficiency; for example, the jet-to-target distance needs to be neither too small nor too large to be effective.

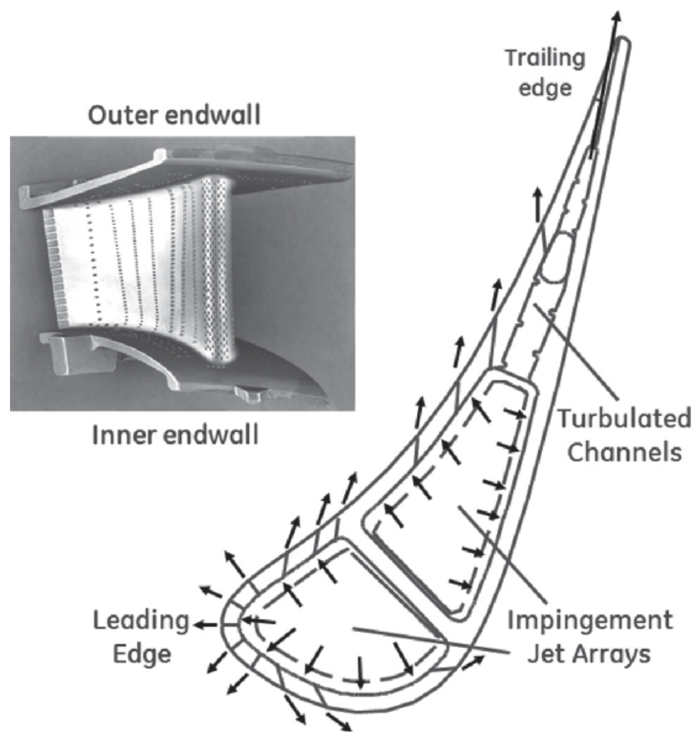

Figure 2.3: Impingement cooling is used mainly at the vane/blade leading edge, where the temperature are higher [1]

2.2.2 Pin-fin cooling

Pin-fin cooling is used exclusively at the trailing edge of the turbine blade, where other methods are not feasible due to the restricted section. Pin fins are pin-shaped protrusions that are realized in the trailing edge of the blade to promote heat transfer between the coolant and the hot gases by increasing the heat exchange area and flow turbulence. Generally, multiple fins are placed on the inner walls of the trailing edge as an array with a studied distribution to increase heat transfer. Pin fins are usually cylindrical, but other shapes have also been used, such as cube-shaped and diamond-shaped pins.

2.2.3 Rib turbulated cooling

Rib turbulated cooling is an effective way to improve heat transfer in the blade internal channels. Ribs can have various shapes from the simple rectangular section to the more complex shapes.
The shape of internal channels is often an U-bend, which is proven in the literature to have a higher heat exchange area compared to a straight channel. In recent decades, the channel shape has been optimized, in particular the region of the U-bend. In addition, the channels have been reinforced by ribs to promote recirculating flows near the walls that augment heat exchange between the coolant and the hot gases. In the literature, most researchers use a simplified straight channel reinforced with ribs to study their effects on thermal performance and friction loss. The objective is to obtain a good trade-off between a better heat transfer and a not much sensible friction loss enhancement.

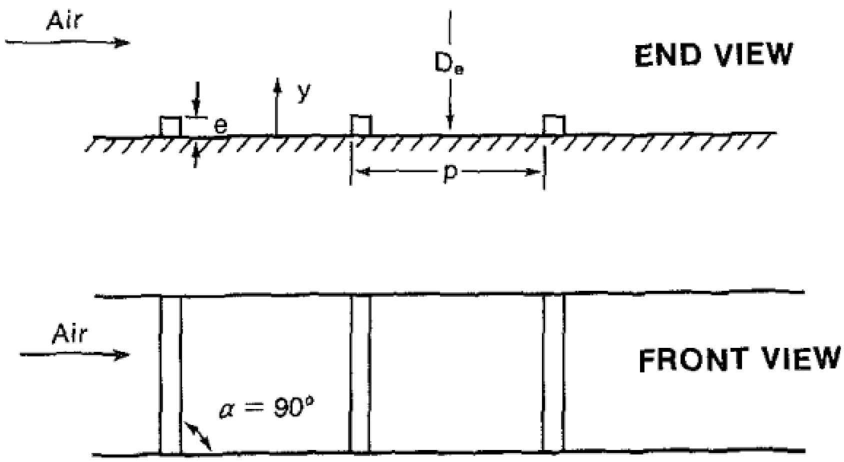

Figure 2.4: Rib geometry parameters [3]

Firstly, in the 1970s researchers began to experimentally evaluate the effects of ribs in straight channels with a square or rectangular section. Empirical correlations for heat transfer performance and friction loss have been developed and validated.
The simplest rib shape is a parallelepiped with a rectangular or square section. However, over the years, many new shapes have been proposed and studied in order to improve the heat exchange and limit the pressure loss. The main parameters of the ribs are the following:

- $\frac{e}{D_h}$ rib height to hydraulic diameter ratio
- $\frac{p}{e}$ rib pitch to rib height ratio
- α rib angle relative to the main flow

The downside of this cooling technology is the increase in pressure loss. The pressure of the coolant has to be quite high to guarantee the film cooling effectiveness, in fact the coolant after passing the internal channel exits from film cooling holes and creates a film over the blade external surface. If the air pressure is not sufficiently high, the insulation film is broken by the main stream and hot gases could come into contact with the blade and create severe damage. Therefore, the design process is a trade-off between increasing heat transfer and limiting the pressure drop across the channel.

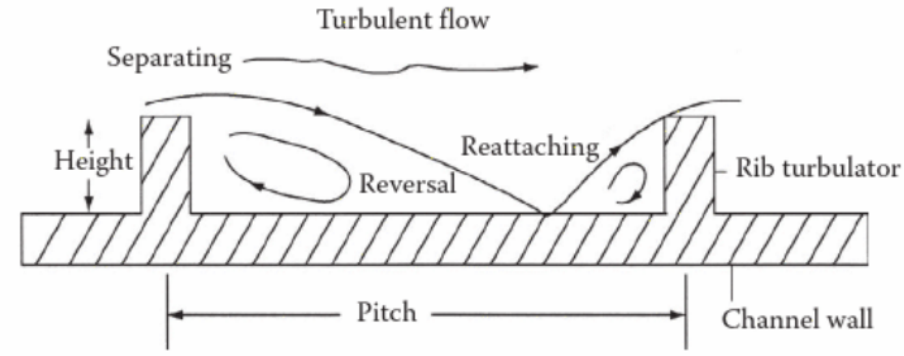

Figure 2.5: Scheme of the rib effects on the boundary layer [2]

As shown in Figure 2.5, the presence of ribs causes flow separation near the ribbed walls. Considering a pitch between two ribs, after the first rib a recirculating zone is generated, then at a certain distance the secondary flow reattaches with the main flow. The disturbed boundary layer improves the turbulent mixing and, therefore, the heat transfer coefficient.
In the next page, the rib shapes and configurations studied by Han et al. are reported in Figure 2.6.

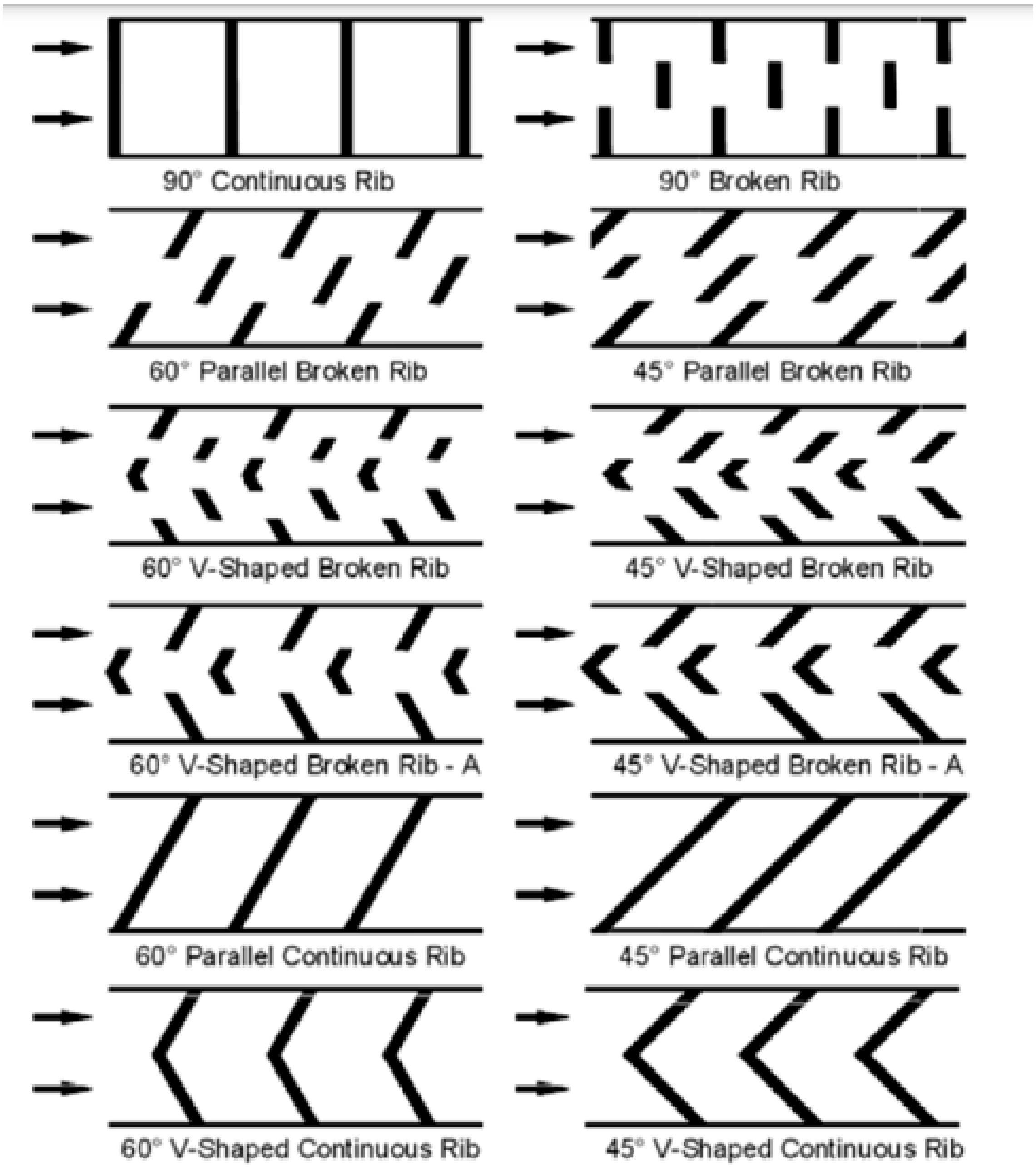

Figure 2.6: Different rib shapes and configurations studied by Han et al. [2]

3 Literature review on rib roughened cooling

3.1 Heat transfer

In internal cooling design, the predominant heat transfer mechanism involved is convection. It is heat transported by a fluid in movement; when a portion of fluid is in contact with a hot source, its temperature increases and the density reduces; in this way the fluid tends to move to regions at higher densities.
In experimental tests and numerical results, heat transfer is often described with dimensionless numbers, such as Nusselt and Stanton numbers. Their values correctly represent the heat transfer intensity because they are proportionally dependent.
The Nusselt number is expressed as:

$$Nu = \frac{hD_h}{\lambda} \tag{1}$$

where h, also called HTC, is the convective heat transfer coefficient, D_h is the hydraulic diameter of the channel and λ is the thermal conductivity of the fluid.
The Stanton number can be obtained as:

$$St = \frac{h}{c_p \rho v} \tag{2}$$

where c_p is the specific heat capacity at constant pressure, ρ is the density of the fluid and v is the mean velocity magnitude of the fluid.
Convective heat transfer coefficient is defined as:

$$h = \frac{\dot{q}}{(T_w - T_a^0)} \tag{3}$$

where $\dot{q}$ is the heat flux, T_w is the wall temperature and T_a^0 is the total temperature of the air.

3.2 Experimental correlations

3.2.1 Friction factor

As studied by Han et al. in their works [3-4], the friction factor for four-sided smooth duct can be obtained by iterating from the following equation imposing that the value of f_s the left and right sides must be equal:

$$\frac{1}{\sqrt{f_s}} = 4.0 \log_{10}(Re_{De}\sqrt{f_s}) - 0.40 \tag{4}$$

The friction factor for the four-sided ribbed duct can be calculated as follows:

$$f_r = \frac{2}{[0.95(\frac{P}{e})^{0.53} - 2.5 \ln \frac{2e}{D_e} - 2.5 - 2.5 \ln \frac{2B}{A+B}]} \tag{5}$$

where A and B are the width and height of the channel, in this study the channel is perfectly square so A=B=7.6 cm. P is the rib pitch and e the rib height. D_e is the hydraulic diameter.

Then, the friction factor for a two-sided ribbed duct is found from the weighted average of the four-sided smooth duct friction factor f_s and the four-sided ribbed duct friction factor f_r.

$$f = \frac{Af_s + Bf_r}{A + B} \tag{6}$$

3.2.2 Thermal correlations from Han 1984

In the article by Han published in 1984 [3], the thermal exchange is represented by the Stanton number. The Stanton number in a four-sided smooth duct is determined by the modified Dittus-Boelter correlation.

$$St_s = \frac{0.023}{Re_{D_e}^{0.2} Pr^{0.6} (2R_{av}/D_e)^{0.2}} \tag{7}$$

where R_{av} is the average ray length of the duct, $2R_{av}/D_e = (1.156+B/A-1)/(B/A)$. In a square section, as in this case, $A = B = D_e$, then $2R_{av}/D_e = 1.156$. $Pr = 0.71$ is the Prandtl number.
The Stanton number in a four-sided ribbed duct can be obtained by:

$$St_r = \frac{f_r/2}{1 + \sqrt{f_r/2}[G_h(e^+, Pr) - R_M(e^+)]} \tag{8}$$

where $G_h(e^+, Pr)$ and $R_M(e^+)$ are correlations from previous literature works.

$$G_h(e^+, Pr) = 4.5(e^+)^{0.28} Pr^{0.75}; e^+ \geq 25 \tag{9}$$

for all configurations and Reynolds numbers tested in this work, the condition $e^+ \geq 25$ is always satisfied.

$$R_M(e^+) = \sqrt{\frac{2}{f_r}} + 2.5 \ln \frac{2e}{D_e} + 2.5 \ln \frac{2B}{A+B} + 2.5 \tag{10}$$

The average Stanton number is defined by:

$$\overline{St} = \frac{ASt_s + BSt_r}{A + B} \tag{11}$$

3.2.3 Thermal correlations from Han 1985

In another article by Han et al. (1985) [4], the correlations for the Stanton number differ from the previous.
The average Stanton number can be found by combining the following two equations:

$$\overline{H}(\overline{e}^+, Pr) = \overline{R}(\overline{e}^+) + [\overline{f}/(2\overline{St}) - 1]/(\overline{f}/2)^{1/2} \tag{12}$$

$$\overline{H}(\overline{e}^+) = 3.47(\alpha/90\ deg)^{0.3}(\overline{e}^+)^{0.28} \tag{13}$$

where

$$\overline{R}(\overline{e}^+) = (2/\overline{f})^{1/2} + 2.5 \ln 2e/D + 2.5 \tag{14}$$

and α is the orientation angle of the rib relative to the main flow.

The Stanton number for a four-sided ribbed duct is obtained in an equivalent way by equaling the equations:

$$H_R(\overline{e}^+, Pr) = \overline{R}(\overline{e}^+) + [\overline{f}/(2St_R) - 1]/(\overline{f}/2)^{1/2} \tag{15}$$

$$H_R/(P/e/10)^{0.14} = 2.83(\alpha/90)^{0.3}(\overline{e}^+)^{0.28} \tag{16}$$

After calculating $\overline{St}$ and St_R, the Stanton number in a four sided smooth duct is given by:

$$St_s = 2\overline{St} - St_R \tag{17}$$

The difference between the 1984 correlation and the 1985 ones is that in the latter the influence of the adjacent ribbed wall on the smooth wall is taken into account. The correlations from 1985 better represent real experimental results, because the smooth walls near ribbed walls have improved thermal heat exchange compared to smooth walls in a four-sided smooth duct.

3.3 Navier-Stokes equations

The Navier-Stokes equations describe how the velocity, pressure, temperature and density of a fluid in motion are related. They are the fundamental equations of fluid dynamics.

$$\frac{\partial \rho}{\partial t} + \frac{\partial}{\partial x_i}(\rho u_i) = 0 \tag{18}$$

$$\frac{\partial(\rho u_i)}{\partial t} + \frac{\partial}{\partial x_j}(\rho\ u_i u_j) = -\frac{\partial p}{\partial x_i} + \frac{\partial}{\partial x_j}[\mu(\frac{\partial u_i}{\partial x_j} + \frac{\partial u_j}{\partial x_i})] - \frac{2}{3}\frac{\partial}{\partial x_i}(\mu\frac{\partial u_k}{\partial x_k}) \tag{19}$$

$$\frac{\partial(\rho E)}{\partial t} = \frac{\partial(\rho E u_j)}{\partial x_j} + \frac{\partial q_i}{x_j} = \rho F_j u_j + \frac{\partial(\tau_{ij} u_j)}{\partial x_j} + S_q \tag{20}$$

In order continuity equation, momentum equation and energy equation. In order to solve the Navier-Stokes equations in a real domain, they are averaged in time considering that the quantities consist of an average value plus a fluctuating part. After applying the Reynolds average, the equations are transformed in the RANS equations (Reynolds-averaged Navier-Stokes equations):

$$\frac{\partial \rho}{\partial t} + \frac{\partial}{\partial x_i}(\rho\overline{u_i}) = 0 \tag{21}$$

$$\frac{\partial}{\partial t}(\rho\overline{u_i}) + \frac{\partial}{\partial x_j}(\rho\overline{u_i}\overline{u_j}) = -\frac{\partial\overline{p}}{\partial x_i} + \frac{\partial}{\partial x_j}(\overline{\tau_{ij}} - \rho\overline{u_i' u_j'}) \tag{22}$$

The last term $\rho\overline{u_i' u_j'}$ does not allow for the direct solution of the equations because there are more unknowns than equations. Therefore, to overcome this problem, there are two different approaches, which are described later.
In recent years, the use of computational fluid dynamics (CFD) has reached rapid diffusion worldwide. This resource is useful to obtain more test cases in the most disparate cases and with different boundary conditions. With the help of CFD results, only a limited amount of real equipment needs to be tested experimentally because the software can give the right search direction for designing machines. In this way, only the selected configurations are tested experimentally.

In most cases in industry and university, the RANS method is used, because its computational burden is acceptable and much less than in the case of LES and DNS methods.
With RANS only the integral scale of turbulence is solved, meanwhile the inertial and Kolmogorov scales are modeled. In most detailed cases, the LES method is used to reach better accuracy, it solves the integral and inertial scales, and it models the Kolmogorov scale. The most expensive method is DNS, which solves all the scales down to the smaller scales, but today this is still difficult to realize in most cases due to limited computational resources.

3.4 Turbulence

Turbulence is a complex phenomenon, which is very difficult to model due to its randomness and small dimension of the dissipation scales. Due to its nature, turbulence cannot be described with a deterministic approach, but only with statistical methods. It can be defined as the sum of an average term and a fluctuation term.

$$u = \bar{u} + u' \tag{23}$$

Turbulence is intrinsically a 3D phenomenon characterized by disorder, the velocity fluctuations are casual and this is clear due to the fact that even testing the same case with the same initial conditions the output flow will never be exactly the same locally. Instead, the averages remain stable and regular, so a statistical approach is much more useful.
Turbulence consists of eddies of different dimensions and energy levels. Larger eddies have length scale l_0, called the integral scale of turbulence, which is comparable to the main flow length scale L. Moreover, the velocity of the larger eddies u_0 is of the same order of the flow velocity U and the velocity fluctuation u'. The smallest scale, where dissipation occurs, is called the Kolmogorov scale δ, by the name of the physicist who theorized it. In Figure 3.1, the different scales of turbulence are reported.

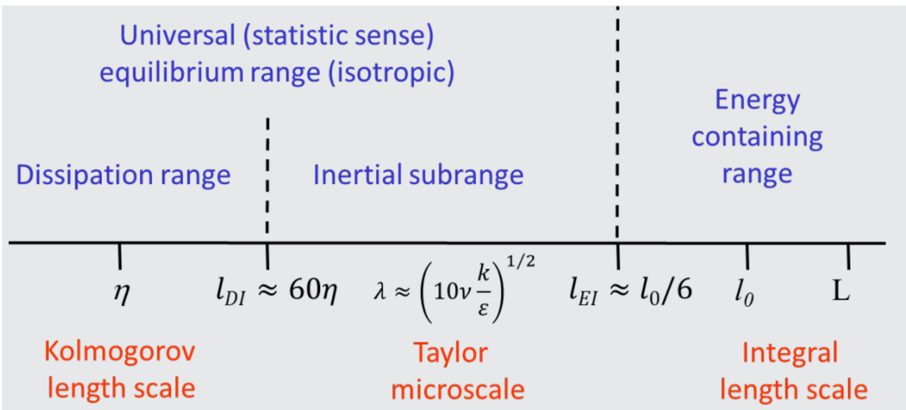

Figure 3.1: Eddies scales classified by Kolmogorov

The two characteristic quantities that describe turbulence are the turbulent kinetic energy k and the energy dissipation rate $[m^2/s^3]$. The turbulent kinetic energy is expressed as:

$$k = \frac{1}{2} < u_i u_i >= \frac{1}{2}(\overline{u'}^2 + \overline{v'}^2 + \overline{w'}^2) \tag{24}$$

The mechanism with which energy is transferred from larger to smaller eddies is known as the energy cascade (Figure 3.2). The bigger eddies split up and transfer energy to the smaller eddies, which split up in turn. This mechanism propagates itself until the viscous scale, where the viscous effects are dominant upon the inertial effects. Dissipation occurs on the smallest scale, where the kinetic energy is transformed into heat.
The energy distribution between various eddies scales is given by the turbulence spectrum. The larger eddies contain the major quote of energy, they have a smaller velocity and they split up to convey energy to smaller eddies, which are faster.

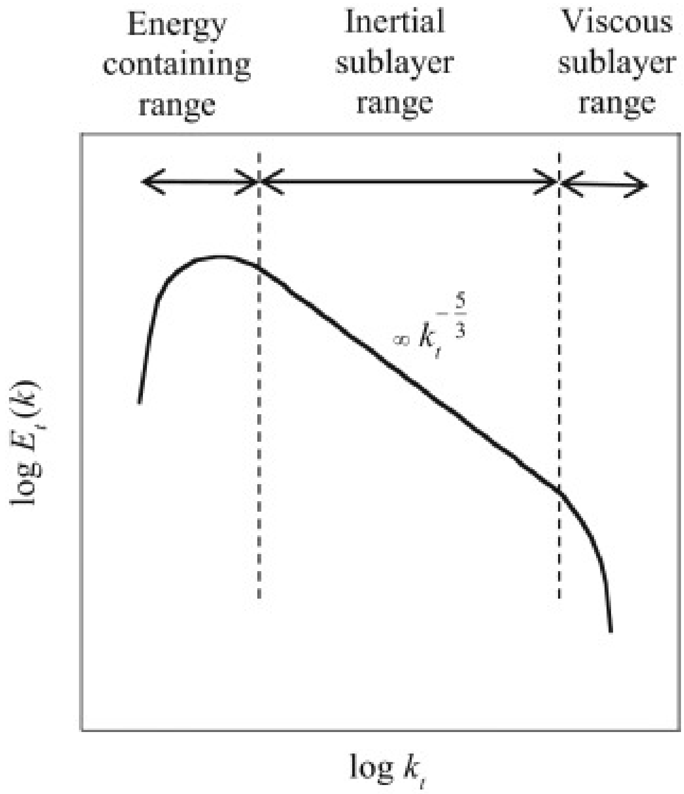

Figure 3.2: Energy spectrum $E(\kappa)$

3.5 Turbulence models

In CFD analysis, one of the most important choices to correctly model the flow behaviour near walls and ribs is the turbulence model. Over the years, several different types of turbulence models have been proposed. In this work, the models studied are: Standard $k-\omega$, SST $k-\omega$, Realizable $k-\epsilon$, RNG $k-\epsilon$ and Reynolds Stress Model.

The simplest models are the eddy viscosity models, such as the $k-\epsilon$ model and the $k-\omega$ model. There are two different types of turbulence models:

- eddy-viscosity models
- Reynolds stress models

The eddy viscosity models calculate turbulent viscosity through the Bousinnesq hypothesis; they are implemented in a CFD simulation to address the viscosity effects

lost in averaging the turbulence effects. The most common eddy viscosity models are two equations models. Two transport equations of two scalar quantities are written: one transport equation for the turbulence kinetic energy and one transport equation for dissipation effects. The dissipation of the turbulent kinetic energy can be represented by a dissipation rate ϵ in the $k-\epsilon$ model or a specific dissipation rate $\omega = \epsilon/k$ in the $k-\omega$ model.
The two transport equations permit the closure of the RANS (Reynolds Averaged Navier-Stokes) equations. Indeed, after obtaining values of turbulent kinetic energy and dissipation, they are used to calculate the turbulent eddy viscosity and finally the Reynolds stress term, whose terms were unknown in the RANS equations. Reynolds stress models do not rely on the Bousinnesq hypothesis to simplify the Reynolds stress tensor; instead, they calculate every element of the tensor directly. Therefore, each term of the Reynolds stress tensor has its own transport equation, which can lead to an increase in computational time and resources needed. The reward is the accuracy of the results near the walls and the boundary layer development. Reynolds stress models account for the anisotropy of the turbulent flow near flows. In computational procedures, a trade-off between accuracy and computational burden is often considered. In the following paragraphs, the turbulence models used in this work are briefly presented; for a more complete description, the Ansys manual can be consulted [7].

3.5.1 Standard k-ϵ model

In the derivation of the $k-\epsilon$ model, the hypothesis is that the effects of molecular viscosity are negligible; therefore, the flow is fully turbulent and the model is only valid for fully turbulent cases. For this reason, the $k-\epsilon$ model is suitable for the free-shear layer flows far from the walls. The Standard k-ϵ model is represented by the following two transport equations.

$$\frac{\partial}{\partial t}(\rho k) + \frac{\partial}{\partial x_i}(\rho k u_i) = \frac{\partial}{\partial x_j}[(\mu + \frac{\mu_t}{\sigma_k})\frac{\partial k}{\partial x_j}] + P_k + P_b - \rho\epsilon - Y_M + S_k \tag{25}$$

$$\frac{\partial}{\partial t}(\rho \epsilon) + \frac{\partial}{\partial x_i}(\rho \epsilon u_i) = \frac{\partial}{\partial x_j}[(\mu + \frac{\mu_t}{\sigma_\epsilon})\frac{\partial \epsilon}{\partial x_j}] + C_{1\epsilon}\frac{\epsilon}{k}(P_k + C_{3\epsilon}P_b) - C_{2\epsilon}\rho\frac{\epsilon^2}{k} + S_\epsilon \tag{26}$$

where Y_M is the contribution of the fluctuating dilatation in compressible turbulence to the overall dissipation rate. $C_{1\epsilon}$, $C_{2\epsilon}$ and $C_{3\epsilon}$ are constants. σ_k and σ_ϵ are the turbulent Prandtl numbers for k and ϵ. S_k and S_k are user-defined source terms. The turbulent viscosity is modeled as:

$$\mu_t = \rho C_\mu \frac{k^2}{\epsilon} \tag{27}$$

where C_μ is a constant. The production of k term is:

$$P_k = -\rho\overline{u_i' u_j'}\frac{\partial u_j}{\partial x_i} = \mu_t S^2 \tag{28}$$

where $S = \sqrt{2S_{ij}S_{ij}}$ is the mean rate-of-strain tensor.

The production of turbulence due to buoyancy is:

$$P_b = \beta g_i \frac{\mu_t}{Pr_t} \frac{\partial T}{\partial x_i} \tag{29}$$

where $Pr_t = 0.85$ is the turbulent Prandtl number and g_i is the i-component of the gravitational vector. The coefficient of thermal expansion β is:

$$\beta = -\frac{1}{\rho}(\frac{\partial \rho}{\partial T})_p \tag{30}$$

The model constants have values: $C_{1\epsilon} = 1.44$, $C_{2\epsilon} = 1.44$, $C_\mu = 0.09$, $\sigma_k = 1.0$, $\sigma_\epsilon = 1.3$, $C_{3\epsilon} = -0.33$

3.5.2 Realizable k-ϵ

The first transport equation of turbulent kinetic energy k remains the same as in the Standard k-ϵ. Meanwhile, the transport equation of the dissipation rate ϵ becomes:

$$\frac{\partial}{\partial t}(\rho\epsilon) + \frac{\partial}{\partial x_i}(\rho\epsilon u_i) = \frac{\partial}{\partial x_j}[(\mu + \frac{\mu_t}{\sigma_\epsilon})\frac{\partial \epsilon}{\partial x_j}] + C_{1\epsilon}\frac{\epsilon}{k}(P_k + C_{3\epsilon}P_b) - C_{2\epsilon}\rho\frac{\epsilon^2}{k} - R_\epsilon + S_\epsilon \tag{31}$$

where the model constants are: $C_{1\epsilon} = 1.42$, $C_{2\epsilon} = 1.68$, $\sigma_k = 1.0$, $\sigma_\epsilon = 1.2$
The main difference from the Standard $k - \epsilon$ model is the additional term R_ϵ:

$$R_\epsilon = \frac{C_\mu \rho \eta^3 (1 - \eta/\eta_0)}{1 + \beta\eta^3} \frac{\epsilon^2}{k} \tag{32}$$

where $\eta = Sk/\epsilon$, $\eta_0 = 4.38$, $\beta = 0.012$.
The Realizable k-ϵ model is a more accurate version than the Standard k-ϵ. As in the Standard k-ϵ model, the turbulent viscosity is expressed as:

$$\mu_t = \rho C_\mu \frac{k^2}{\epsilon} \tag{33}$$

But in this model C_μ is no longer constant, but it is a function of the mean strain, rotation rates and turbulence fields k and ϵ.

3.5.3 RNG k-ϵ

The RNG k-ϵ model is derived from the Standard k-ϵ using a statistical technique called renormalization group theory.

$$\frac{\partial}{\partial t}(\rho k) + \frac{\partial}{\partial x_i}(\rho k u_i) = \frac{\partial}{\partial x_j}(\alpha_k \mu_{eff} \frac{\partial k}{\partial x_j} + G_k + G_b - \rho\epsilon - Y_M + S_k \tag{34}$$

$$\frac{\partial}{\partial t}(\rho\epsilon) + \frac{\partial}{\partial x_i}(\rho\epsilon u_i) = \frac{\partial}{\partial x_j}(\alpha_\epsilon \mu_{eff}\frac{\partial \epsilon}{\partial x_j}) + C_{1\epsilon}\frac{\epsilon}{k}(G_k + C_{3\epsilon}G_b) - C_{2\epsilon}\rho\frac{\epsilon^2}{k} - R_\epsilon + S_\epsilon \tag{35}$$

where α_k and α_ϵ are the inverse effective Prandtl numbers for k and ϵ. $C_{1\epsilon} = 1.42$ and $C_{2\epsilon} = 1.68$. The R_ϵ term is the same of the Realizable $k - \epsilon$ model. For high Reynolds numbers, the turbulent viscosity is:

$$\mu_t = \rho C_\mu \frac{k^2}{\epsilon} \tag{36}$$

where $C_\mu = 0.0845$ is derived using the RNG theory.
The standard $k-\epsilon$ model is suitable for high Reynolds flows; while the RNG $k-\epsilon$ model, due to RNG theory, has an analytically derived differential formula for effective viscosity that accounts for low Reynolds number effects, making this model capable of describing flows near walls with an adequate enhanced wall treatment.

3.5.4 Standard k-ω

The Standard k-ω model was developed by Wilcox, it is formed by two transport equation, one for the kinetic turbulent energy k and the second for the specific dissipation rate ω.

$$\frac{\partial}{\partial t}(\rho k) + \frac{\partial}{\partial x_i}(\rho k u_i) = \frac{\partial}{\partial x_j}(\Gamma_k \frac{\partial k}{\partial x_j}) + G_k - Y_k + S_k \tag{37}$$

$$\frac{\partial}{\partial t}(\rho \omega) + \frac{\partial}{\partial x_i}(\rho \omega u_i) = \frac{\partial}{\partial x_j}(\Gamma_\omega \frac{\partial \omega}{\partial x_j}) + G_\omega - Y_\omega + S_\omega \tag{38}$$

where G_k is the turbulent kinetic energy generated by velocity gradients. G_ω is the generation of ω, Γ_k and Γ_ω are the diffusivity of k and ω. Y_k and Y_ω are the dissipation of k and ω.
The Standard k-ω performs well in the viscous sublayer of wall-bounded flows. This model permits a better accuracy in the near wall treatment with the help of a switch between a wall function to a low-Reynolds number formulation based on grid spacing.

3.5.5 SST k-ω

The Shear Stress Transport SST k-ω was developed by Menter to blend the k-ω model in the near wall region to the k-ϵ model in the free-stream region in the far stream. The standard $k-\omega$ model and $k-\epsilon$ are multiplied by a blending function and added together.

$$\frac{\partial}{\partial t}(\rho k) + \frac{\partial}{\partial x_i}(\rho k u_i) = \frac{\partial}{\partial x_j}(\Gamma_k \frac{\partial k}{\partial x_j}) + \tilde{G}_k - Y_k + S_k \tag{39}$$

$$\frac{\partial}{\partial t}(\rho \omega) + \frac{\partial}{\partial x_i}(\rho \omega u_i) = \frac{\partial}{\partial x_j}(\Gamma_\omega \frac{\partial \omega}{\partial x_j}) + G_\omega - Y_\omega + D_\omega + S_\omega \tag{40}$$

where $\tilde{G}_k$ is the generation of turbulent kinetic energy due to the mean velocity gradients. G_ω is the generation of ω. Γ_k and Γ_ϵ represent the effective diffusivity of k and ω. Y_k and Y_ω represent the dissipation of k and ω due to turbulence. D_ω is the cross-diffusion term. S_k and S_ω are user-defined source terms.
To blend the $k-\epsilon$ model with the $k-\omega$ model together, the standard $k-\epsilon$ model has been transformed into equations based on k and ω, which leads to the introduction of the cross-diffusion term D_ω.

3.5.6 Reynolds Stress Model

The Reynolds Stress Model, RSM, is the most complex type of RANS turbulence model. It permits closure of the RANS equations by directly solving each term of the Reynolds stress tensor. This strategy is also called Second Order Closure, because it does not rely on the Bousinnesq hypothesis and describes each term of the Reynolds Stress Model. The RSM has four transport equations for the Reynolds stress tensor in a 2D flow and six transport equations in a 3D flow. The dissipation rate transport equation completes the model.
This model accounts for the directional effects of the Reynolds stresses. In flows characterized by high anisotropy, flow separation and recirculation, eddy viscosity models have relatively poor performances.
The transport equations for the Reynolds stresses can be expressed as follows.

$$\frac{\partial}{\partial t}(\rho\overline{u_i'u_j'}) = -\frac{\partial}{\partial x_k}[\rho\overline{u_i'u_j'u_k'} + \overline{p'(\delta_{kj}u_i' + \delta_{ik}u_j')}] + \frac{\partial}{\partial x_k}[\mu\frac{\partial}{\partial x_k}(\overline{u_i'u_j'})]$$
$$-\rho(\overline{u_i'u_k'}\frac{\partial u_j}{\partial x_k} + \overline{u_j'u_k'}\frac{\partial u_i}{\partial x_k}) + \overline{p'(\frac{\partial u_i'}{\partial x_j} + \frac{\partial u_j'}{\partial x_i})} - 2\mu\overline{\frac{\partial u_i'}{\partial x_k}\frac{\partial u_j'}{\partial x_k}} - 2\rho\Omega_k(\overline{u_j'u_m'}\epsilon_{ikm} + \overline{u_i'u_m'}\epsilon_{jkm}) \tag{41}$$

or more briefly:

$$partial\ time\ derivate = +C_{ij} = D_{T,ij} + D_{L,ij} + P_{ij} + \phi_{ij} - \epsilon_{ij} + F_{ij} \tag{42}$$

where C_{ij} is the convection term, $D_{T,ij}$ is the turbulent diffusion, $D_{L,ij}$ is the molecular diffusion, P_{ij} is the stress production, ϕ_{ij} is the pressure strain, ϵ_{ij} is the dissipation term and F_{ij} is the stress production by system rotation. The terms $D_{T,ij}$, ϕ_{ij} and ϵ_{ij} need to be modeled. In the literature, different formulations have been proposed to model these terms.

4 Validation

In the first part of the activity, the setup and validation process of the CFD model are described.

4.1 Domain

The selected numerical domain is derived from the real channel used in the experimental investigations conducted by Han et al. [3-4] in the 1980s. The channel has a square section with a side of 7.6 cm, so the hydraulic diameter also has the same value. It consists of three sections: an entry region long 1.524 m in order to have a fully developed flow; an heated region of 1.524 m, which is the test section; an exit region of 0.457 m to prevent exit effects. In fact, when the air enters the channel, it starts to interact with the walls and the boundary layer is progressively formed and developed until a certain length downstream. The exit trait is also necessary to keep the main flow undisturbed at the end of the heated region, so the properties of the flow remain stable.
Figures 4.1 and 4.2 show the real channel and the numerical model, respectively.

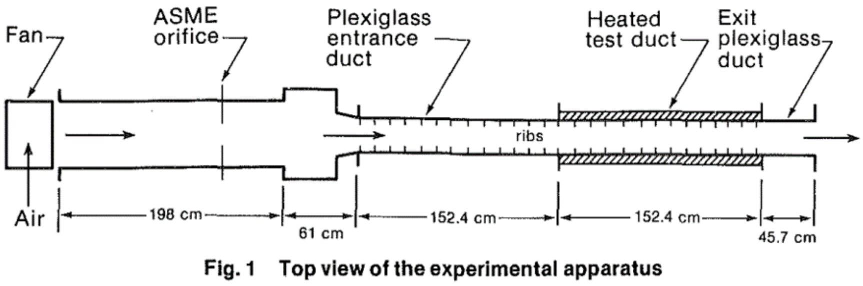

Figure 4.1: Experimental domain utilized by Han [3]

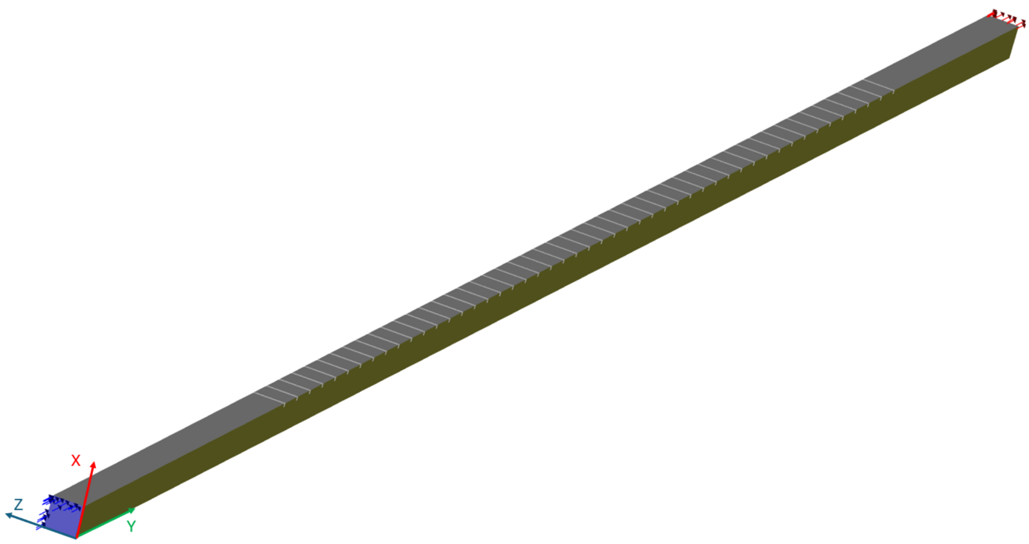

Figure 4.2: Numerical domain, realized with Ansys Design Modeler

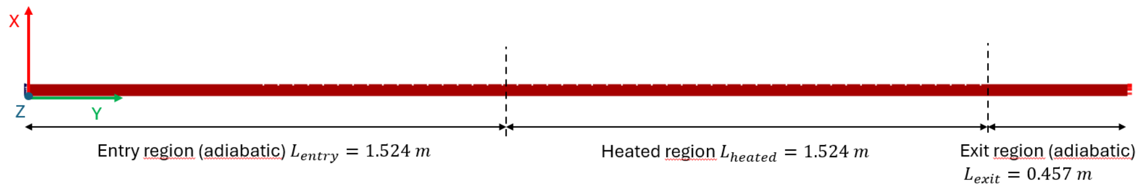

Figure 4.3: Numerical domain, lateral view

In Figure 4.3, a lateral view of the numerical channel is shown with the three different regions. In the first simulations, the whole section of the channel was considered. Then only one quarter of the channel was simulated, cutting the section in the XY and YZ symmetry planes to reduce the mesh elements (see Figure 4.4).

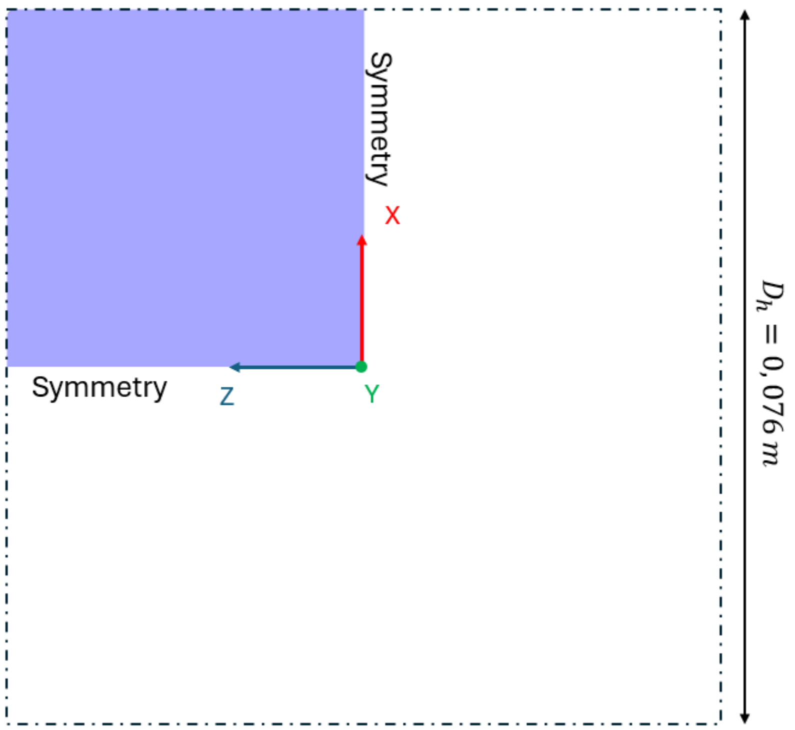

Figure 4.4: Numerical domain cross section, one quarter of the real channel

The square ribs are placed on two opposite walls. In the model the geometrical parameters of the ribs are taken from a case in the experimental campaign by Han [3], with rib height to hydraulic diameter e/D_h of 0.063 and pitch to height p/e of 10. The ribs are oriented at 90 degrees relative to the main flow. In Figure 4.5, a rib pitch is shown with the parameters used in the numerical model. A fillet with radius of $0.8mm$ is added to the edges of the ribs and the ribbed wall, because sharp edges as in the real channel ribs lead to issues in meshing and simulation instability. Ribs begin in the entry region and are placed with the aforementioned pitch between each other until the end of the heated region, exactly as in the experimental setup. More precisely, in the model the ribs are not placed from the start of the entry region, but after the first simulations it has been decided to start from the second half of the entry region; it has been observed that this compromise allows to have less mesh cells and to reach anyway fully developed flow. Instead, the exit region is smooth and its only objective is to remove the exit effects.

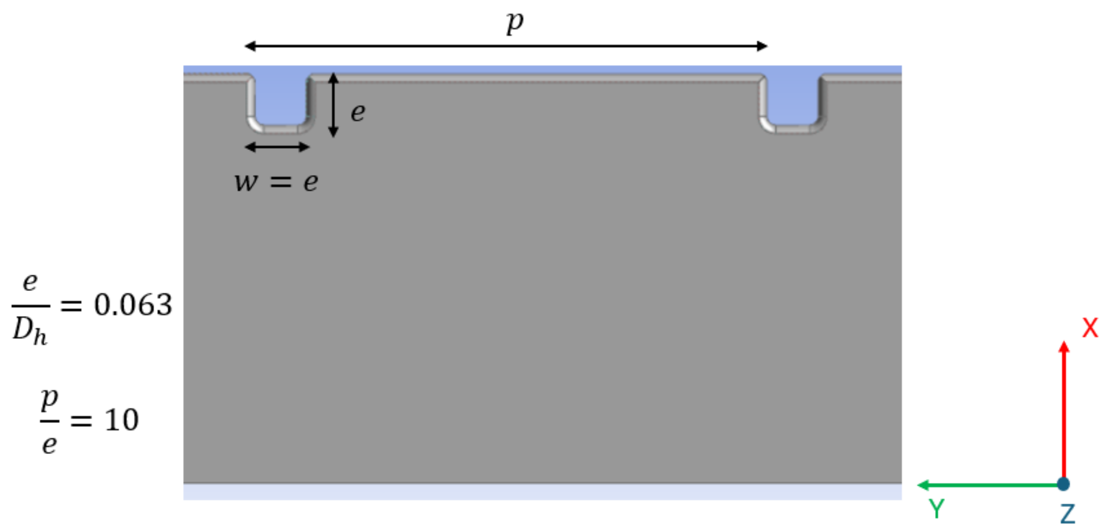

Figure 4.5: Geometrical parameters of the ribs in the numerical model

4.2 Mesh

After defining the domain, by means of Ansys Meshing a first hybrid mesh of about 17 million cells with tetrahedral elements is generated. The mesh is refined near the ribs and fillets, but coarse in the entrance and exit regions, where accuracy is not necessary. The refinement is done with a control sizing on every surface of the domain. The control sizing of the entry and exit region is in the order of 10^{-3} m; while in the heated region, which is the area of interest, the element sizing is about 10^{-4} m.

In order to guarantee a good accuracy of the results, stability and convergence of the simulations, it is necessary to insert inflation layers near walls to correctly capture the boundary layer development. The inflation type chosen is *first layer thickness*, with a size of $4 \cdot 10^{-5}$ m, 16 maximum layers and a growth rate of 1.1.

The ribbed side and the ribs are discretized with more elements than the smooth side. In general, the resolution has improved in the heated region. Initially, two different meshes with a different grade of refinement have been implemented: a finer mesh with about 17 million elements and a coarser mesh with about 9.5 million elements. A view of the finer mesh is shown in Figure 4.6. Then, a medium mesh has been generated, which is a trade-off of the two previous meshes, it has been derived from the coarse mesh with a slight more control refinement of the heated region. In the following paragraphs, it can be seen that the medium mesh has almost identical results compared to the fine mesh with less computational costs. The medium mesh has about 13.6 million elements. All three meshes are verified to have dimensionless wall distance values $y^+ < 5$, which is the prescribed interval for the turbulence models that describe the viscous sublayer (Standard $k - \omega$, SST

$k - \omega$, Reynolds Stress model), the zone of the boundary layer near the walls where the dissipation occurs.
Different types of $k - \epsilon$ turbulence models have been tested: Standard $k - \epsilon$, Realizable $k - \epsilon$ and RNG $k - \epsilon$. Generally, this family of turbulence models is only used with meshes with $y^+ > 30$, but in this case these models have been adopted with enhanced wall treatment, so these models can be used with all the three meshes described previously. The wall $y+$ is calculated as:

$$y^+ = \frac{y\ u_t}{\nu} \tag{43}$$

where u_t is the friction velocity, y is the absolute distance from the wall and ν is the kinematic viscosity.

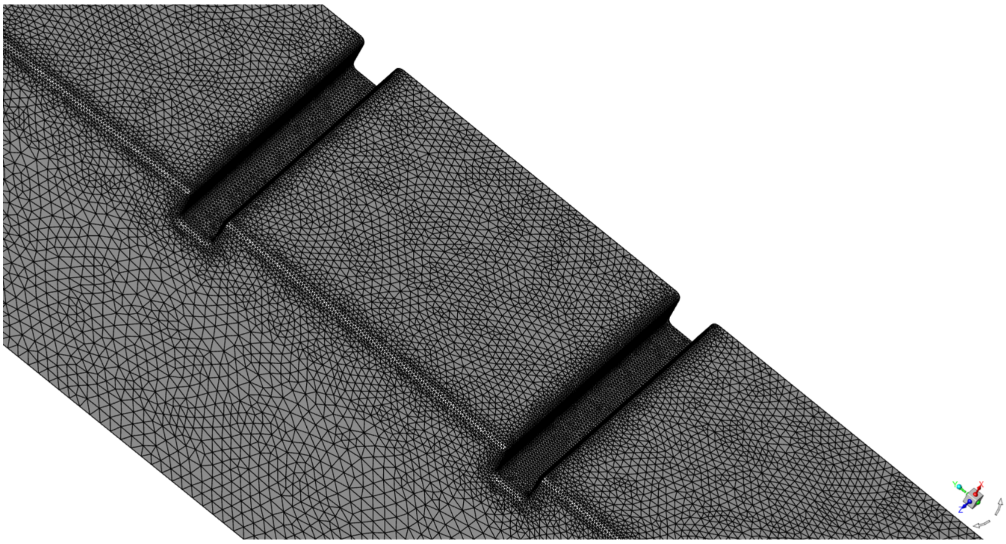

Figure 4.6: Fine mesh, detail of two ribs in the heated region

In the following paragraphs, it is demonstrated that the coarse and the medium mesh are sufficient to achieve good results, comparable to the experiments of Han et al. [3-4]. In the following pages, zoomed views of a rib pitch for the three meshes are shown (Figures 4.7, 4.8, 4.9). The most critical case for limiting the $y+$ below $y^+ < 5$ is the $Re = 42000$ case, where the turbulence is higher, thus the friction velocity u_t is higher. In Table 1, the maximum values of y^+ are reported for each case. The maximum y^+ is 2.64, which is within the acceptable interval. The y^+_{max} is the same for all the meshes in the $Re = 21500$ case, because the boundary layer sizing is the same for the three meshes. Moreover, these maximum values are reached only in a few localized spots, while in almost the whole mesh, the condition $y^+ < 1$ is verified, as shown in the y^+ contour image (Figure 4.10).

$\boldsymbol{y^+_{max}}$ $[-]$	**fine mesh**	**medium mesh**	**coarse mesh**
$Re = 21500$	1.68	1.68	1.68
$Re = 42000$	/	2.64	/

Table 1: y^+_{max} values for different meshes and flow conditions

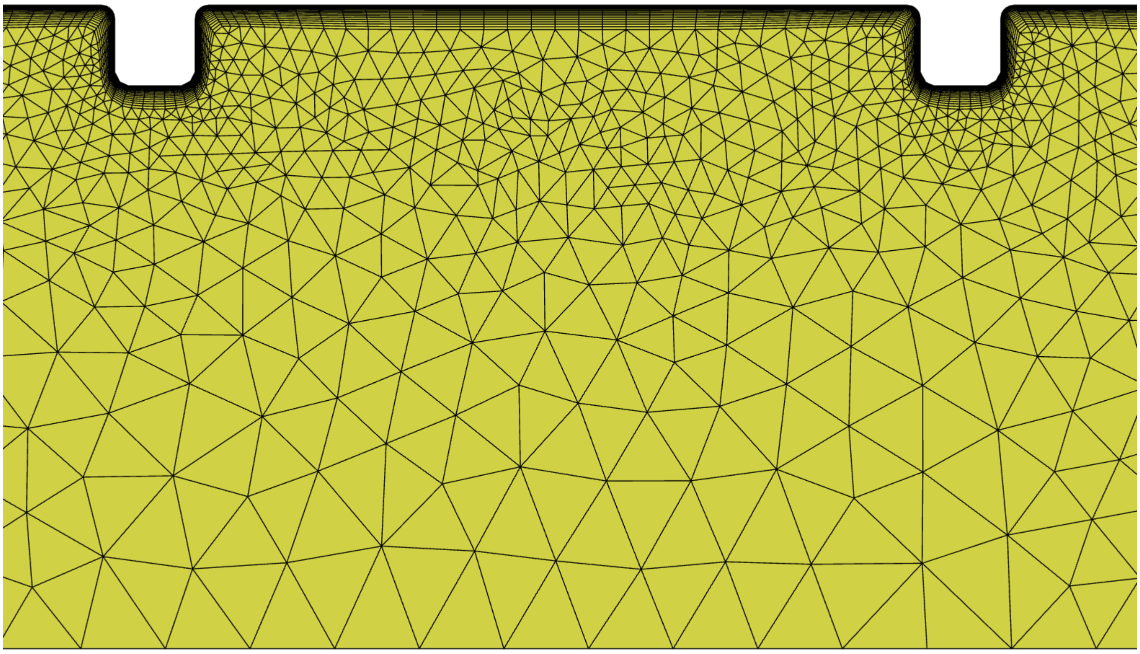

Figure 4.7: Coarse mesh of 9.5 million elements

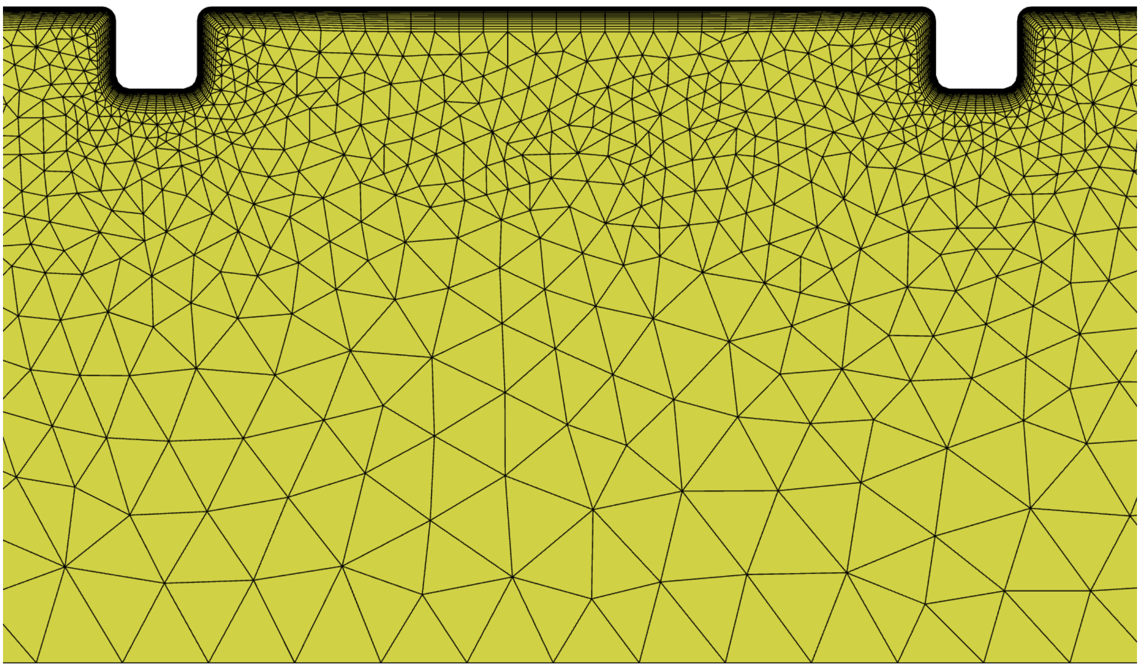

Figure 4.8: Medium mesh of 13.6 million elements

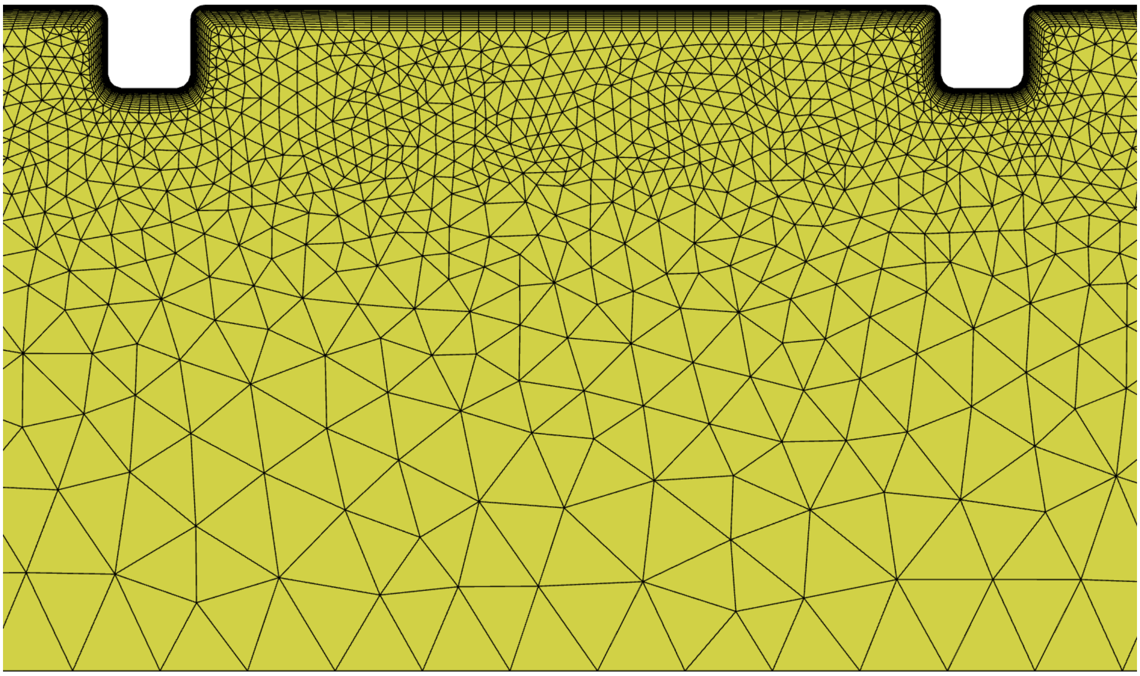

Figure 4.9: Fine mesh of 17 million elements

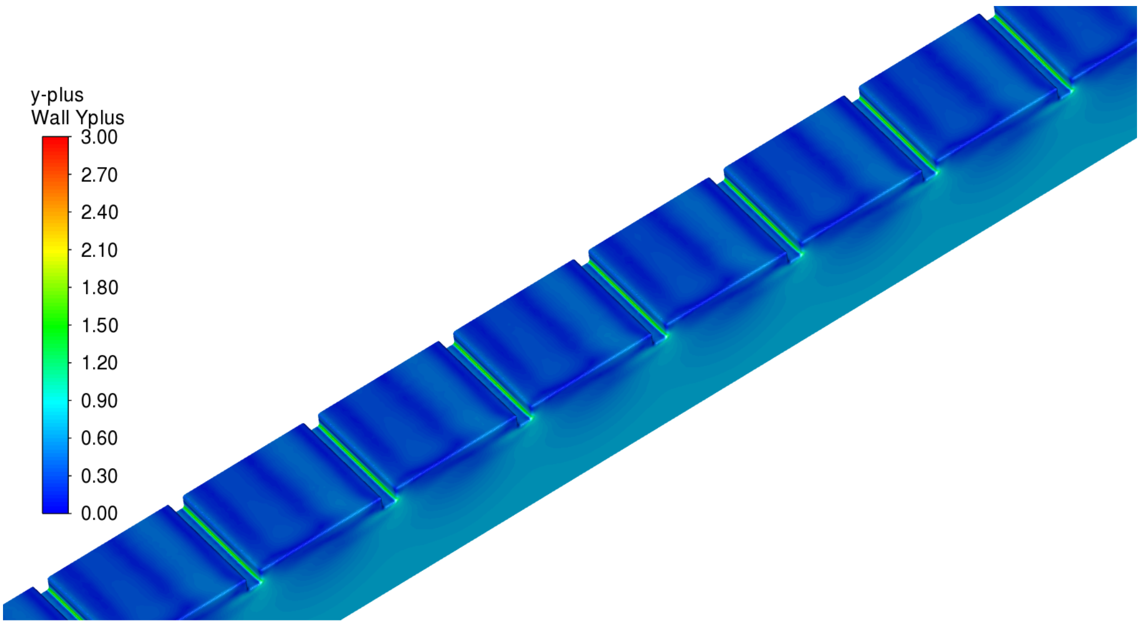

Figure 4.10: Contour of y^+, $Re = 42000$, medium mesh

4.3 Boundary conditions

In order to obtain consistent results in the CFD simulations, it is necessary to establish the boundary conditions consistent with the real physics.
The first boundary condition is at the inlet of the straight duct. After a few attempts, it was decided to adopt a mass flow rate inlet boundary condition, where the numerical value can be calculated from the Reynolds number, which is known.

$$Re = \frac{\rho D_h v}{\mu} \tag{44}$$

Inverting the precedent formula, the velocity is given by:

$$v = \frac{Re\mu}{\rho} \tag{45}$$

Then from the continuity equations, with the hypothesis of 1D stationary flow, the mass flow rate is:

$$\dot{m} = \rho A v \tag{46}$$

In Table 2, the values of mass flow rate calculated for the two flow conditions are reported.

Case	**entire mass flow-rate** $[kg/s]$	**one quarter mass flow-rate** $[kg/s]$
$Re = 21500$	0.03168	0.00792
$Re = 42000$	0.06189	0.01547

Table 2: Mass flow rate inlet values for the two Re numbers studied

The second boundary condition is the pressure at the outlet, which is set at ambient pressure $p_2 = 101325\ Pa$, because in the experimental setup by Han the air exits directly from the channel to the external environment.
Then a constant temperature $T = 350\ K$ is imposed for all walls and ribs of the heated region, while all other walls of the entry and exit regions are kept adiabatic. Firstly, the heat flux boundary condition was implemented, but the heat transfer results were considerably lower than the experimental ones. After postprocessing results from the first simulation with heat flux imposed on the heated region walls, an average temperature of 350 K was adopted in substitution of the constant heat flux condition. It was seen that using constant temperature wall boundary condition coupled with a bulk temperature evolution leads to better stability and faster convergence. The boundary conditions are reported in Table 3.

zone	**boundary condition**	**value**
inlet	mass flow rate $\dot{m}$	(see Table 2)
outlet	static pressure	$101325\ Pa$
walls heated region	T_{wall}	$350\ K$
walls entry and exit region	heat flux	adiabatic

Table 3: Boundary conditions imposed for the CFD model

4.4 Case setup

For the turbulence model and the mesh resolution choice, all simulations have been performed using a Reynolds number of $Re = 21500$, from which the mass flow rate inlet has been calculated. The properties of air have been established on the basis of the inlet temperature of 300 K and the temperature evolution along the heated region. Their values along the channel are calculated from laws used in the literature. The thermal conductivity is obtained by a polynomial function:

$$\lambda = -3.06 \cdot 10^{-4} + 9.89089 \cdot 10^{-5}\, T - 3.46571 \cdot 10^{-8}\, T^2 \tag{47}$$

The air properties are resumed in Table 4.

Air property	**law**
Fluid type	Ideal gas
Specific heat c_p	Nasa 9-piece polynomial
Thermal conductivity λ	polynomial(T)
Dynamic viscosity μ	Sutherland law

Table 4: Coolant physical properties

In the following table, the imposed solver settings are reported.

solver	**Pressure-based (viscous heating enabled)**
Pressure-velocity coupling	Coupled
Gradient	Least squares cell-based
Spatial discretization	Second order upwind

Table 5: Solver options

Second-order spatial discretization has been imposed in the solver options to obtain more accurate results. The pressure-based approach is more suitable for incompressible and mildly compressible flows, so it is selected because in this case the density undergoes very little variation along the channel. A coupled strategy is chosen to have more accuracy than a segregated approach. Furthermore, the viscous heating option has been enabled to account for the dissipation in the viscous sublayer of the boundary layer. Initially, this option was disabled, and the heat transfer results were too low compared to the experimental results by Han. Then the mesh sensitivity and the turbulence model sensitivity have been evaluated.

4.5 Postprocessing of the numerical results

The following thermal results are calculated as an average value between the smooth and the ribbed walls, in order to capture also the effect that the ribbed side has on the adjacent smooth side.
With the help of user-defined function in the Fluent solver, the Nusselt number has been defined as the area-weighted average in the ribbed wall, ribs and smooth side.

$$Nu = \frac{\dot{Q} D_h}{\lambda (T_{wall} - T_{bulk})} \tag{48}$$

where $\dot{Q}$ is the heat flux, $T_{wall} = 350K$ is the set boundary condition and T_{bulk} is a crescent linear function of the temperature along the heated region. T_{bulk} has been defined through a user-defined function, where the temperature increases linearly with the heated region axial coordinate, as stated in the previous case setup paragraph. The temperature at the inlet of the heated region is around 300 K, the same as at the inlet of the entry region, which is not heated. The temperature at the outlet of the heated region has been read for each simulation, it is always around 320 K. Then, the temperature along the heated region has been linearly interpolated between these extremes (see Figure 4.11).

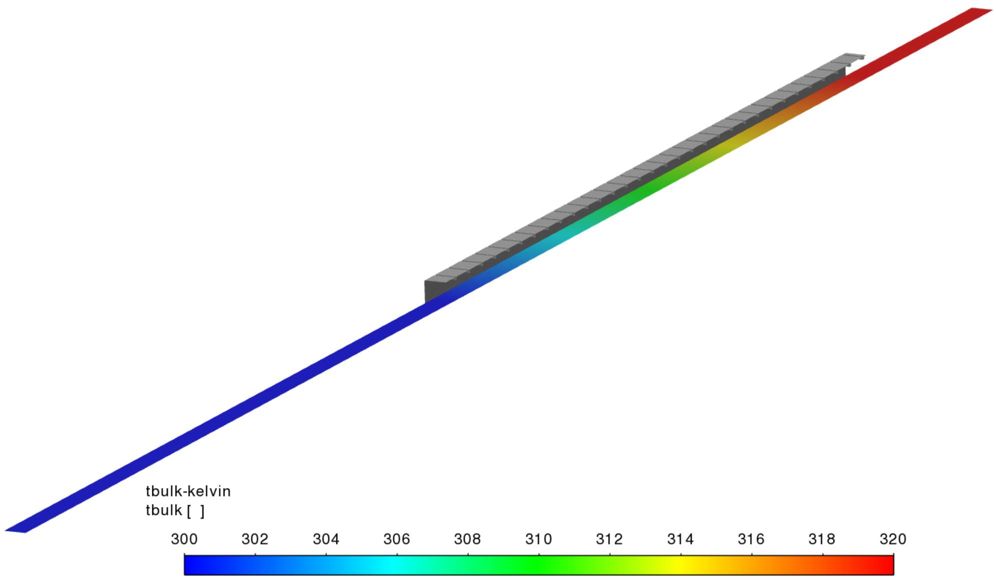

Figure 4.11: Evolution of the coolant total temperature through the heated section

The friction factor is calculated as:

$$f = \frac{p_{in} - p_{out}}{2 \frac{L}{D_h} \rho v^2} \tag{49}$$

where p_{in} and p_{out} are the area-weighted average static pressures at the inlet and outlet of the heated section (Figure 4.12), L is the length of the heated region, ρ and v are the mass-weighted average density and the velocity at the inlet of the heated section.
The thermal exchange has also been calculated with a second approach, for discrete axial coordinates along the heated region. The heated region length has been discretized with planes and iso-surfaces perpendicular to the main flow placed at 0.002

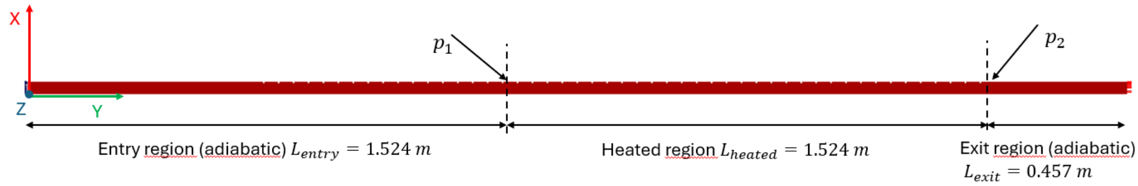

Figure 4.12: The area-weighted static pressure is read at the inlet and outlet of the heated region to calculate the friction factor

m between each other (Figures 4.13 and 4.14). The planes and iso-surfaces have been created with the help of a journal function in Fluent. In each iso-surface the area-weighted average heat flux and in each plane the mass-weighted average total temperature and thermal conductivity have been read to calculate the local Nusselt number.

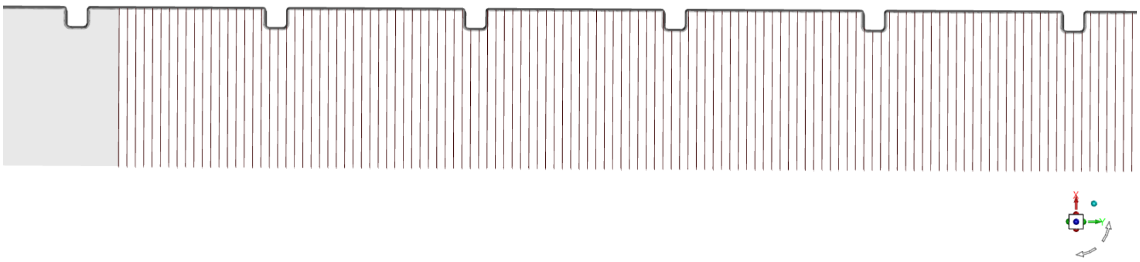

Figure 4.13: Length discretization of the heated region, planes with pitch 0.002 m

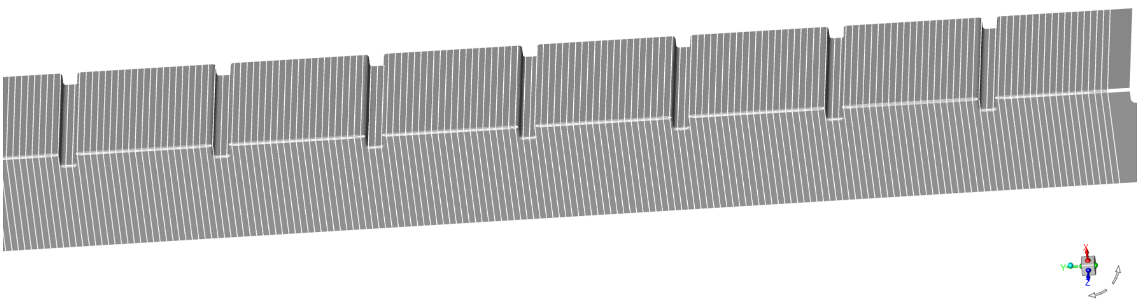

Figure 4.14: Length discretization of the heated region, iso-surfaces with pitch 0.002 m

4.5.1 Turbulence model sensitivity results, Re=21500

Simulations were run with different turbulence models to account for the boundary layer development near the walls and accurately approximate wall heat exchange. This analysis was performed completely under the same flow condition $Re = 21500$.

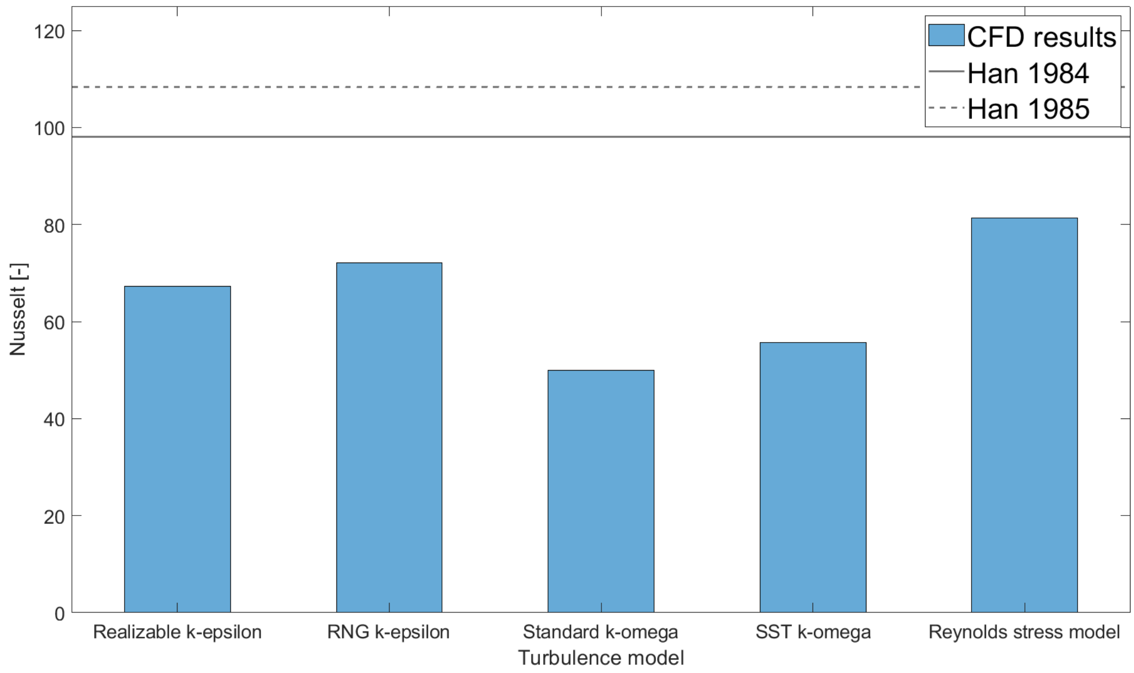

Figure 4.15: Turbulence model sensitivity results of the average Nu

turb.model	wall	$\boldsymbol{Nu\ CFD}$ $[-]$	$\Delta\%$ $\boldsymbol{Han}$ **1984** $[-]$	$\Delta\%$ $\boldsymbol{Han}$ **1985** $[-]$
Realizable $k-\epsilon$	smooth	66.4	12.1%	-25.3%
	ribbed	67.8	-50.4%	-46.9%
	average	67.2	-31.4%	-38%
RNG $k-\epsilon$	smooth	70.4	18.8%	-20.8%
	ribbed	73.6	-46.2%	-42.4%
	average	72.1	-26.4%	-33.4%
Standard $k-\omega$	smooth	52.8	-10.9%	-40.6%
	ribbed	47.6	-65.2%	-62.7%
	average	50	-49%	-53.8%
SST $k-\omega$	smooth	59	-0.5%	-33.6%
	ribbed	53.1	-61.2%	-58.5%
	average	55.7	-43.2%	-48.6%
Reynolds Stress model	smooth	73.4	24%	-17.3%
	ribbed	87.8	-35.8%	-31.3%
	average	81.4	-17%	-24.9%

Table 6: Turbulence model sensitivity results, average Nu number

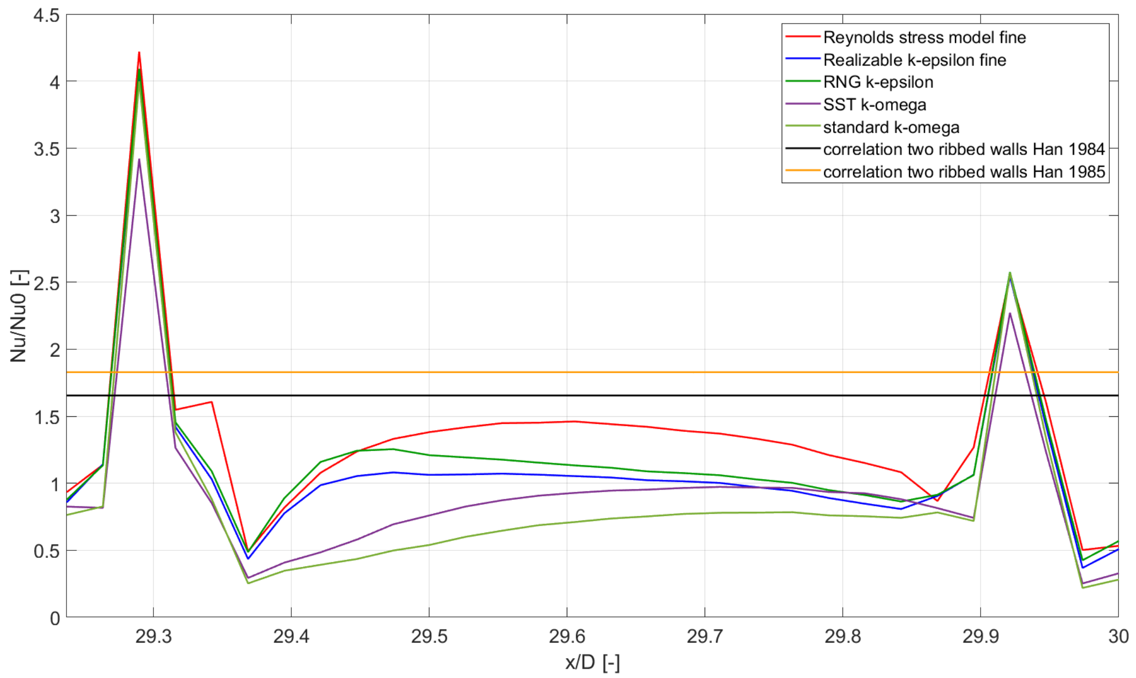

Figure 4.16: Turbulence models sensitivity of the Nusselt ratio between two ribs in the middle of the heated region

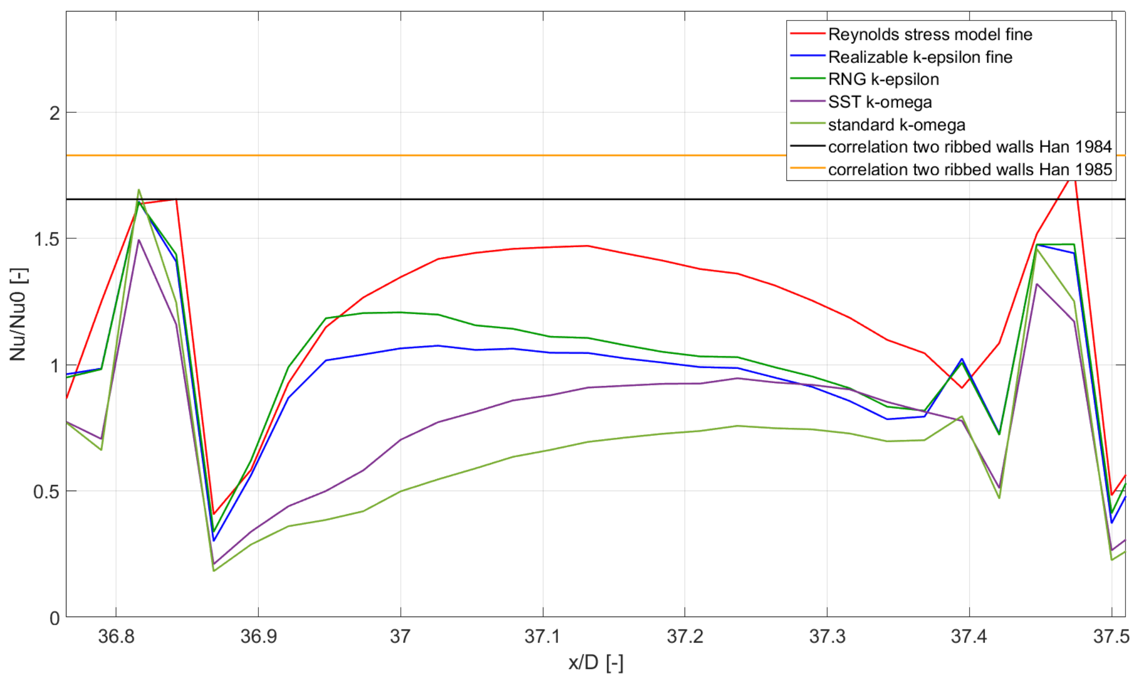

Figure 4.17: Turbulence models sensitivity of the Nusselt ratio between two ribs at the end of the heated region

In Figure 4.15 and Table 6, it can be seen that the Reynolds stress model more accurately represents heat exchange near the walls. The average Nusselt number is similar to the experimental correlations; instead, the eddy viscosity turbulence models considerably underestimate the thermal phenomena, in particular for the $k-\omega$ models the results are not consistent with the real ones, because the smooth side obtains an higher Nusselt compared to the ribbed side.
The Nusselt number obtained with correlations is higher than that obtained with the RSM, this is probably due to the limited number of measurement points in the experimental setup by Han et al. In an experimental setup the number of acquisitions is limited by the thermocouples and temperature sensors, while in a CFD calculation, the whole surface can be studied.
In Figures 4.16 and 4.17, the Nusselt number ratio Nu/Nu_0 is calculated at each axial coordinate in two different rib intervals, one in the central trait of the heated region (Figure 4.16) and the second interval at the end of the heated region (Figure 4.17). The profiles reflect the flow behaviour near walls caused by the ribs, in particular right after the rib a recirculation zone is generated, where the flow slows down. Then the secondary flow reattaches with the main flow and the same pattern is repeated similarly at each rib pitch. In the experimental results, this profile is not entirely captured, but only a few discrete points are evaluated in correspondence of the temperature sensors (Figure 4.18). For example, the minimum peak of Nusselt ratio after a rib is not completely taken into account, so the average heat transfer results are higher than the CFD results. In conclusion, both for the average results and the axial results lead to the choice of the Reynolds Stress Model over the eddy viscosity models.

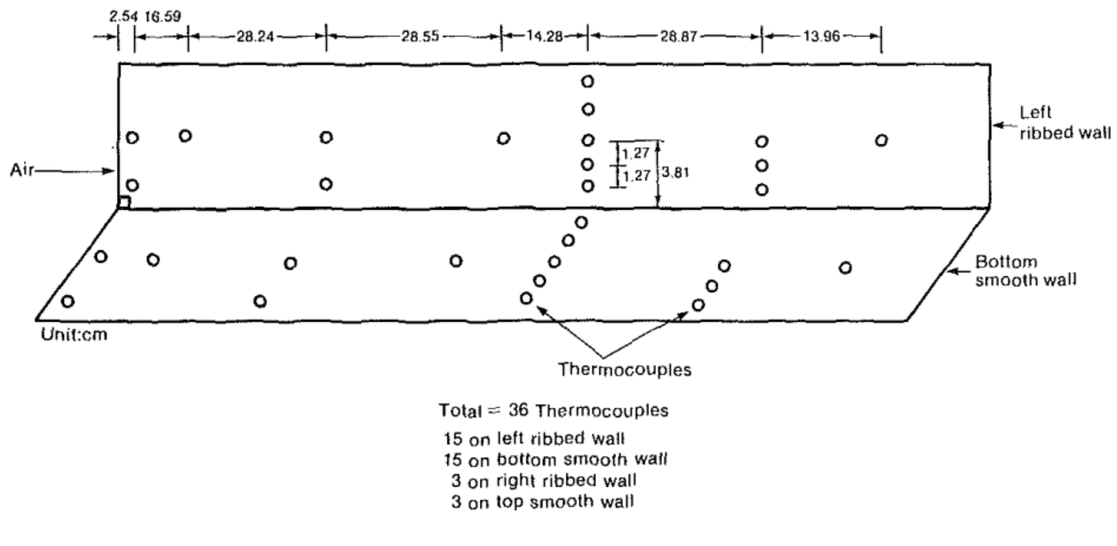

Figure 4.18: Thermocouples distribution on the test equipment [3]

Moreover, the numerical friction factor with the Reynolds Stress Model is almost equal to that calculated by correlations. Instead, with eddy viscosity models, f is greatly underestimated. The friction factor results are shown in Figure 4.19 and Table 7.

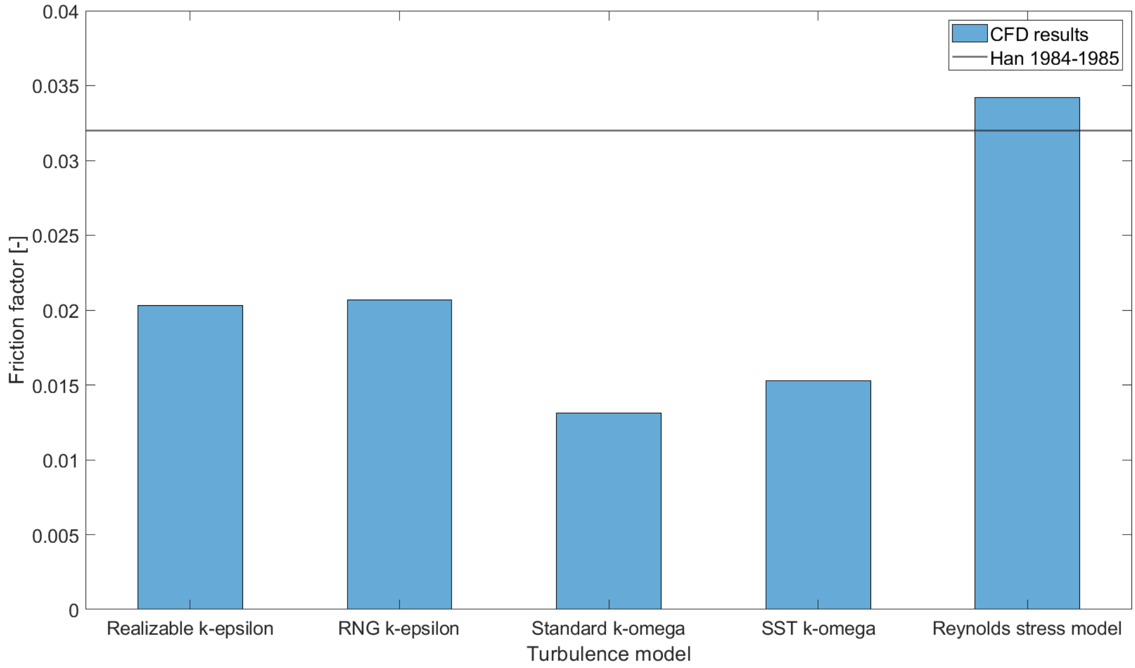

Figure 4.19: Turbulence model sensitivity results of friction factor

turbulence model	$\boldsymbol{f}$ $\boldsymbol{CFD}$ $[-]$	$\boldsymbol{f}$ $\boldsymbol{Han}[-]$	$\boldsymbol{\Delta}\%$
Realizable $k-\epsilon$	0.0203		-36.12%
RNG $k-\epsilon$	0.0207		-34.86%
Standard $k-\omega$	0.0131	0.0318	-58.92%
SST $k-\omega$	0.0153		-51.99%
Reynolds stress model	0.0342		7.50%

Table 7: Turbulence model sensitivity results of friction factor

4.5.2 Mesh resolution sensitivity results, Re=21500

After confirming the Reynolds stress turbulence model, different meshes with different resolutions have been tested. This analysis was carried out entirely under the same flow condition of $Re = 21500$, as for the turbulence model sensitivity. In the following graphs and tables, it can be seen that the results are independent of the mesh resolution. The medium and coarse meshes are sufficient to have good heat transfer predictions; therefore, adopting the fine mesh would cost additional computational time without significant advantages. In Figure 4.20 and Table 8, the average Nu values for the three meshes with the Reynolds Stress Model are reported. In Figure 4.21, the values of Nusselt ratio in each axial coordinate with Reynolds Stress Model and Realizable $k-\epsilon$ are compared with different mesh resolutions in a rib pitch around the middle of the heated region; the average values calculated from the correlations are also displayed. The same comparison is made in Figure 4.22 for a rib pitch near the end of the heated region.

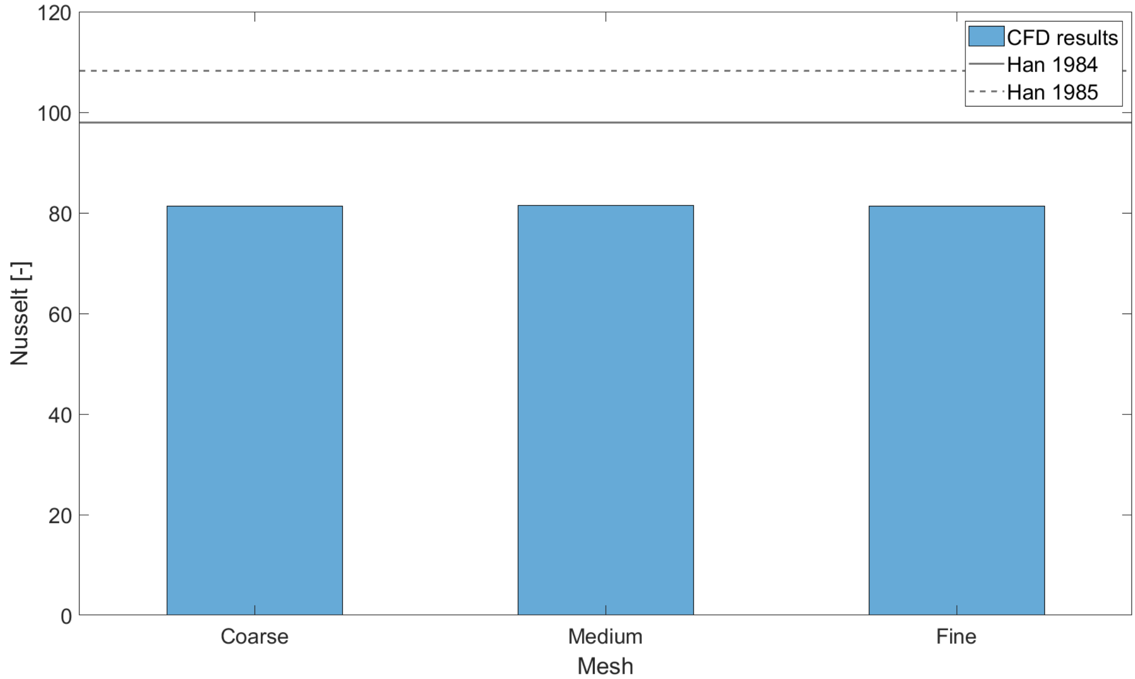

Figure 4.20: Mesh sensitivity results, average Nu, Reynolds Stress model

$\boldsymbol{Nu}$ ***CFD*** $[-]$ **Reynolds Stress model**	**fine mesh**	**medium mesh**	**coarse mesh**
smooth side	73.4	73.5	73.4
ribbed side	87.8	87.7	87.6
average	81.4	81.5	81.3

Table 8: Mesh sensitivity results, average Nu, Reynolds Stress model

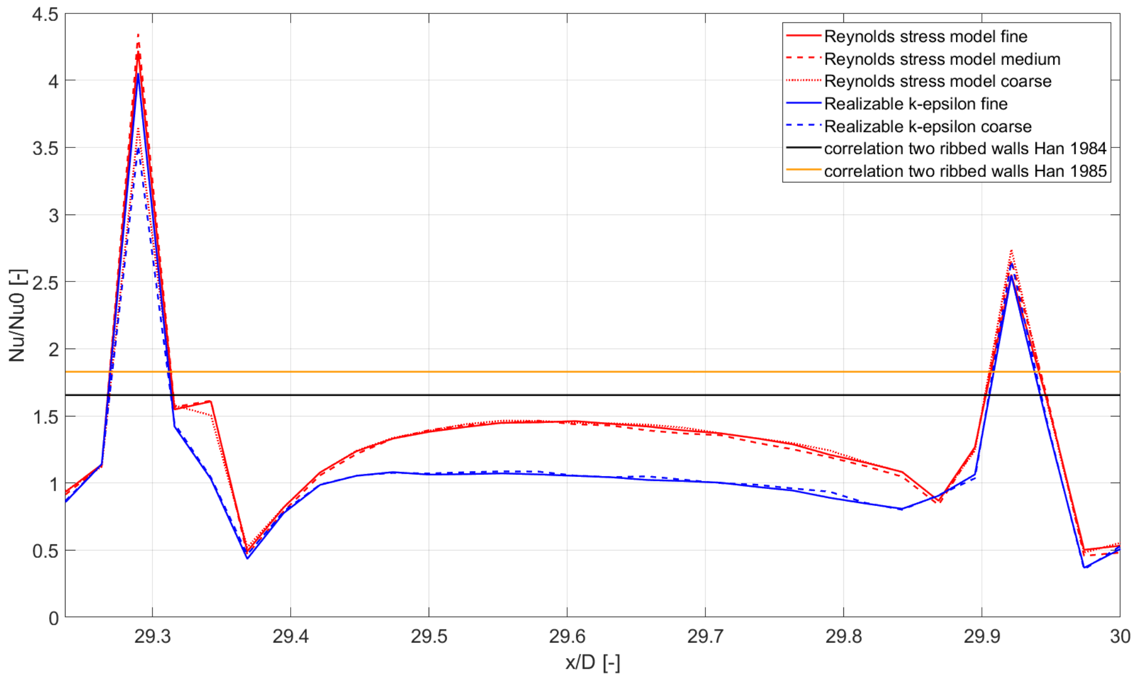

Figure 4.21: Mesh sensitivity results of Nu/Nu_0 of a rib pitch in the middle of the heated region

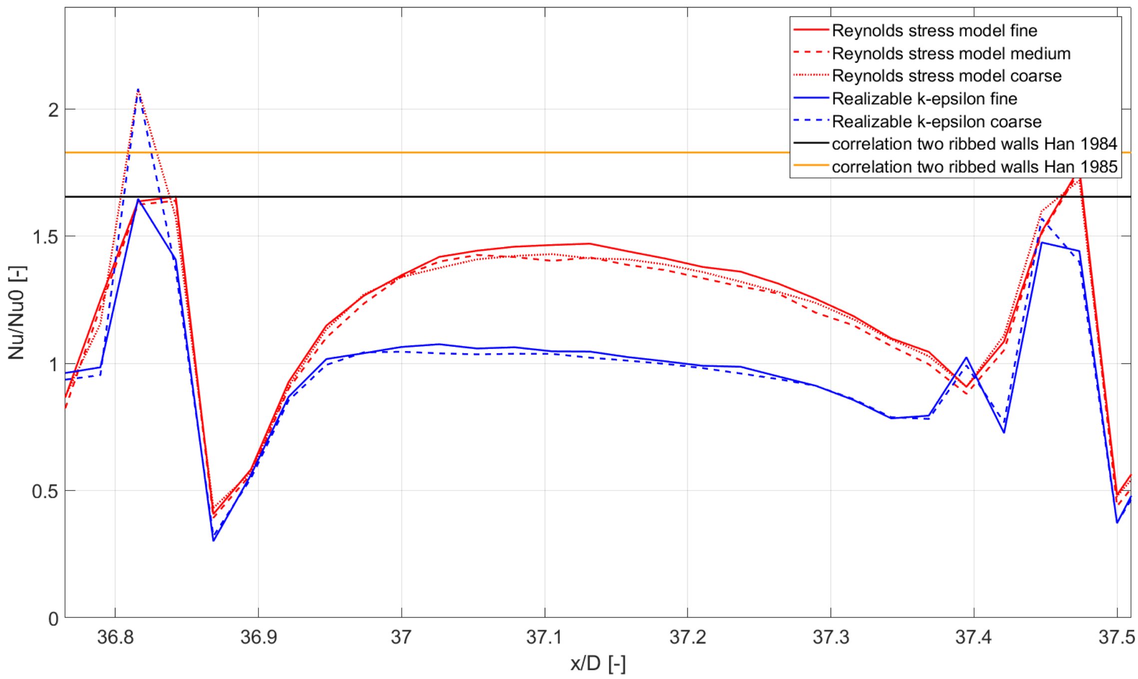

Figure 4.22: Mesh sensitivity results of Nu/Nu_0 of a rib pitch at the end of the heated region

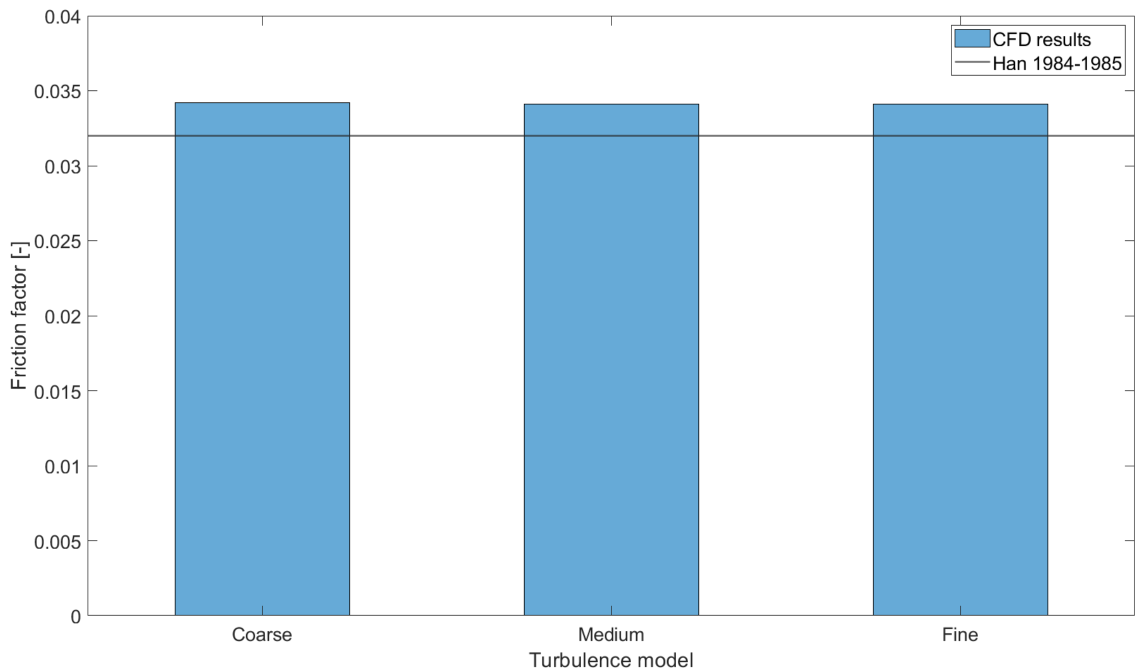

Figure 4.23: Mesh sensitivity results of friction factor, Reynolds Stress model

Reynolds Stress model	fine mesh	medium mesh	coarse mesh
$f\ CFD\ [-]$	0.0342	0.0341	0.0341

Table 9: Mesh sensitivity results, friction factor f, Reynolds Stress model

In Figure 4.23 and Table 9, the friction factor values with the Reynolds Stress model and the three mesh resolutions are shown. The results are almost equivalent to the correlations and are independent of the mesh resolution.

4.5.3 Choice of the turbulence model and the mesh resolution

The setup that better correlates with the experimental results is the channel with Reynolds stress model as turbulence model and the medium resolution mesh, which represents a good compromise between accuracy and simulation costs. The average thermal results of this configuration, compared with the correlations, are reported in Table 10.

$\boldsymbol{Nu}[-]$	CFD	Han 1984	Δ%	Han 1985	Δ%
smooth side	73.5	59.3	24%	88.8	-17.3%
ribbed side	87.7	136.8	-35.9%	127.8	-31.4%
average	81.5	98	-16.9%	108.3	-24.8%

Table 10: Area-averaged Nu results using the Reynolds Stress model and medium mesh, comparisons with correlations results, $Re = 21500$

The numerical results tend to be lower than the experimental correlations; this is probably caused by the few measurements considered in the experiments, as described in the turbulence model sensitivity paragraph and by the intrinsic approximation errors of the numerical model. However, the numerical results well describe the heat transfer enhancement produced by the ribbed wall, not only on the wall itself, but also on the adjacent smooth wall. In fact, the Nusselt number of the smooth side is closer to the Han 1985 correlation, which also takes into account this enhancement of the heat transfer on the smooth side produced by ribs.

In conclusion, the numerical results obtained with the chosen turbulence model and mesh resolution represent a good approximation of the real phenomenon and are the starting point for a successive channel geometry optimization.

4.5.4 Results Re=42000

Successively, the Reynolds number has been augmented to 42000 to verify the similarity between simulation results and empirical correlations under a different and more turbulent condition.

For this Reynolds value, only the setup validated at $Re = 21500$, with a medium resolution mesh and the Reynolds Stress turbulence model is evaluated.

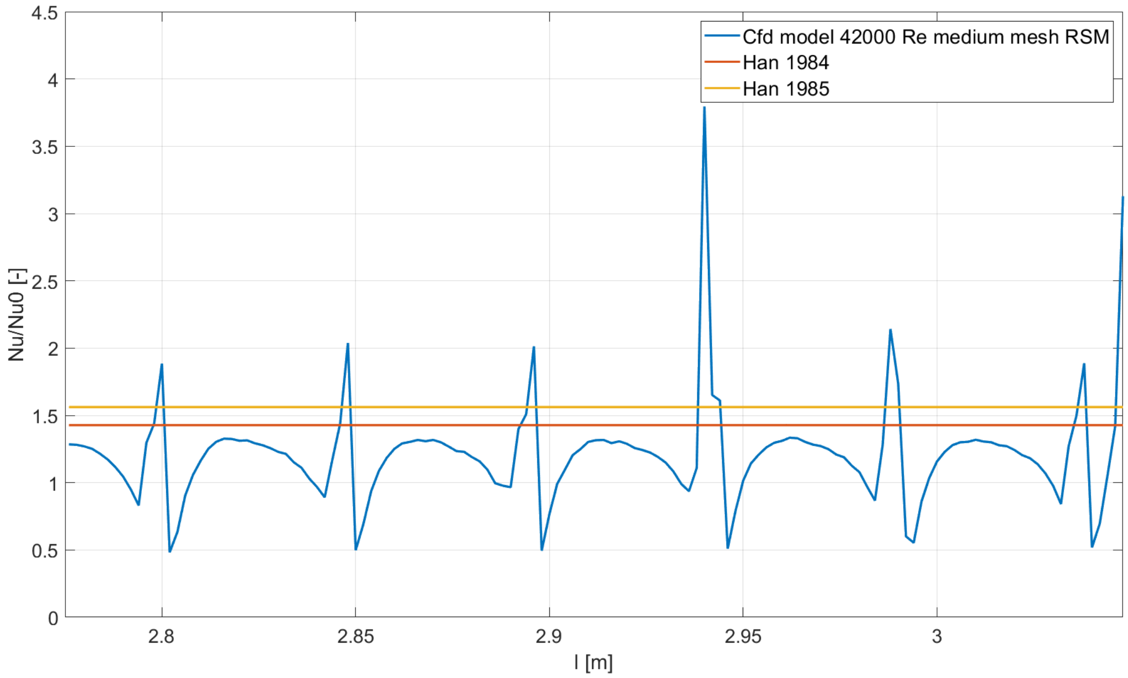

Figure 4.24: Nu/Nu_0 axial values of a portion of the heated region and average values from experimental correlations

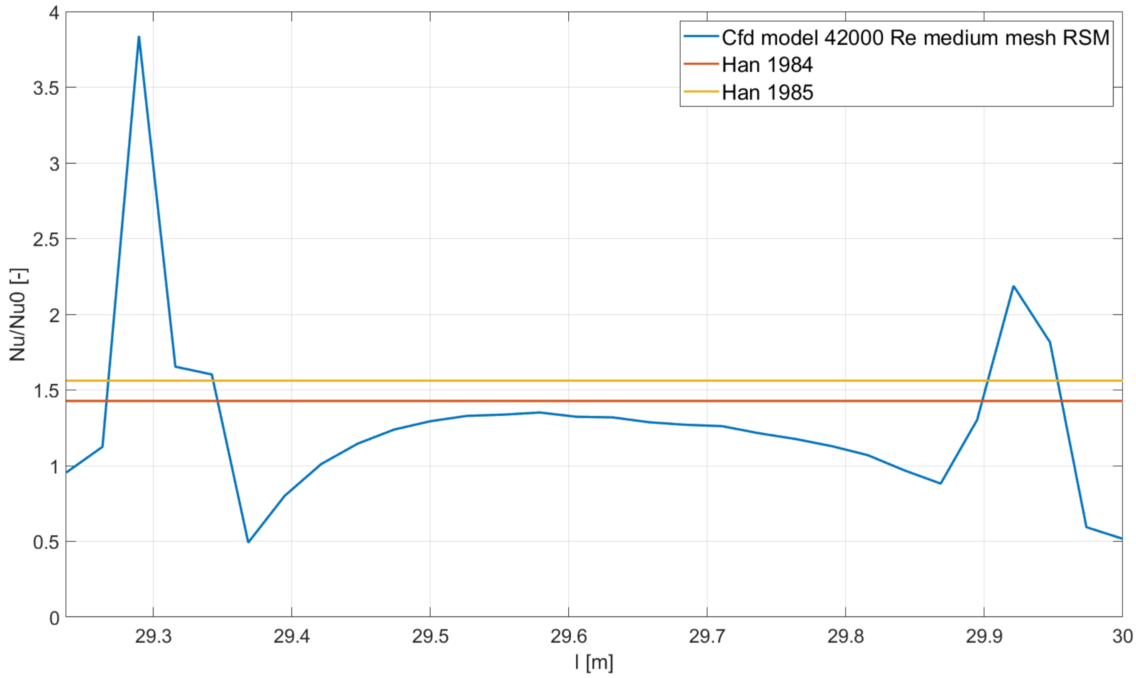

Figure 4.25: Nu/Nu_0 axial values in a rib interval in the middle of the heated region and average values from experimental correlations

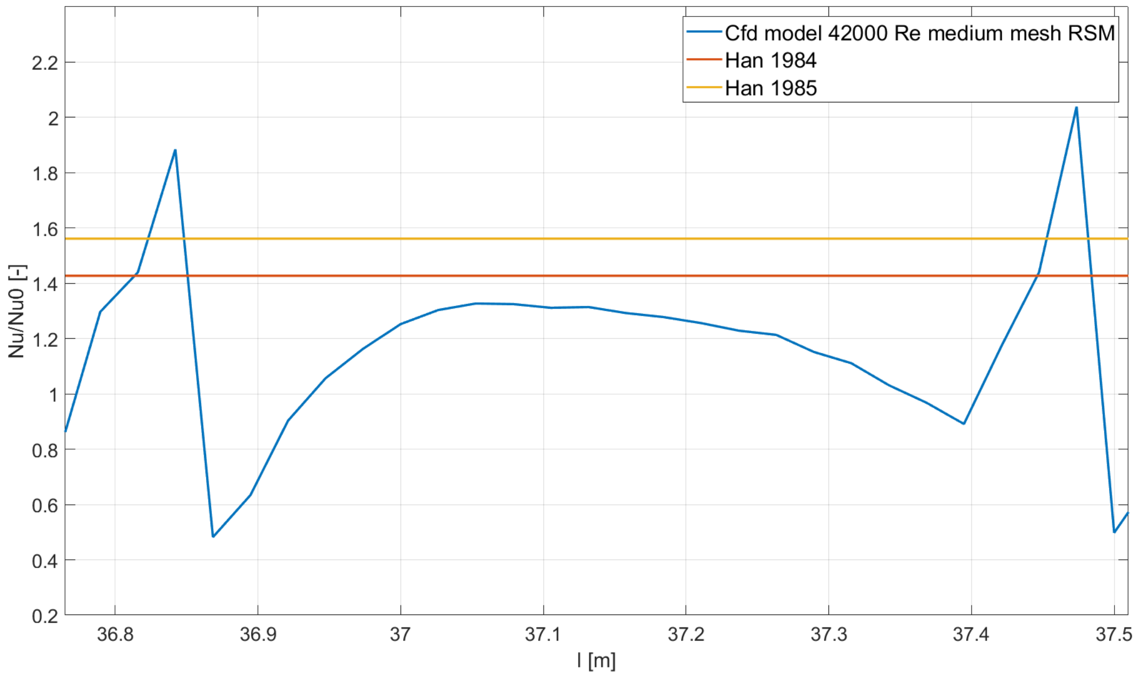

Figure 4.26: Nu/Nu_0 axial values in a rib interval at the end of the heated region and average values from experimental correlations

$Nu[-]$	CFD	Han 1984	Δ%	Han 1985	Δ%
smooth side	124.73	101.24	23.2%	146.53	-14.9%
ribbed side	140.92	226.75	-37.9%	213.16	-33.9%
average	133.66	163.99	-18.5%	179.84	-25.7%

Table 11: Area-averaged Nu results using the Reynolds Stress model and medium mesh, comparisons with correlations results, $Re = 42000$

Figure 4.24 shows the graph of the Nusselt ratio at each axial coordinate of a portion of the heated region. Figures 4.25 and 4.26 are detailed zooms of Nu/Nu_0 results of two rib pitches in the heated region, in the middle and at the end of the heated region, respectively. The numerical results have the same characteristics of the lower Re case compared to the experimental correlations; in particular, the enhancement of heat transfer in the smooth wall. This confirms that the previous choices made for the setup, the turbulence model and the mesh resolution are suitable, even for higher Reynolds numbers and a more turbulent flow.
Then, in Table 12 the friction factor is reported, it has a very close value to the experimental correlation. In conclusion, the CFD results well represent the experimental correlations in both flow conditions.

$f\ CFD[-]$	$f\ Han\ 1984-85[-]$	Δ%
0.0296	0.0313	-5.55%

Table 12: Friction factor, comparison between CFD results and experimental correlations, $Re = 42000$

5 Adjoint-based optimization

The second part of this work focuses on optimizing heat exchange performance in the final trait of the channel. The method used is adjoint-based optimization, by means of a tool available in Fluent. The idea of using this strategy is inspired by an article by He et al. [6], where a ribbed U-bend internal cooling channel is optimized in terms of aerothermal performance, with an objective function that is a linear combination of heat transfer and friction losses to consider the trade-off between these quantities.

Conventional optimization methods, called gradient-free algorithms, are much more time consuming because they do not provide a defined search direction for the objective function. They are excessively expensive for a large number of design variables, due to the fact that the optimization is not automated.

In recent years gradient-based optimizers coupled with discrete adjoint method became very popular for automating the design of turbine internal cooling channels, but also in different other fields. Adjoint-based optimization is an efficient method of calculating the gradients of the objective functions. The adjoint equations allow for the rapid solution of the gradients of the objective functions because their advantage is the independence from the number of design variables. In CFD applications, the continuous adjoint method writes the adjoint equations from the original Navier-Stokes equations, then discretizes them. Instead, in the discrete adjoint approach, first the Navier-Stokes equations are discretized, then the adjoint equations are applied. The mathematical background is not discussed because it is beyond the scope of this work, but only the practical steps performed for the optimization process are described.

The discrete Adjoint-based optimization is already implemented in Fluent and is a valid help in designing new shapes. It consents to obtain the optimal shape of a component to guarantee the best results for a given working condition with specified boundary conditions. This tool allows to obtain irregular and different shapes instead of parametric design with only a few design variables.

5.1 Optimization domain last 6 ribs

The chosen domain for the optimization is half of the real channel in section, but only a limited trait in length from an axial distance from the inlet of 2.775 meters. The domain is shown in Figure 5.1. This region comprises the last six ribs of the heated region and the entire exit region, for a better simplicity of the outlet boundary condition. Initially, the exit region was excluded from the optimization domain, but it was seen that having to extract physical quantities profiles both at the inlet and at the outlet of the optimization domain was time-consuming and also decreased the results accuracy. Instead, considering also the exit region consents to set a simple ambient pressure boundary condition at the outlet, which is much more immediate and simple.

Instead of considering a quarter of the channel cross section as in the validation, it was chosen to model half of the channel cross section to have entire ribs and not add a symmetry constraint in the optimization (Figure 5.2).

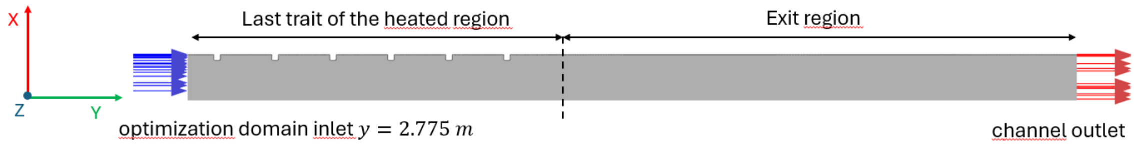

Figure 5.1: Optimization domain, with last 6 ribs of the heated region from $y = 2.775\ m$, lateral view

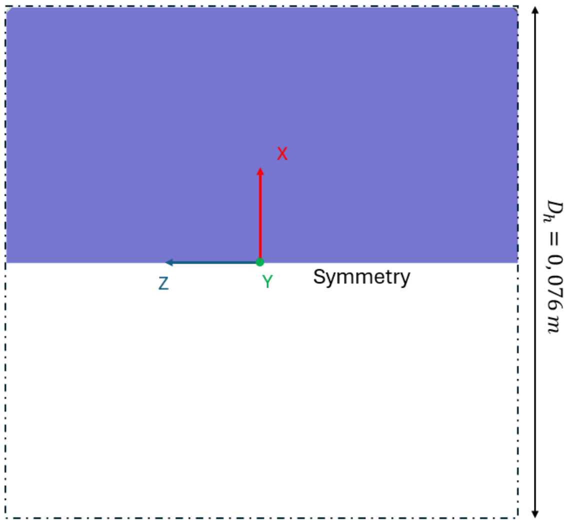

Figure 5.2: Optimization domain, half cross section has been simulated

5.1.1 Mesh

The reference mesh is the medium resolution mesh selected in the validation procedure. The only difference is the named selection, where the ribs are considered singularly to optimize each shape separately. In this way, each rib obtains a unique and independent shape based on the coolant flow and its properties.
Obviously, the number of mesh elements is significantly lower for the reduced domain, the number of mesh elements is about 4.1 million cells.

5.1.2 Boundary conditions

All the boundary conditions for this reduced domain are the same of those of the entire channel chosen in the validation, with Reynolds stress turbulence model and medium resolution mesh. The only difference is the inlet boundary condition, where a 1D mass flow rate value would not be sufficient to have a fully developed flow in the reduced domain equivalent to that of the entire channel. Therefore, it is necessary to read the profiles in the cross section of the entire channel that correspond to the inlet section in the reduced domain.
In particular, the total temperature inlet and velocity inlet vector components have been read in a plane placed exactly at the axial distance of 2.775 meters from the channel entrance from the results of the simulation with Reynolds stress and medium mesh. The profiles have then been imported into the optimization case setup and set as inlet boundary conditions. In the entire channel domain, only one quarter of the transversal section is considered, so the profiles extracted are only for one

quarter, while in the optimization domain, half of the cross section is simulated. It is necessary to mirror one quarter section profiles to obtain half section profiles, this can be done by attributing the same values of velocity and total temperature at the mirrored coordinates with respect to axis z.

In particular, two profile files are written from the entire channel domain in the perpendicular section at the axial coordinate y=2.775 m. One file contains velocity values and the other total temperature values for the respective coordinates x and z, but only for one quarter section. Then for the same x coordinate and the z coordinate with negative sign the same values of velocity and temperature are assigned. The profiles are shown in Figures 5.3 and 5.4.

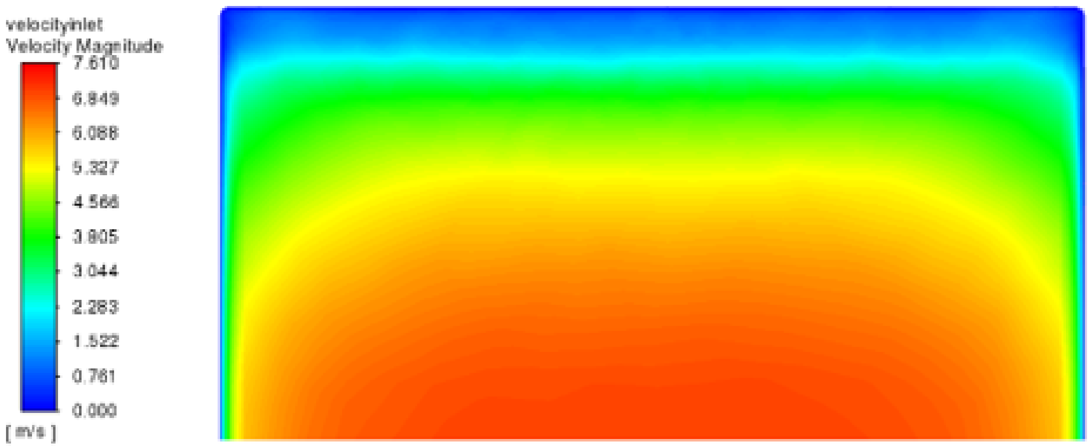

Figure 5.3: Velocity profile applied at the inlet of the optimization domain, $y = 2.775\ m$

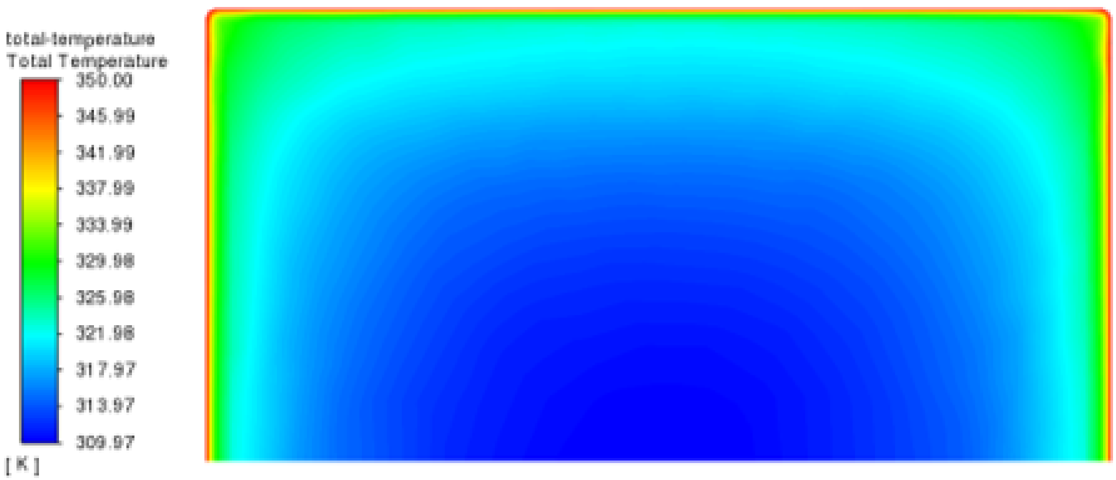

Figure 5.4: Total temperature profile applied at the inlet of the optimization domain, $y = 2.775\ m$

5.1.3 Case setup

The setup is the same as for the validation activity, with the same solver settings and air properties. The only turbulence model implemented is the Reynolds Stress model, which was chosen in the validation process. The flow conditions considered are $Re = 21500$ and $Re = 42000$.

5.1.4 Optimization domain baseline comparison with the entire domain: Re=21500

In order to confirm the boundary conditions imposed at the inlet of the optimization domain, it is necessary to compare the results of the optimization domain with the reference results of the entire channel in terms of thermal performance to confirm that the results are equivalent, the boundary conditions are coherent and the profiles have been correctly imported from the reference case.
Planes and iso-surfaces, perpendicular to the main flow, were created to compare results of the optimization domain with those of the entire channel. Slices are realized only in the heated region, progressively at an axial pitch of 0.002 meter between each other. The axial discretization and the process are equal to the validation campaign.

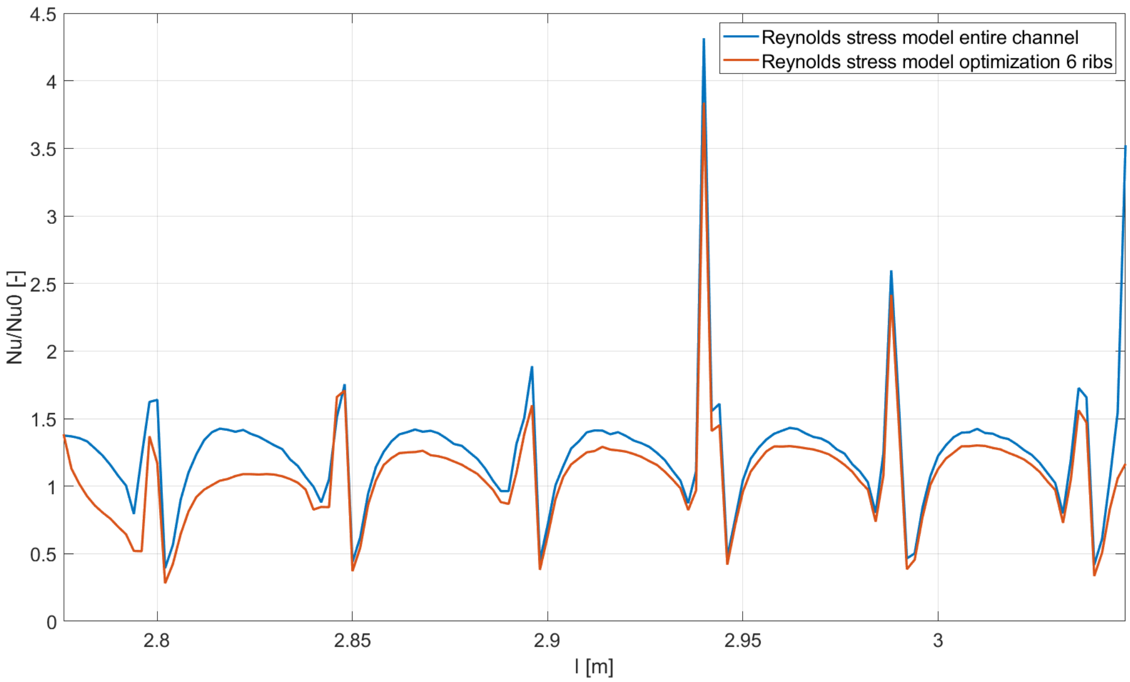

Figure 5.5: Comparison of optimization domain Nusselt ratio results with the entire channel, $Re = 21500$

In Figure 5.5, a comparison is shown between the optimization domain results and the entire channel results. The results are very similar in the last four ribs in terms of profile, but slightly lower in values for the optimization domain. In the first two ribs, the heat transfer profile of the reduced domain is visibly lower than the entire channel profile and does not reproduce the same trend along the first two rib pitches. From the third rib, the flow is developed and the optimization domain correctly represents the heat transfer profile along a rib pitch. For this reason, it has been decided to optimize only the last four ribs of the heated region, where the flow is fully developed.

5.1.5 Optimization domain baseline comparison with the entire domain: Re=42000

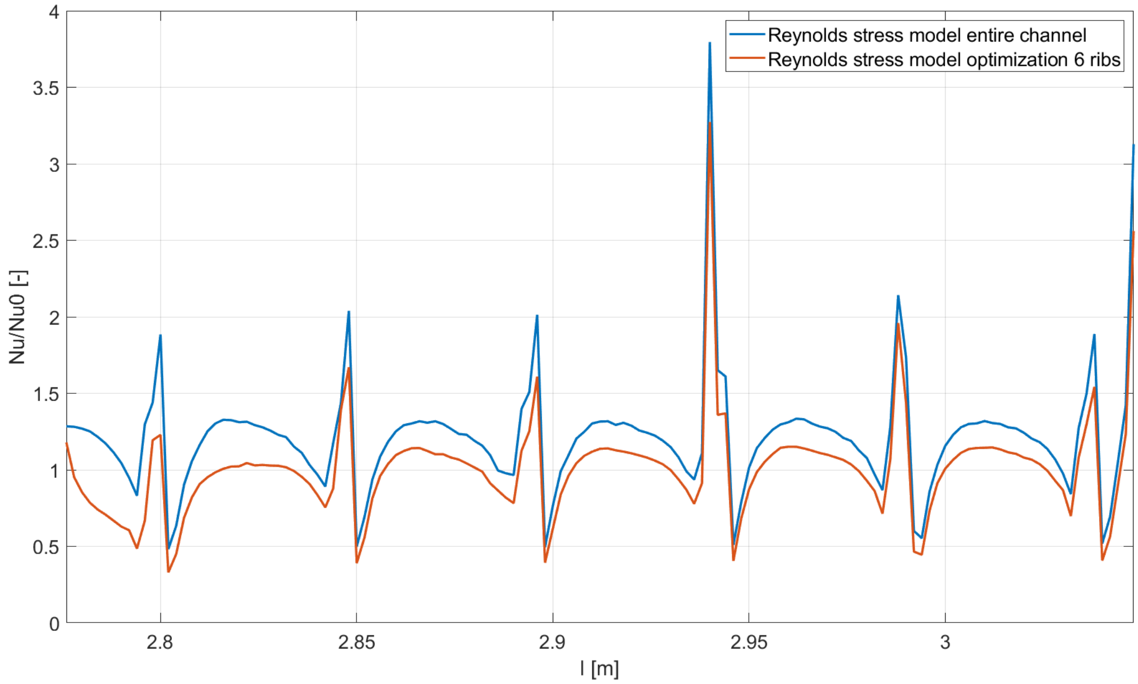

Figure 5.6: Comparison of optimization domain Nusselt ratio results with the entire channel, $Re = 42000$

In Figure 5.6, the Nusselt ratio profile of the optimization domain is compared with the results of the entire channel under $Re = 42000$. The same considerations of the $Re = 21500$ case are valid for the results under more turbulent conditions $Re = 42000$. The Nusselt ratio profile is slightly lower in the optimization domain for the first two ribs, but from the third rib the results are very similar to those of the entire channel. Therefore, the boundary conditions applied are coherent and the reduced domain has been selected for optimization.

5.2 Optimization region

After confirming that the reduced domain comprising the last six ribs has equivalent results compared to the entire channel, the next step is to optimize the shape of the ribs and walls to obtain the best heat transfer performance. The domain described in Section 5.1 represents the baseline for the optimization process; its isometric view is shown in Figure 5.7.

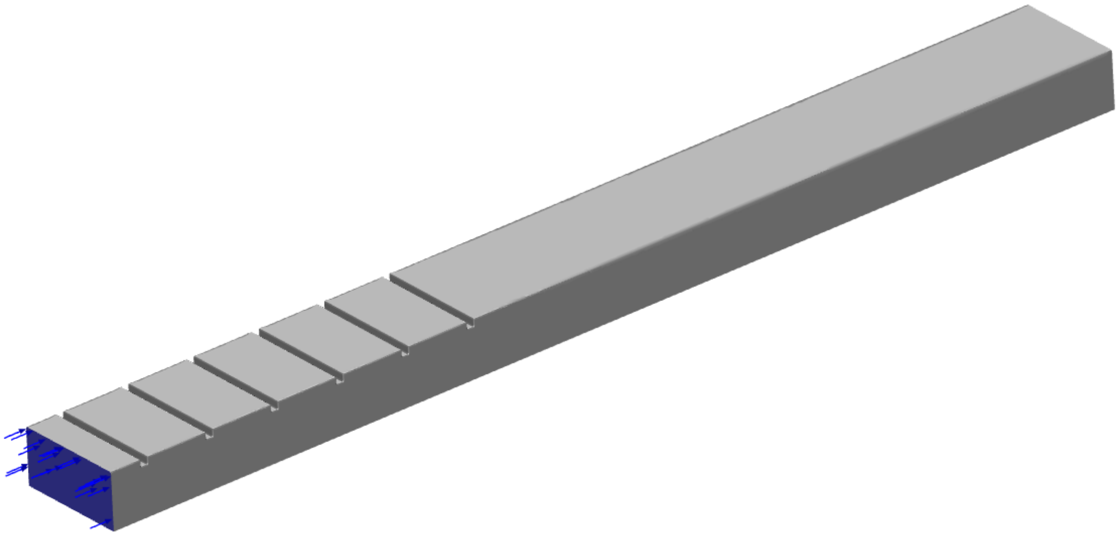

Figure 5.7: Baseline optimization domain

From the reduced domain of six ribs, it was chosen to optimize only a limited region, which comprises the last four ribs of the heated region (Figure 5.8). Considering a smaller portion consents to obtain more accurate results with less computational time, in fact each adjoint iteration is expensive because it requires a lot of CFD iterations to solve the RANS equations, then the adjoint iterations to calculate the new geometry.

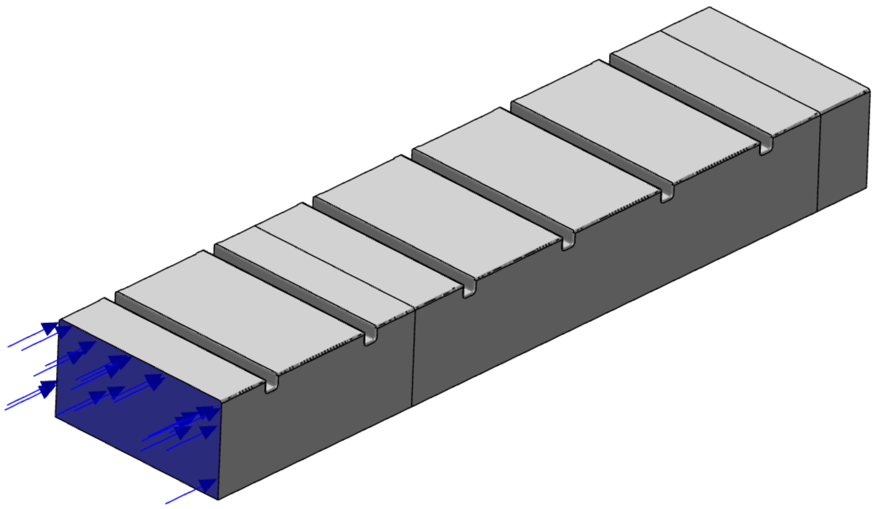

Figure 5.8: Optimization region, only the zone delimited by the black lines have been optimized

5.3 Adjoint setup

5.3.1 Observables

The first step of an adjoint calculation is the definition of one or more observables. The observables are the quantities of interest that could be maximized or minimized during the calculation process. In this work, the main observable is the convective heat transfer coefficient HTC, the other defined observables are the terms needed to calculate the main observable.
The objective function HTC is calculated as:

$$HTC = \frac{\dot{Q}}{T_{wall} - T_{bulk}} \tag{50}$$

where $T_{wall} = 350\ K$ is the wall boundary condition and T_{bulk} is calculated as:

$$T_{bulk} = \frac{T_{in}^0 + T_{out}^0}{2} \tag{51}$$

where $T_{in}^0 = \frac{\sum m_{in} T_{in}^0}{m_{tot}}$ and $T_{out}^0 = \frac{\sum m_{out} T_{out}^0}{m_{tot}}$

5.3.2 Adjoint solver settings

The adjoint solver settings are reported in the last column of Table 13, compared to the CFD settings.

	flow solver	**adjoint solver**
gradient	Least Squares Cell Based	Green-Gauss cell based
pressure	Second Order	Standard
momentum	Second Order Upwind	First Order Upwind

Table 13: Adjoint Solver options

These are the default settings in the Ansys tool and are the most simple choices to obtain a faster solution with fewer computational resources. In fact, the adjoint optimization could be quite expensive with a more complex discretization, because each iteration consists of two processes:

- classical CFD iterations, to solve the flow in the domain through the RANS equations
- adjoint iterations, to calculate the gradients of the objective functions

After calculating the gradients, the mesh is deformed through a mesh morphing tool, and consequently the geometry changes together with the mesh, in order to reach the imposed relative improvement of the objective functions. Thanks to the mesh morphing tool, the geometry cannot drastically change from the baseline configuration and the main structure is preserved. The gradient-based optimizer requests one or more observables to be optimized, and the percentage of improvement between each iteration. In this case, the observable of interest is HTC, and its maximization has been established between $1 - 5\%$ at each iteration. This percentage cannot be too high in order to maintain a certain mesh quality. In this case, the main settings for the adjoint optimization process are summarized in Table 14.

number of flow iterations	2000
number of Adjoint iterations	300
Convergence criteria	0.005
Minimum orthogonality	0.005

Table 14: Adjoint optimization parameters

5.3.3 Design change and Mesh morphing

The mesh morphing zone has been reduced to only a limited height from the ribbed wall to not excessively deform the walls, especially near the symmetry plane.
The zones to be optimized are the ribs from the third to the sixth, the ribbed side and the smooth side, but only the region included in the meshing box with coordinates in Table 15.

x_{min} $[m]$	x_{max} $[m]$	y_{min} $[m]$	y_{max} $[m]$	z_{min} $[m]$	z_{max} $[m]$
0.02	0.044	2.86	3.08	-0.0475	0.0475

Table 15: Meshing box coordinates, where the geometry is optimized

The morphing method used is the Radial Basis Function. This option is usually recommended when some zones need to stay fixed and for better output mesh quality. In Figures 5.9 and 5.10, the lateral and top views of the mesh morphing box are shown.

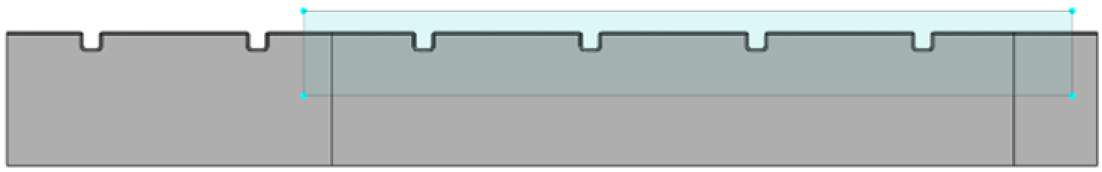

Figure 5.9: Mesh morphing box, lateral view

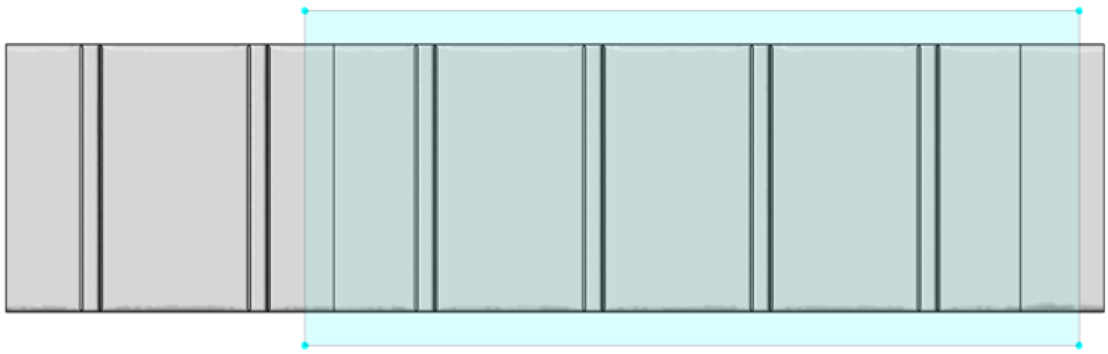

Figure 5.10: Mesh morphing box, top view

6 Postprocessing of the adjoint-based optimization results

6.1 Results Re=21500, after 19 iterations

6.1.1 Adjoint optimization history

The adjoint optimization history for the first 19 iterations is reported in Figure 6.1.

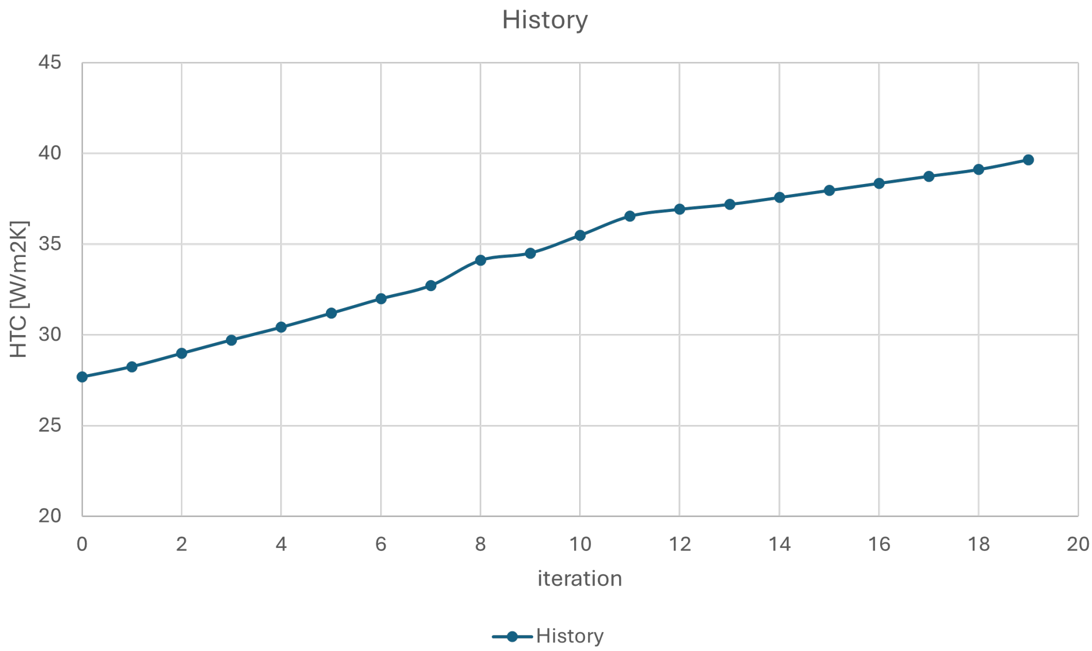

Figure 6.1: Adjoint optimization history after 19 iterations, $Re = 21500$

The increments of HTC between each iteration cannot be excessively high, because the mesh would be rapidly deformed and in a few iterations the mesh quality would be too poor. Therefore, the increments between iterations vary between $1 \div 5\%$. In Table 16, the increase of HTC, after the first 19 iterations, is shown.

$HTC_{baseline}$ $[W/m^2K]$	$HTC_{after19iterations}$ $[W/m^2K]$	$HTC_{19}/HTC_{baseline}$
27.7	39.7	1.43

Table 16: HTC increment after 19 iterations, $Re = 21500$

The optimization stopped not because of having reached the optimal configuration, but because of poor mesh quality. In particular, the minimum mesh orthogonality of 0.005 was not satisfied after the 19th iteration.

6.1.2 Optimized geometry after 19 iterations

In Figures 6.2, 6.3 and 6.4, the optimized geometry after 19 iterations is reported in top, lateral and isometric views, respectively.
The frontal view of the four ribs is shown in Figures 6.5, 6.6, 6.7 and 6.8; an isometric view of the four ribs is reported in Figure 6.8, to better visualize their similarities and differences.

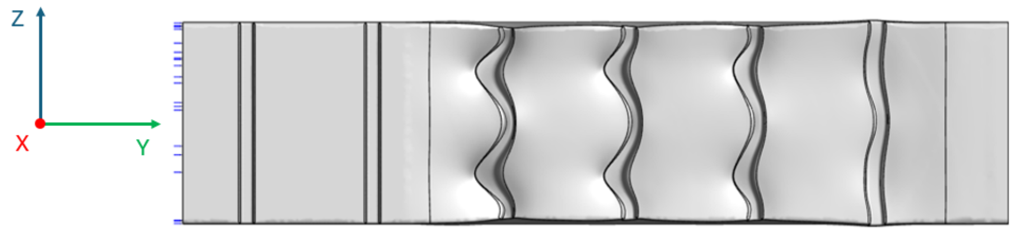

Figure 6.2: Optimized geometry after 19 iterations, $Re = 21500$, top view

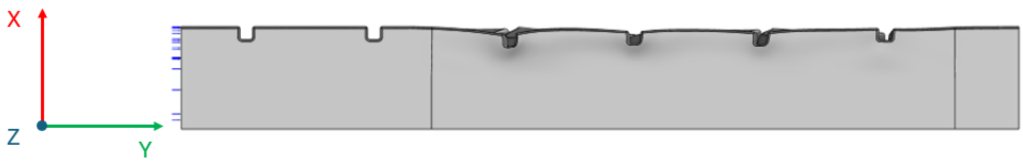

Figure 6.3: Optimized geometry after 19 iterations, $Re = 21500$, lateral view

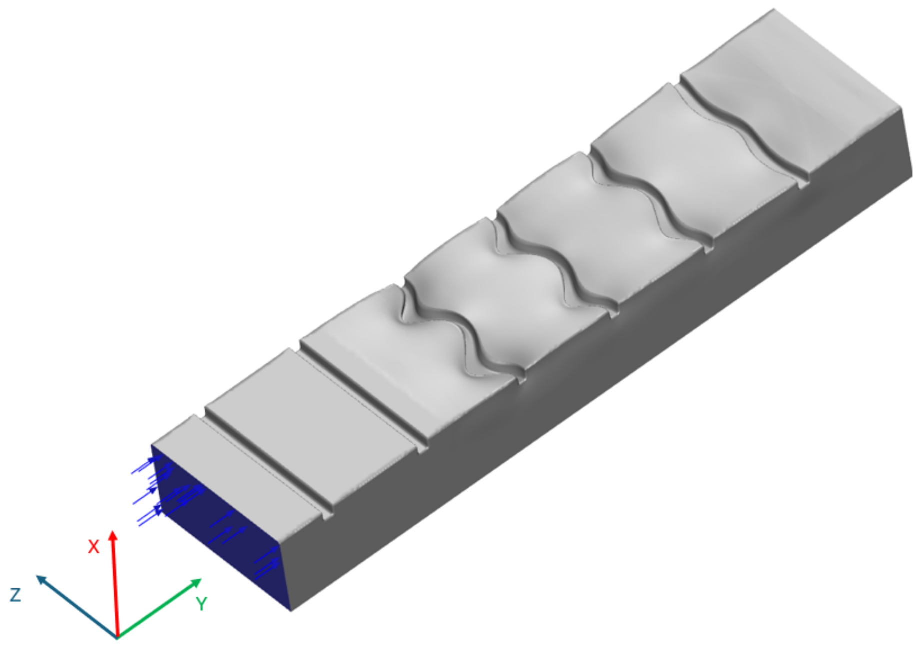

Figure 6.4: Optimized geometry after 19 iterations, $Re = 21500$, isometric view

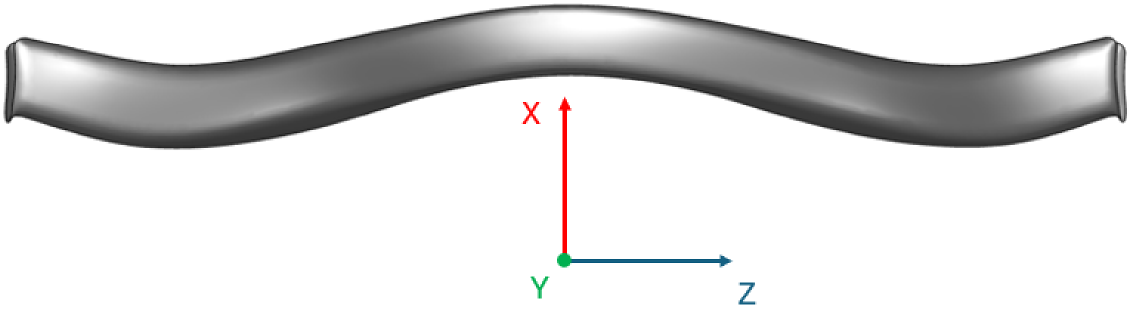

Figure 6.5: Optimized rib 1 after 19 iterations, $Re = 21500$, frontal view

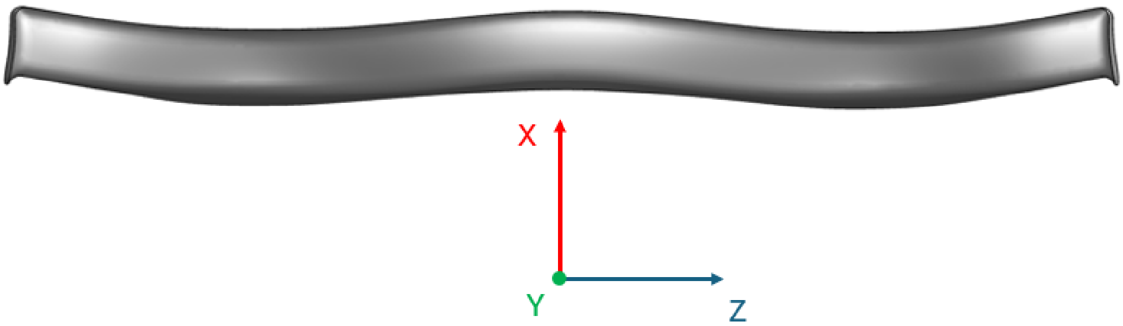

Figure 6.6: Optimized rib 2 after 19 iterations, $Re = 21500$, frontal view

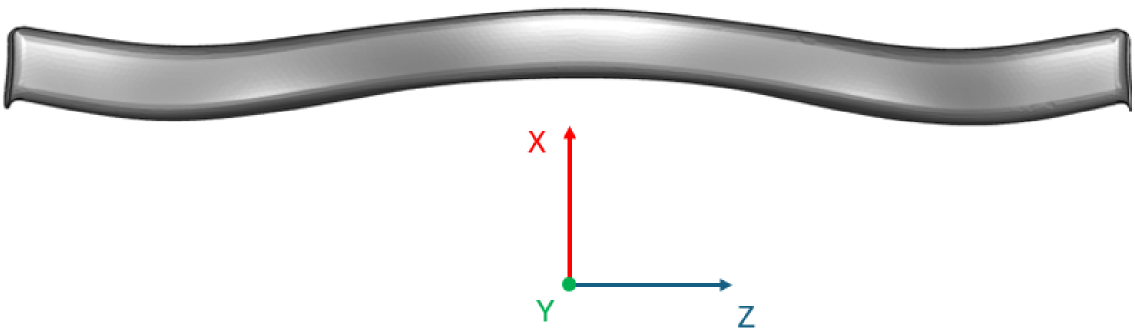

Figure 6.7: Optimized rib 3 after 19 iterations, $Re = 21500$, frontal view

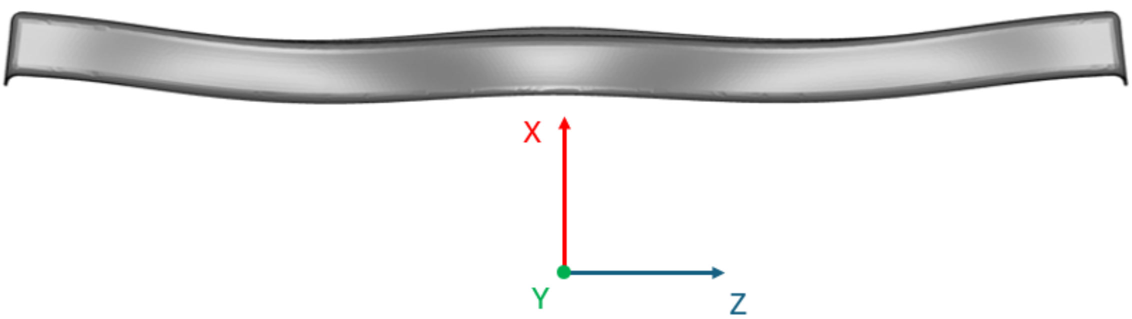

Figure 6.8: Optimized rib 4 after 19 iterations, $Re = 21500$, frontal view

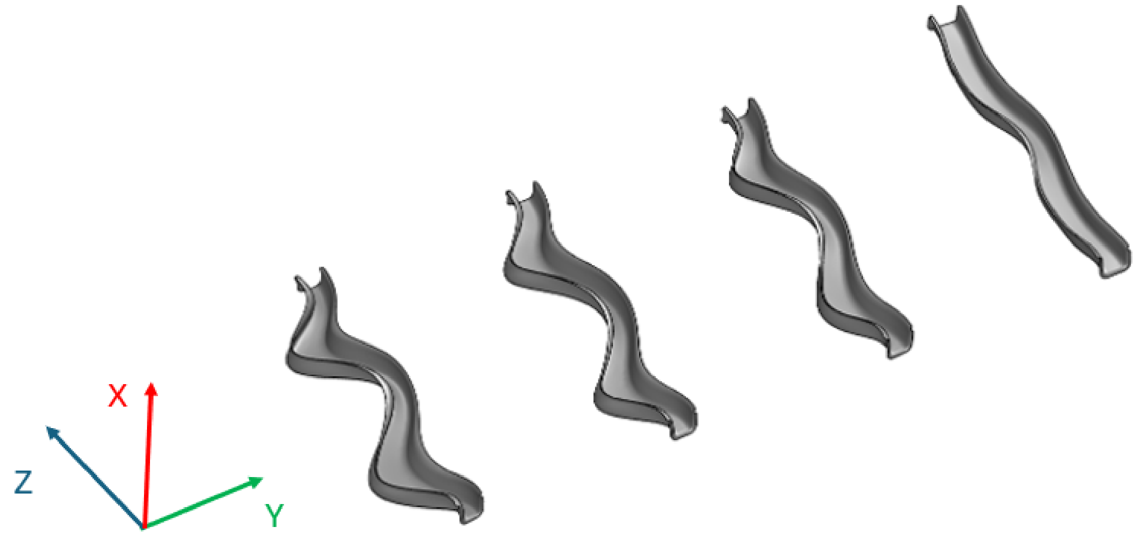

Figure 6.9: Optimized ribs after 19 iterations, $Re = 21500$, frontal view

The first optimized rib is more curved compared to the following because it influences the downstream flow and its thermal performance. A periodicity can be seen where one rib is wavier (first and third ribs) and the following has a more regular shape (second and fourth ribs), this can be the starting point for a successive parametrization. All optimized ribs assume a wavy shape, which is generally called w-shape in the literature. This shape is characterized by a central valley and two lateral peaks, in both frontal and axial directions, and the symmetry of each rib is conserved. This consents to create counter rotating eddies that push the flow to the walls; therefore, it leads to an improved heat exchange between the external hot gases and the internal cool air. The channel walls, in particular the ribbed wall, follow the same pattern as the optimized ribs, with a w-shaped cross section that periodically changes in height.

6.1.3 Vorticity effects on heat transfer

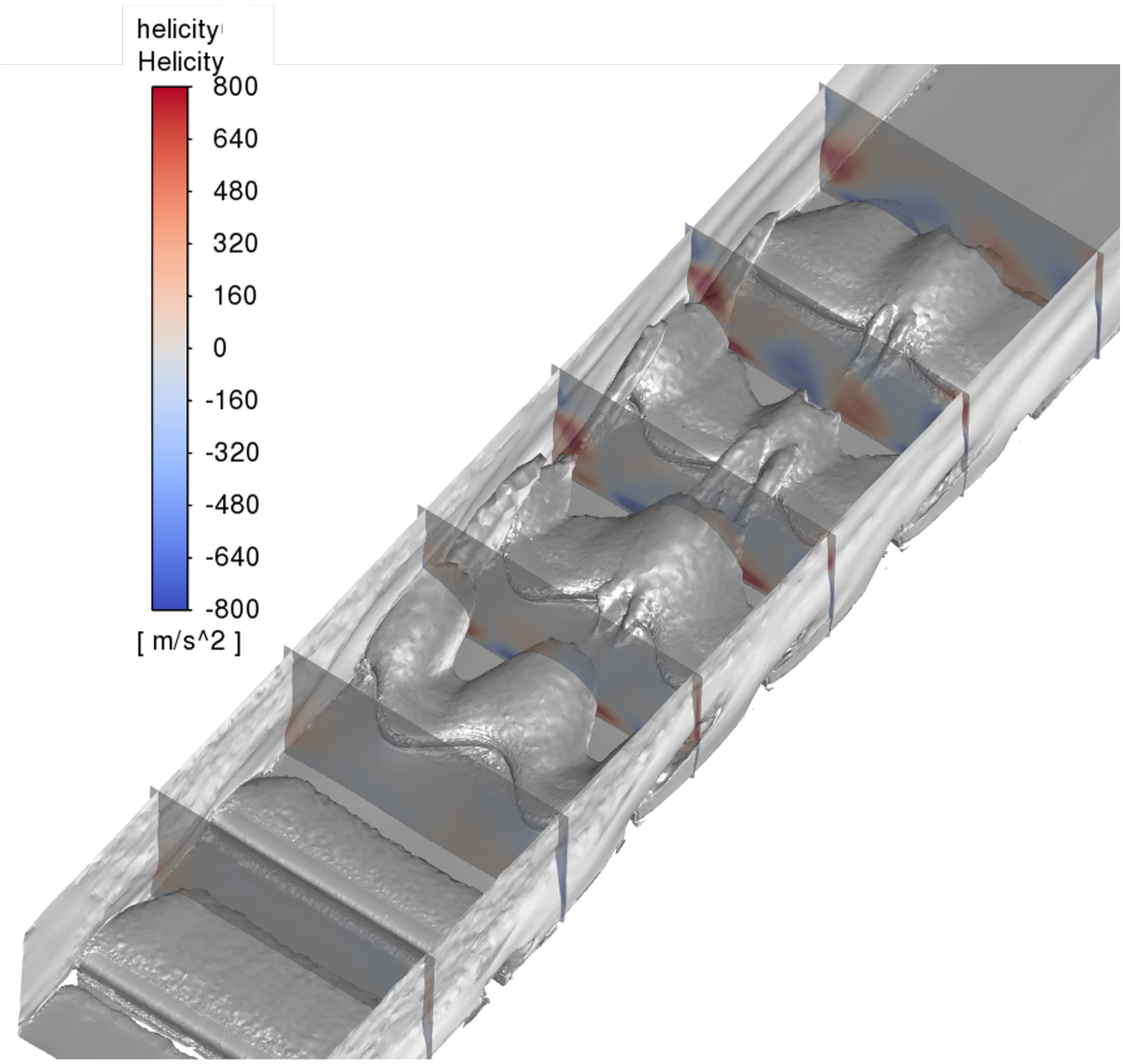

Figure 6.10: Vorticity induced by optimized ribs, 19 iterations, $Re = 21500$

In Figure 6.10, it can be seen that after the first two ribs, which have not been optimized, a regular recirculation zone is generated, then the flow reunites and proceeds normally. Instead, after the last four ribs, which have been optimized, the flow assumes a much more irregular configuration. In particular, four main eddies are generated by the new ribs geometry: two clockwise rotating eddies (red) and two counterclockwise rotating eddies (blue). One clockwise eddy is directed at the angle between the ribbed wall and one smooth wall, meanwhile, one counterclockwise eddy is pointed to the angle between the ribbed wall and the second smooth wall. The other two eddies, one clockwise and the other counterclockwise, are rotating symmetrically in two regions between the smooth walls and the ribs symmetry plane. In Figure 6.11, the heat flux contour shows that, for each rib pitch, the maximum values of heat flux are reached in two symmetric portions located in the middle between a smooth wall and the symmetry plane of the ribs. In Figure 6.12, it can be seen that for each optimized rib pitch, the two portions of the ribbed wall where the heat flux is higher are the zones where two counter rotating eddies meet (one

clockwise and the other counterclockwise), the coolant is dragged to the ribbed wall. In this way, the coolant is more in contact with the walls for a longer time, and the heat transfer increases significantly. This phenomenon is shown more clearly in Fig. 6.13 for a specific rib interval.
Moreover, the two vortices at the corners between the smooth walls and the ribbed walls lead to the generation of impingement jets on the smooth walls, this can be seen in Figures 6.12 and 6.13, where the heat flux is higher on the smooth wall after the optimized ribs. Helicity is a measure of the rotation of the fluid about an axis parallel to the main flow.

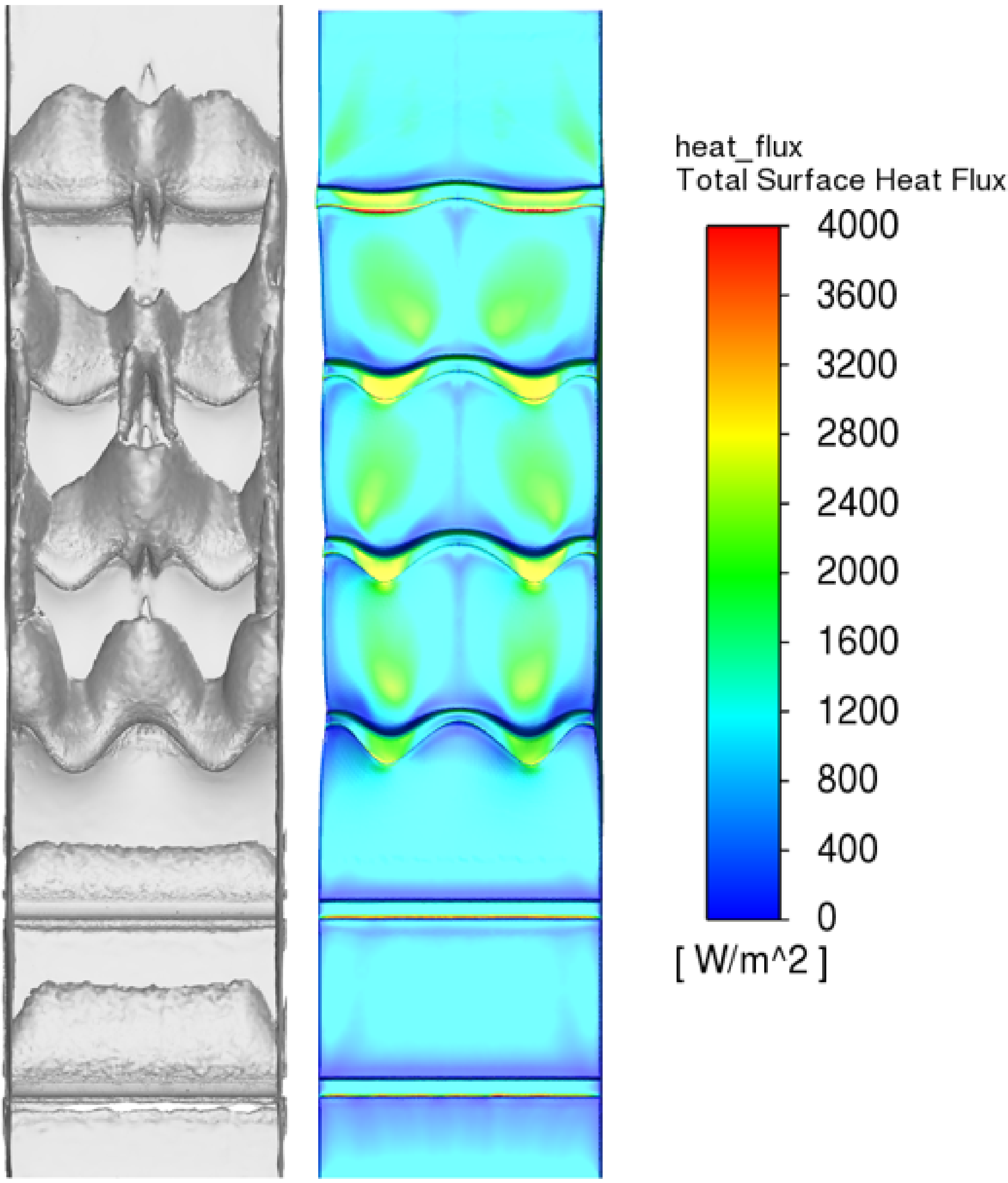

Figure 6.11: Vorticity and heat transfer enhancement induced by optimized ribs, 19 iterations, $Re = 21500$

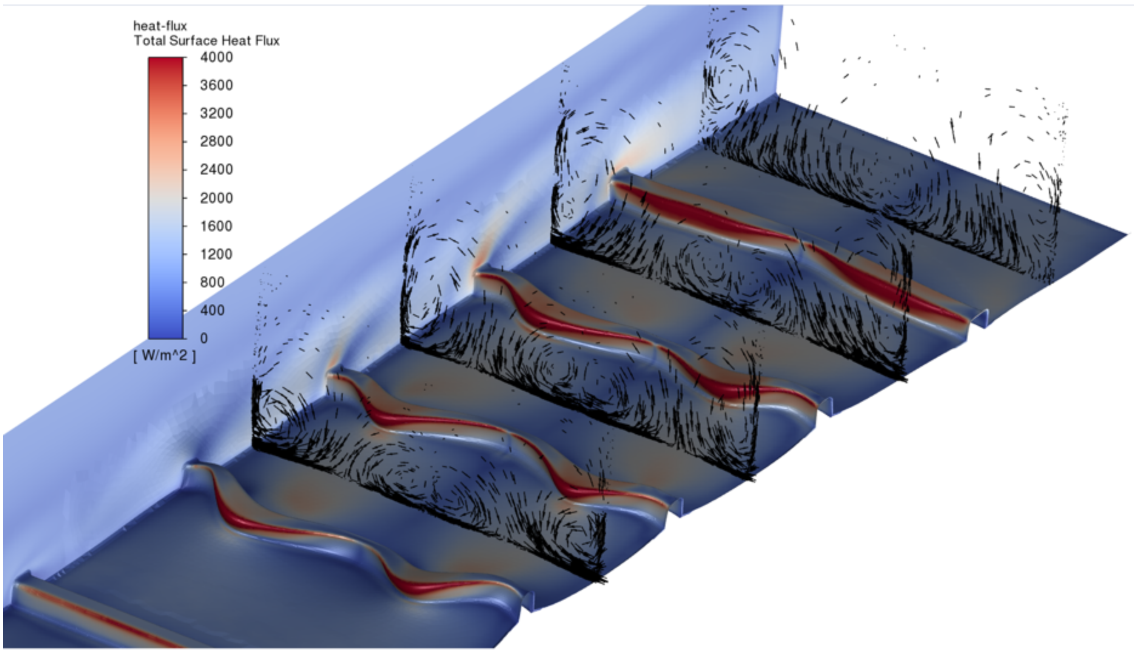

Figure 6.12: Heat transfer enhancement and eddies induced by optimized ribs, 19 iterations, $Re = 21500$

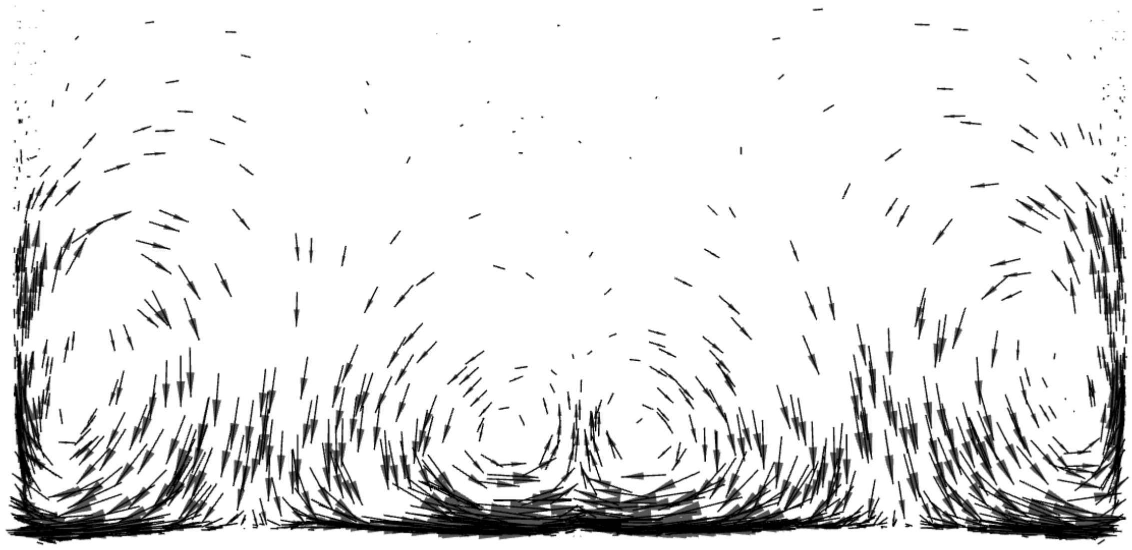

Figure 6.13: Helicity vectors in a plane perpendicular to the main flow in the middle of the interval between ribs 4-5, $y = 2.966m$, 19 iterations, $Re = 21500$

6.2 Remeshing, Re=21500, after 19 iterations

The adjoint optimization stopped after 19 iterations, as stated in the previous paragraph, not because the solver had reached an optimal solution, but because of poor mesh quality. In fact, the solution after 19 iterations has not reached convergence, but the mesh has been excessively deformed and it does not respect anymore the minimum orthogonality of 0.005 imposed before launching the optimization. Especially near the most modified ribs, the mesh elements are more irregular and perturbed compared to the baseline mesh.
Therefore, in order to proceed with further iterations to obtain better thermal performance results, it is necessary to extract the optimized geometry after 19 iterations and create a new mesh. This process is complicated by the possibility of extracting the geometry only in an STL file. An STL file is the simplest way to represent a geometry; the geometry is discretized into tetrahedrons or triangles, in 3D or 2D respectively. The STL format is not the preferred format for CAD software, this also applies for Ansys Design Modeler and Ansys SpaceClaim, which have been utilized in this activity. The first step for the remeshing process is to import the STL file into Ansys SpaceClaim, which is more suitable for refining a geometry compared to Design Modeler, because it has more complex and complete functions and tools. In SpaceClaim, the geometry after 19 iterations discretized into tetrahedrons in the STL file, has been merged into one single volume. After obtaining the geometry in a unique volume, it is ready for remeshing. With the help of Ansys Meshing, a new mesh has been generated to meet the mesh quality requirements. Finally, the remeshed geometry is updated in Fluent solver and, after setting the boundary conditions and the simulation setup, the adjoint optimization is launched again. The updated results are shown in the following paragraph.
In Figure 6.14, the mesh before remeshing after 19 iterations is compared to the new mesh after the remeshing process. The slight difference in geometry after remeshing can be seen near the ribs, the surface is slightly deformed by the process of merging the STL file tetrahedrons.

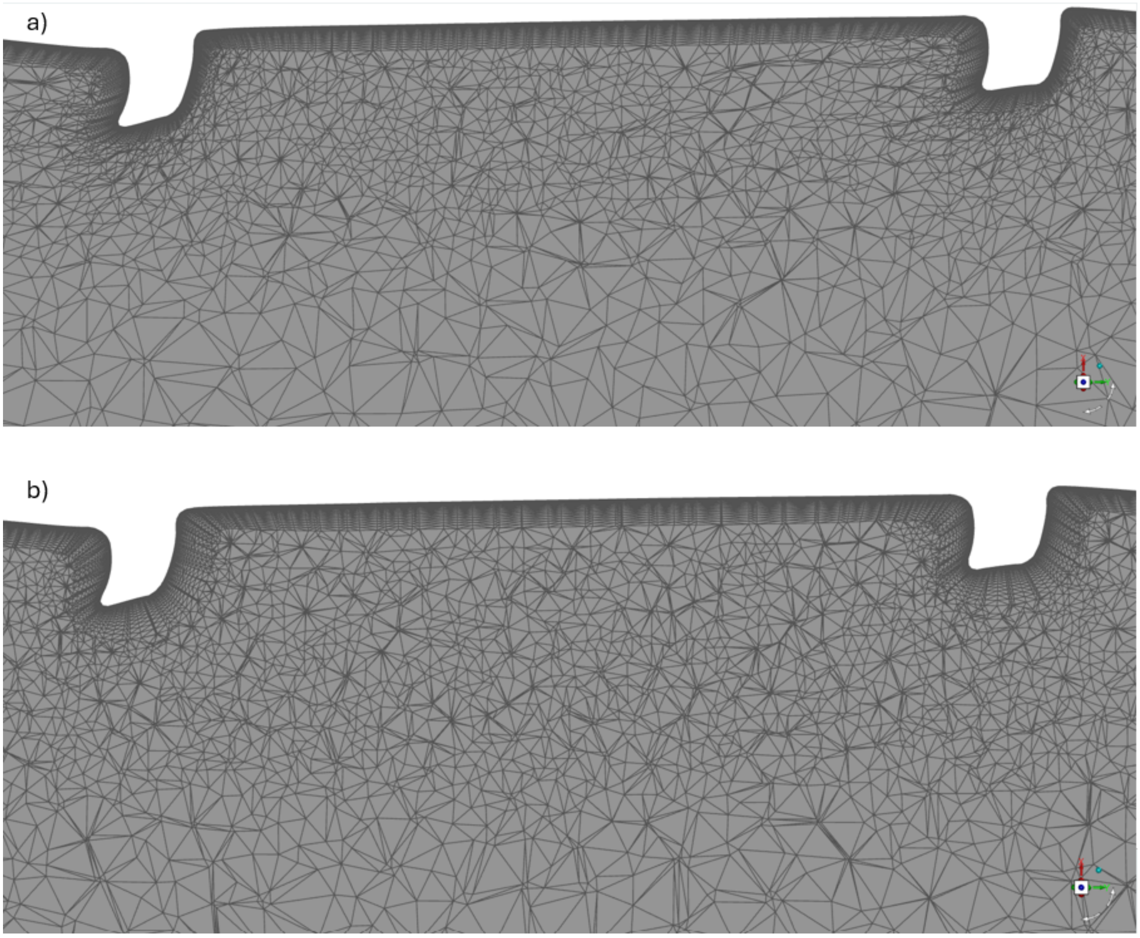

Figure 6.14: Mesh deformed before a) and after b) remeshing, $Re = 21500$, view of mesh near second and third optimized ribs in longitudinal XY plane (ribs plane of symmetry)

6.3 Results Re=21500, after 32 iterations

6.3.1 Adjoint optimization history

After another 13 iterations, for a total 32 iterations, the adjoint optimization terminated due to reached convergence. The adjoint history for all the iterations is shown in Figure 6.15.

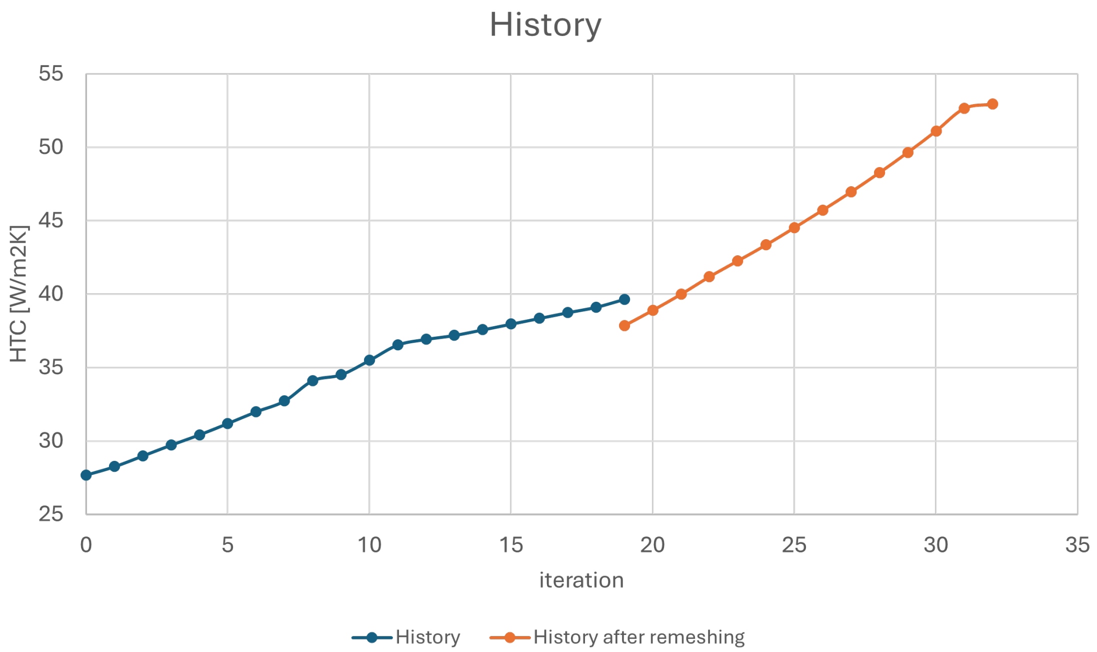

Figure 6.15: Adjoint optimization history after 32 iterations, $Re = 21500$

$HTC_{baseline}$ $[W/m^2K]$	$HTC_{19remeshed}$ $[W/m^2K]$	HTC_{32} $[W/m^2K]$	$HTC_{32}/HTC_{baseline}$
27.7	37.9	52.9	1.91

Table 17: HTC increment after the total 32 iterations, $Re = 21500$

In Table 17, the increase of HTC is shown. The average HTC of the optimized region after remeshing is slightly different from the average HTC after 19 iterations. The reason is probably the poor accuracy of the deformed mesh. At the end of the 32 iterations, the HTC value is almost twice the baseline value.

6.3.2 Optimized geometry after 32 iterations

In Figures 6.16, 6.17 and 6.18, the optimized geometry after 19 iterations is reported in top, lateral and isometric views, respectively.
The frontal view of the four ribs is shown in Figures 6.19, 6.20, 6.21 and 6.22; an isometric view of the four ribs is reported in Figure 6.23, to better visualize their similarities and differences.

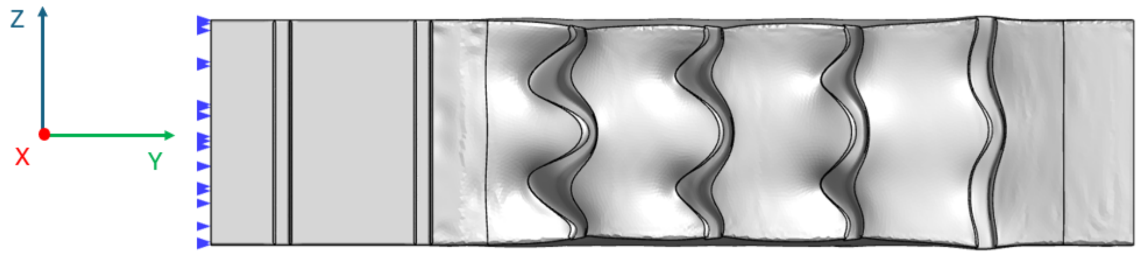

Figure 6.16: Optimized geometry after 32 iterations, $Re = 21500$, top view

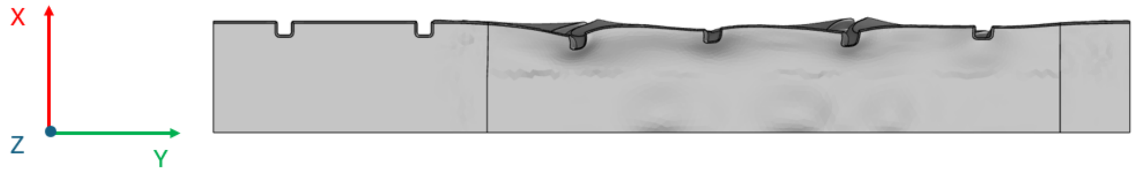

Figure 6.17: Optimized geometry after 32 iterations, $Re = 21500$, top view

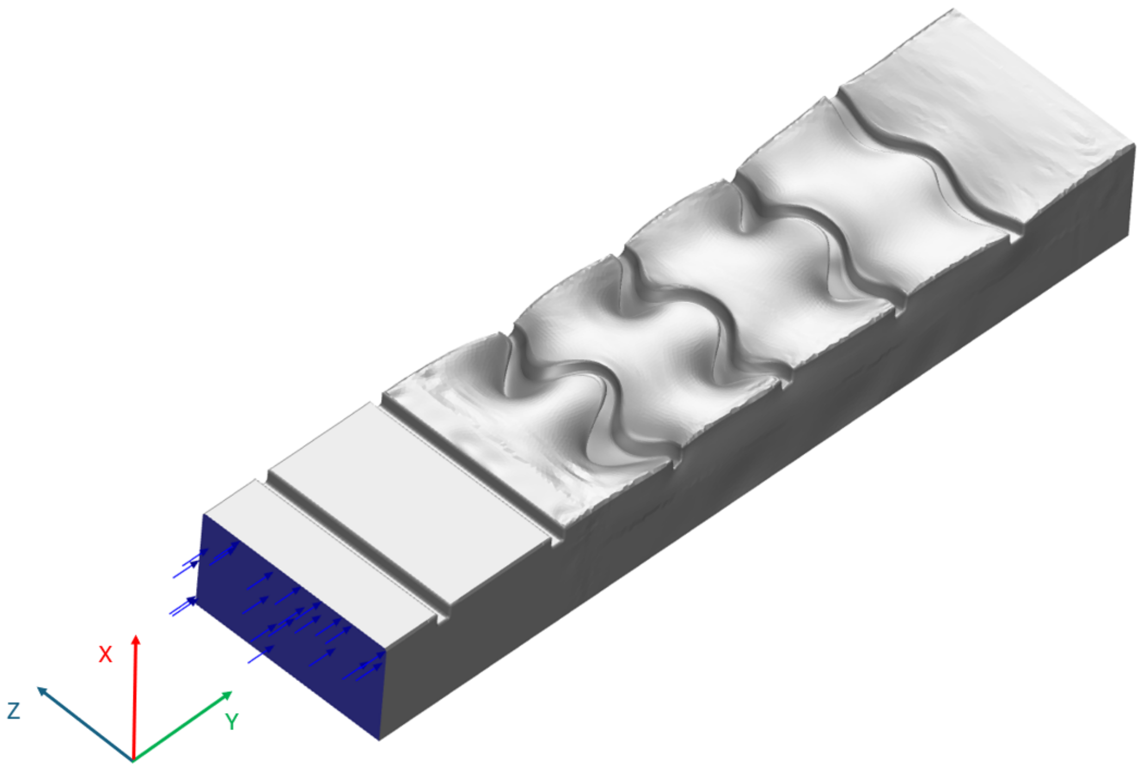

Figure 6.18: Optimized geometry after 32 iterations, $Re = 21500$, isometric view

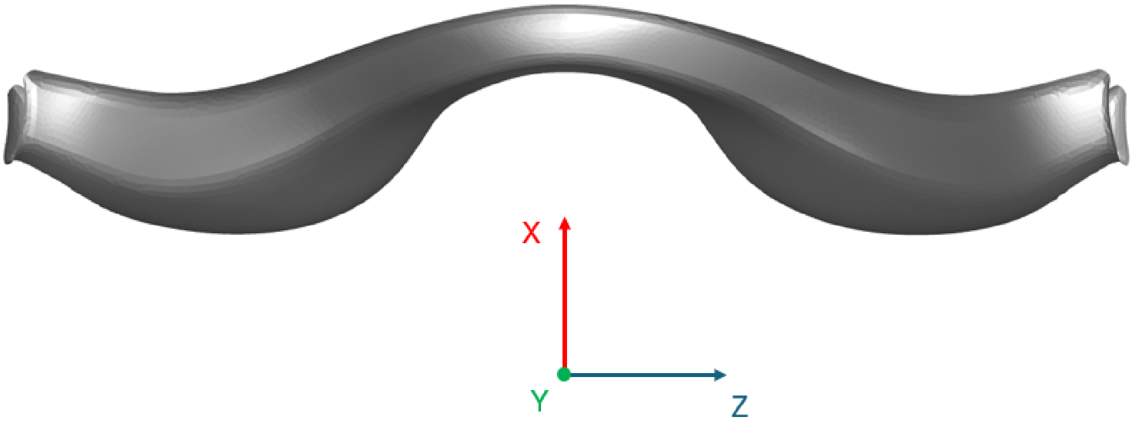

Figure 6.19: Optimized rib 1 after 32 iterations, $Re = 21500$, frontal view

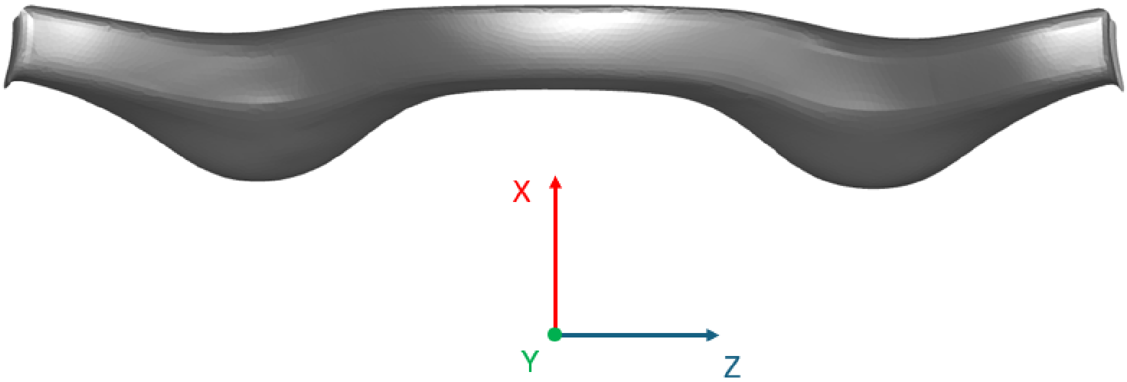

Figure 6.20: Optimized rib 2 after 32 iterations, $Re = 21500$, frontal view

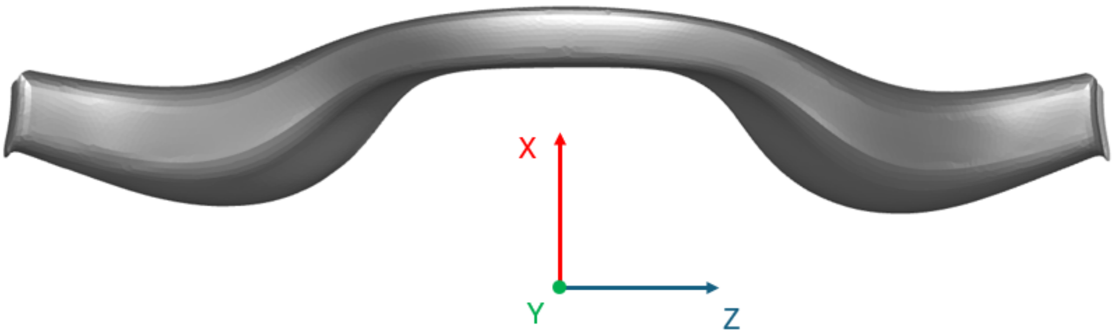

Figure 6.21: Optimized rib 3 after 32 iterations, $Re = 21500$, frontal view

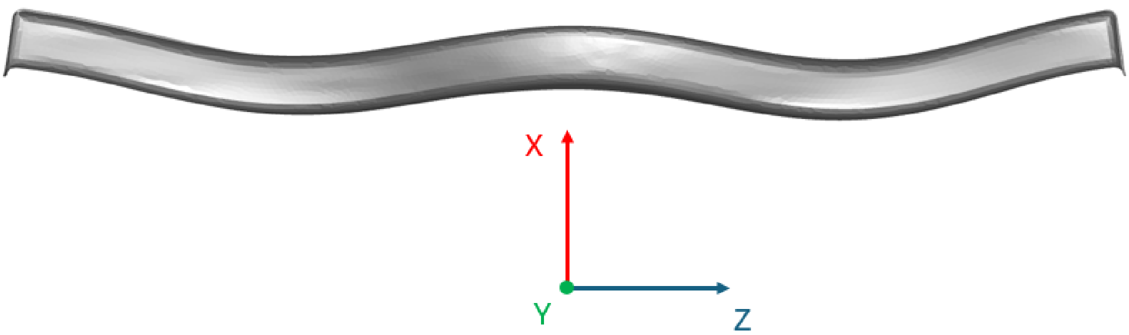

Figure 6.22: Optimized rib 4 after 32 iterations, $Re = 21500$, frontal view

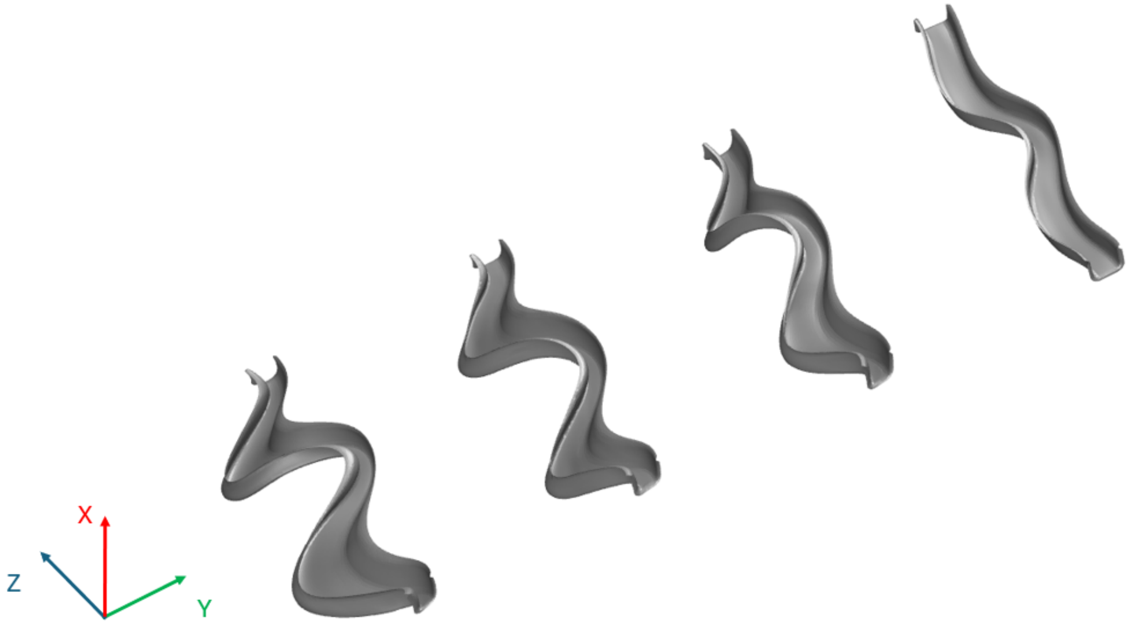

Figure 6.23: Optimized ribs after 32 iterations, $Re = 21500$, isometric view

The four optimized ribs are overall similar to the ribs after 19 iterations. The first and third ribs are more deformed than the second and fourth ribs. The fourth rib is more irregular than after 19 iterations, where it was slightly deformed from the baseline. The main difference is the larger deformation of the four ribs in the axial direction, which can be seen in the isometric view. This feature allows for the formation of the eddies and the flow contact with the ribbed wall to be extended both spatially and temporally.

6.3.3 Vorticity effects on heat transfer

In Figure 6.24, it can be seen that the same eddies structure described for the geometry after 19 iterations is found in the 32 iteration case, but this time they are more emphasized. The updated shape of the ribs leads to a higher overall heat exchange (Figure 6.25), but in particular in the two regions of the ribbed wall where the two counter rotating eddies drive the coolant to the same wall. In Figures 6.26 and 6.27, it can be seen that the counter rotating eddies generated by the w-shaped ribs are more intense after 32 iterations.
The impingement on the smooth walls is visible in Figure 6.26, where the heat flux increases after the optimized ribs. After 32 iterations, this phenomenon is more pronounced compared to the first 19 iterations.

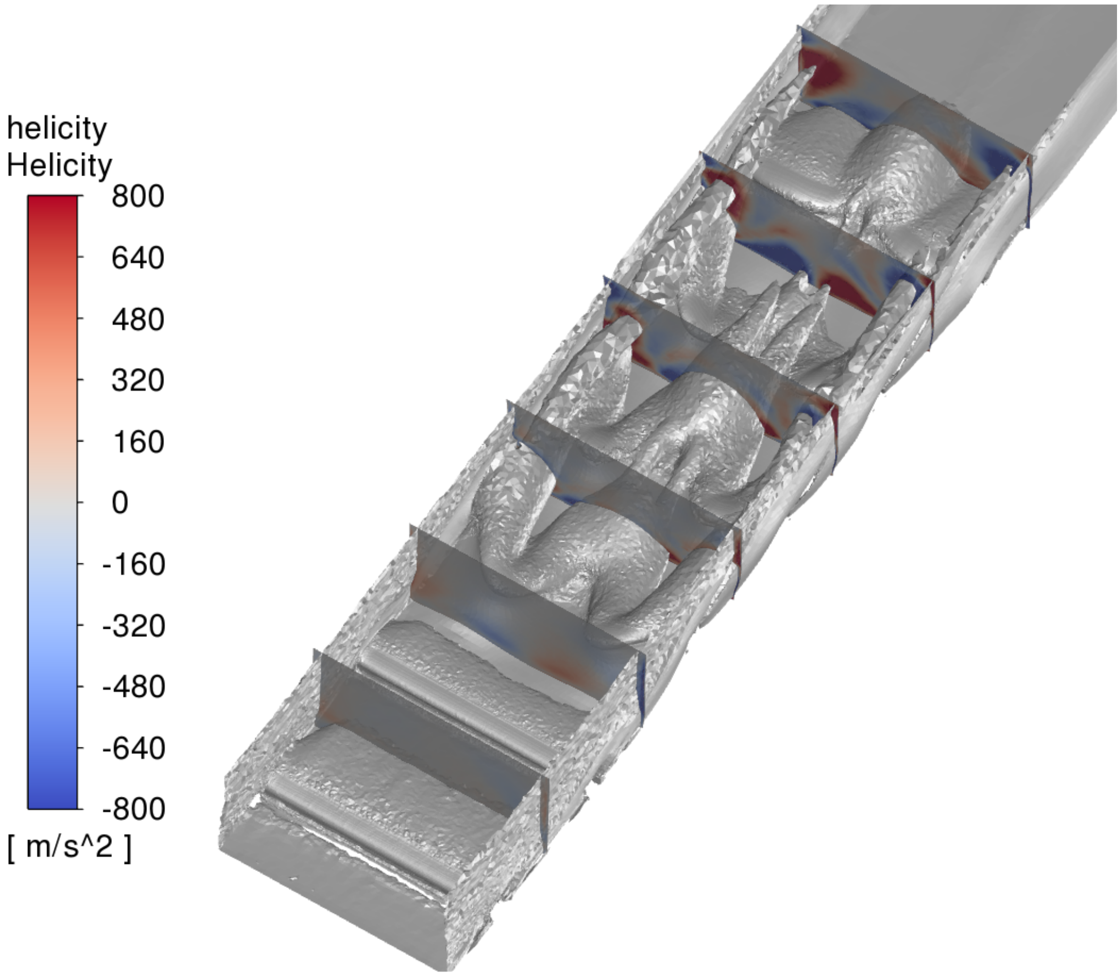

Figure 6.24: Vorticity induced by optimized ribs, 32 iterations, $Re = 21500$

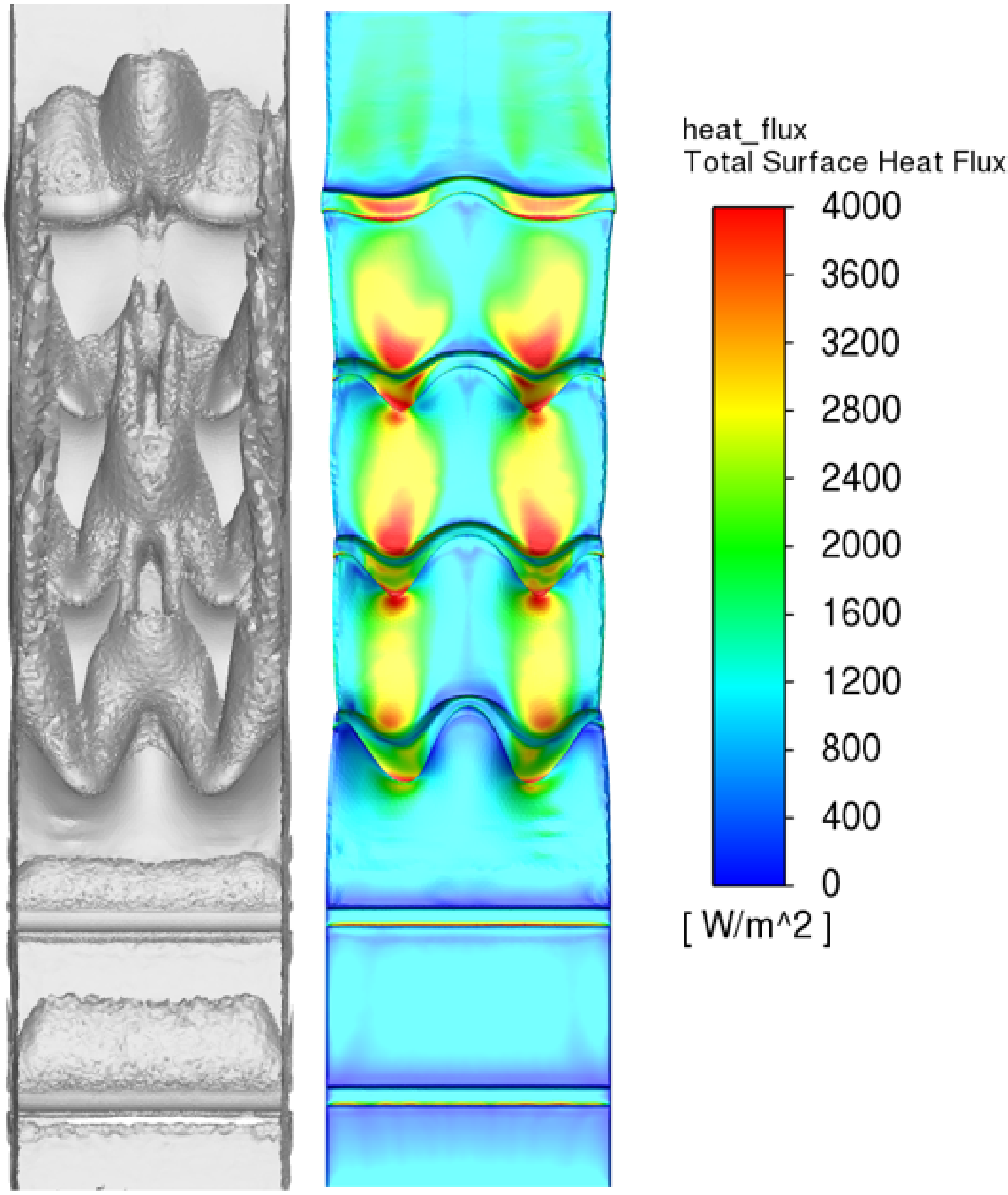

Figure 6.25: Vorticity and heat transfer enhancement induced by optimized ribs, 32 iterations, $Re = 21500$, top view

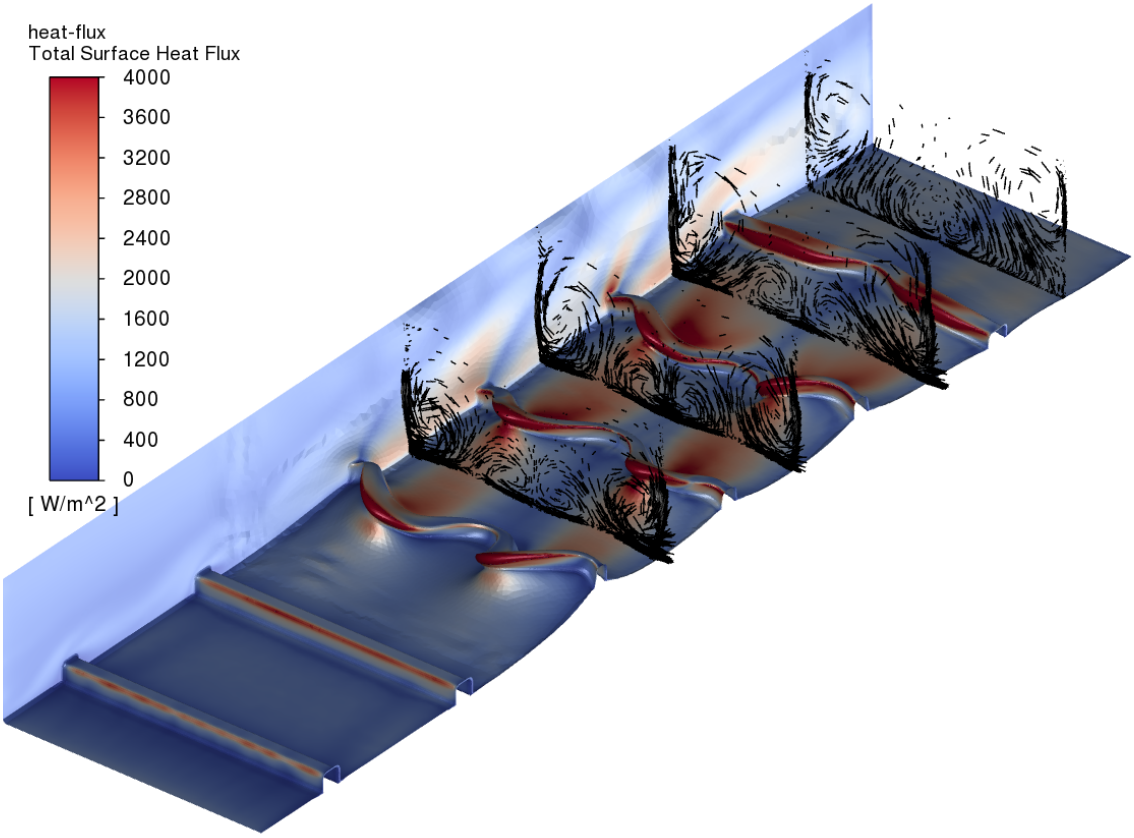

Figure 6.26: Heat transfer enhancement and eddies induced by optimized ribs, 32 iterations, $Re = 21500$

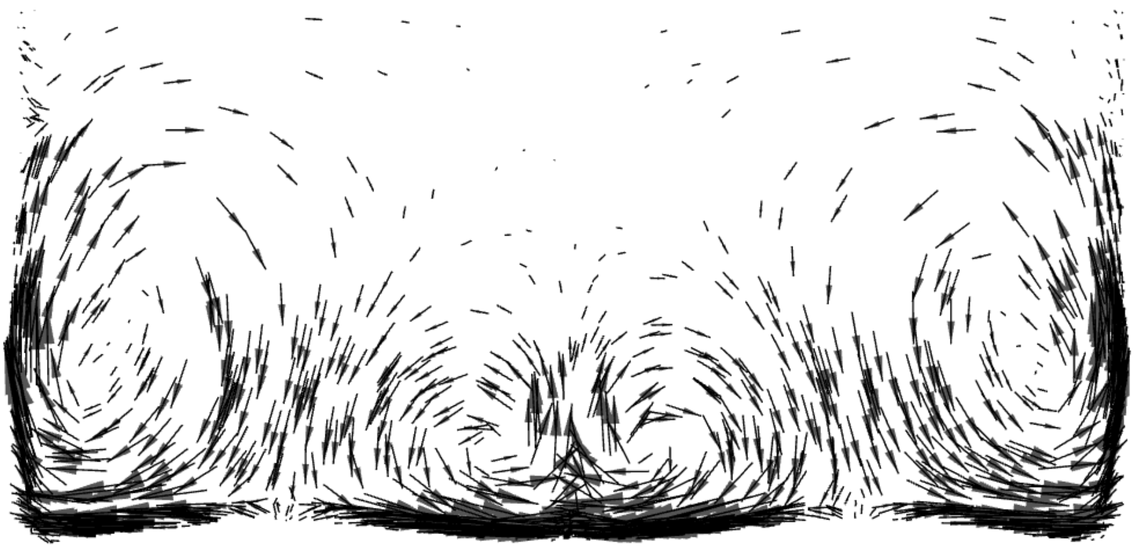

Figure 6.27: Helicity vectors in a plane perpendicular to the main flow in the middle of the interval between ribs 4-5, $y = 2.966m$, 32 iterations, $Re = 21500$

6.3.4 Heat transfer improvement relative to the baseline

In Figure 6.28, the Nusselt number ratio of the optimized domain is compared with that of the baseline domain at each axial coordinate.

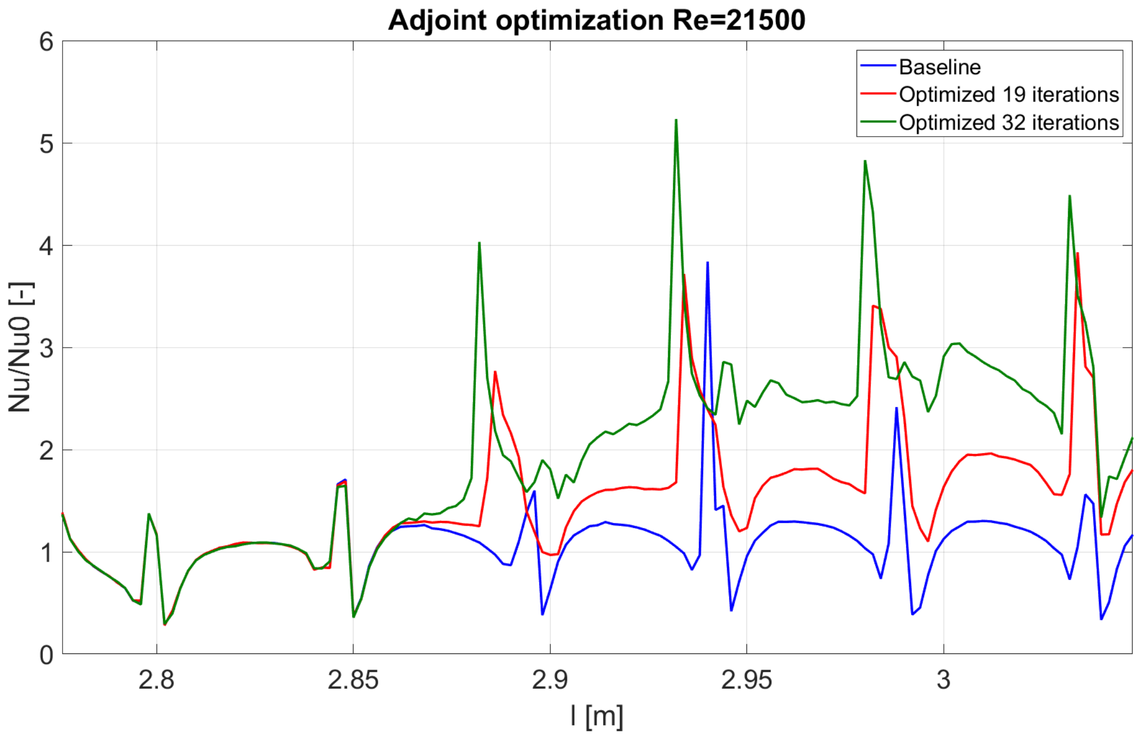

Figure 6.28: Nusselt number ratio of the optimized domain after 19 iterations, 32 iterations and the baseline domain, $Re = 21500$

It can be seen that after the first two ribs (not optimized) the Nusselt ratio is substantially equivalent for the three cases, but after the second rib from the beginning of the optimized region, the Nusselt ratio is greatly increased after the total 32 iterations compared to the baseline results. Then the averaged values are reported in Table 18.

	$Nu_{baseline}$ $[-]$	$Nu_{19}/Nu_{baseline}$ $[-]$	$Nu_{32}/Nu_{baseline}$ $[-]$
smooth sides	62.33	1.28	1.79
ribbed side	77.45	1.54	2.08
average	70.65	1.44	1.98

Table 18: Nu increment after the adjoint iterations relative to the baseline results, $Re = 21500$

The average values of Nu are about twice the baseline values. The friction factor also increases significantly, as shown in Table 19. In future analysis, it can be useful to impose an objective function that includes both the thermal performance and the friction factor to limit the increase in pressure loss.

$f_{baseline}[-]$	f_{19}/f_{bl} $[-]$	f_{32}/f_{bl} $[-]$
0.0194	2.39	4.81

Table 19: Friction factor increment after the adjoint iterations relative to the baseline results, $Re = 21500$

6.4 Results Re=21500, after final remeshing

The last aspect to verify the results after the optimization process is the error caused by the deformed mesh. Therefore, after the total 32 iterations, the final geometry is exported with an STL file. This file has been converted and cleaned with the help of Ansys SpaceClaim, then a new mesh is generated. This process is the same of the intermediate remeshing, but in this case only a flow solution has been carried, because this time the optimization has stopped due to solution convergence and not due to mesh quality criteria. Finally, the results of the optimized geometry before and after remeshing are compared in Figure 6.29 and Table 20.

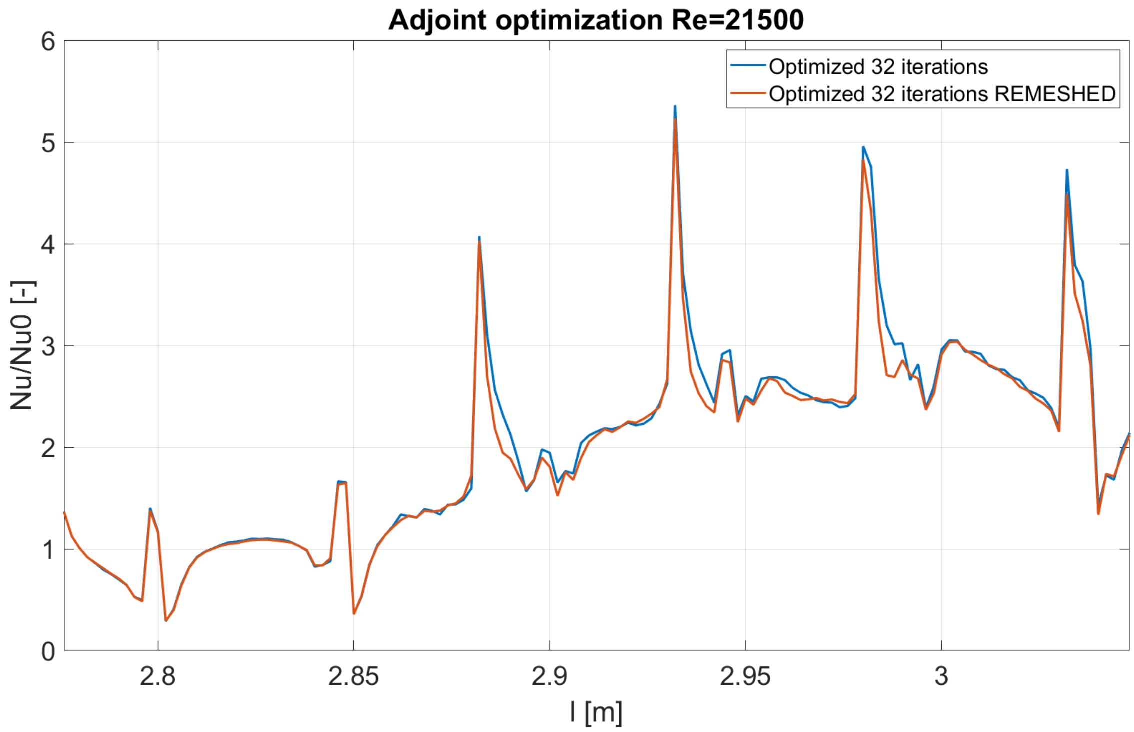

Figure 6.29: Comparison of Nu/Nu_0 along the optimization region before and after the remeshing, 32 iterations, $Re = 21500$

The results of heat exchange and friction factor are very close with a small percentage difference; therefore, the final results of the adjoint optimization are verified.

	Nu_{32iter} $[-]$	$Nu_{32iter-remeshed}$ $[-]$	$\Delta\%$
smooth side	111.55	111.63	-0.07%
ribbed side	166.46	161.11	3.32%
average	142.71	139.67	2.17%

Table 20: Nu results after 32 iterations before and after remeshing, $Re = 21500$

f_{32iter} $[-]$	$f_{32iter-remeshed}$ $[-]$	$\Delta\%$
0.0904	0.0912	-0.9%

Table 21: Friction factor results after 32 iterations before and after remeshing, $Re = 21500$

6.5 Results Re=42000, after 16 iterations

The HTC improvement at each iteration is shown in Figure 6.30.

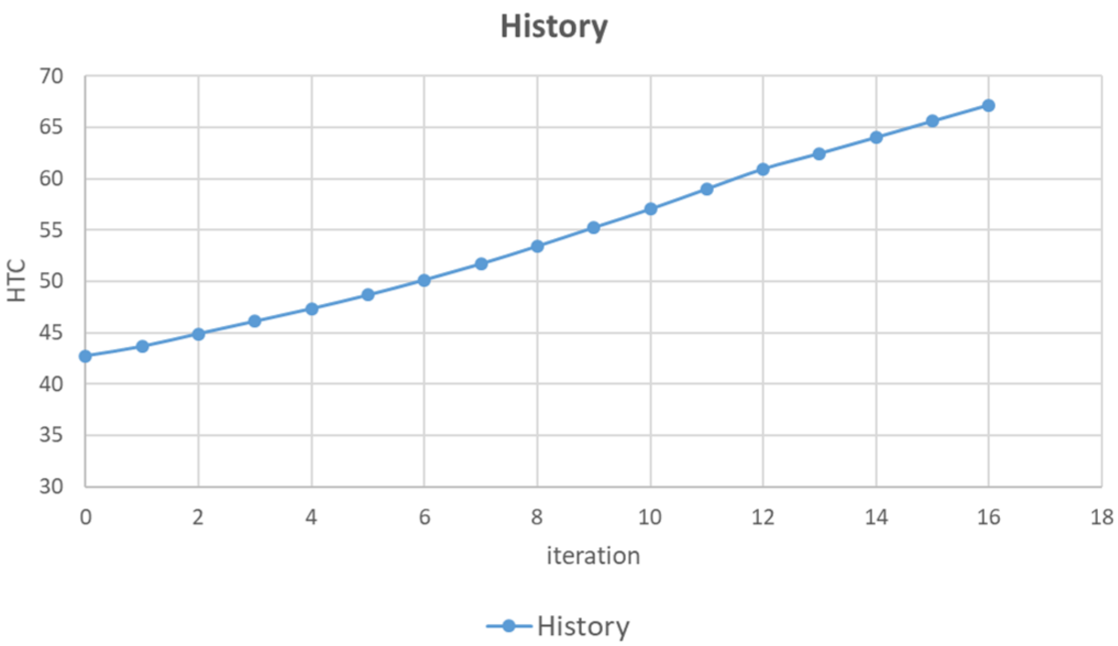

Figure 6.30: Adjoint optimization history after 16 iterations, $Re = 42000$

In Table 22, the total HTC increment is shown.

$HTC_{baseline}$ $[W/m^2K]$	$HTC_{16iterations}$ $[W/m^2K]$	$HTC_{16}/HTC_{baseline}$ $[-]$
42.7	67.2	1.57

Table 22: HTC increment after 16 iterations, $Re = 42000$

As in the precedent case, the optimization stopped before reaching the optimal solution due to poor mesh quality.

6.5.1 Optimized geometry after 16 iterations

In Figures 6.31, 6.32 and 6.33, the optimized geometry after 19 iterations is reported in top, lateral and isometric views, respectively.
The frontal view of the four ribs is shown in Figures 6.34, 6.35, 6.36 and 6.37; an isometric view of the four ribs is reported in Figure 6.38, to better visualize their similarities and differences.

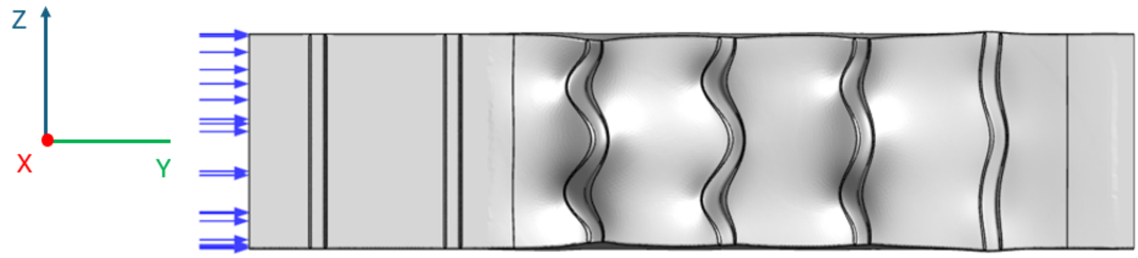

Figure 6.31: Optimized geometry after 16 iterations, $Re = 42000$, top view

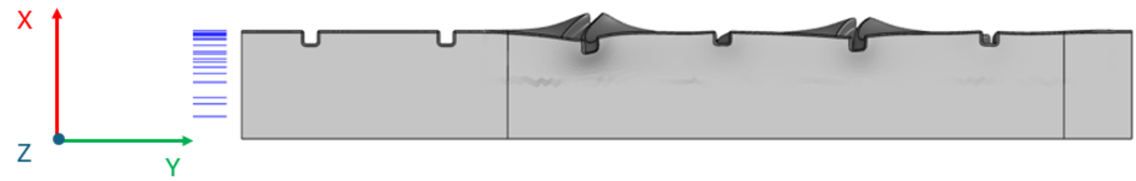

Figure 6.32: Optimized geometry after 16 iterations, $Re = 42000$, lateral view

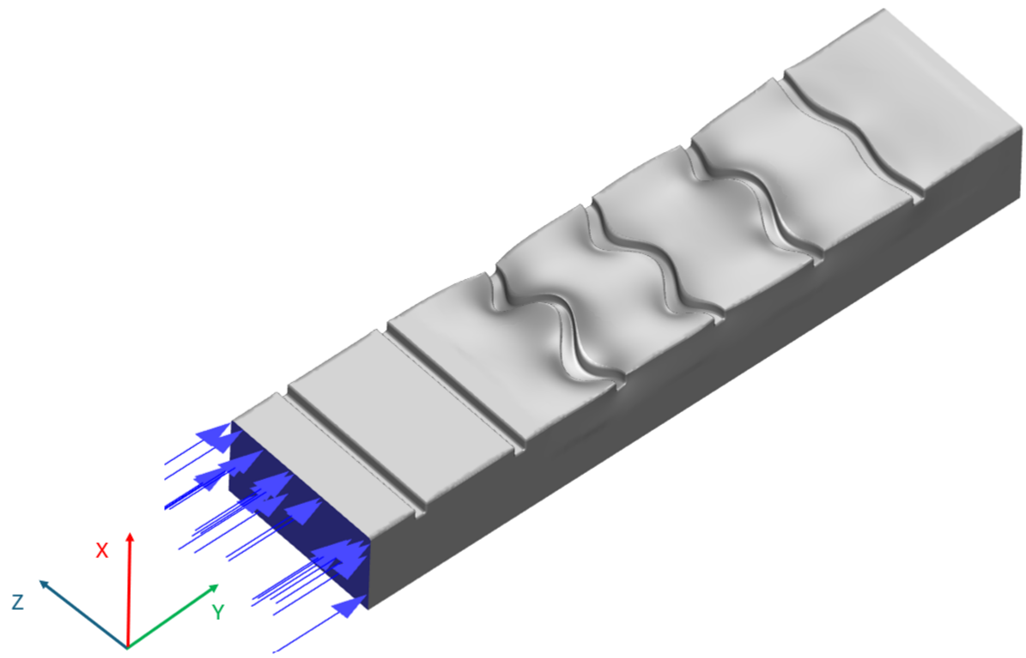

Figure 6.33: Optimized geometry after 16 iterations, $Re = 42000$, isometric view

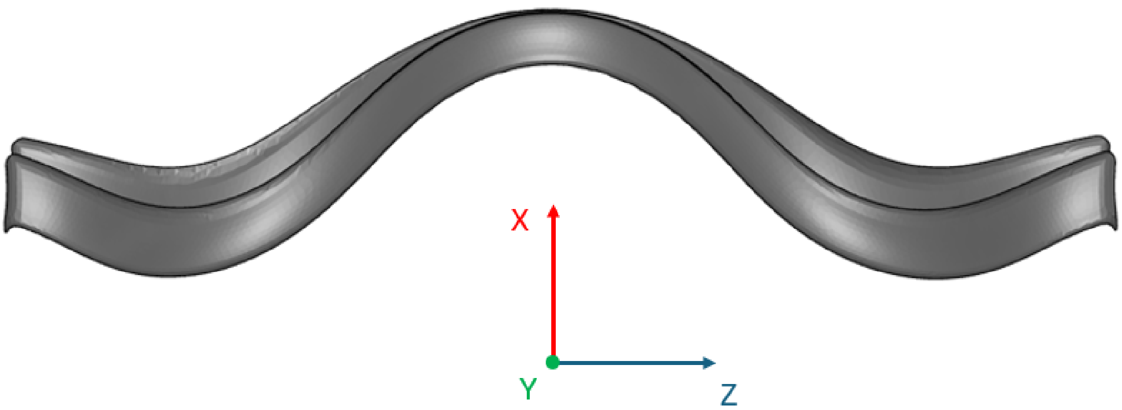

Figure 6.34: Optimized rib 1 after 16 iterations, $Re = 42000$, frontal view

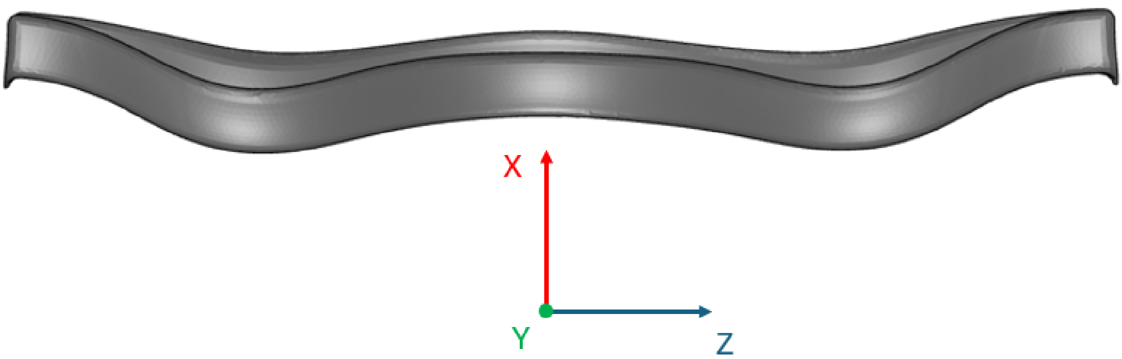

Figure 6.35: Optimized rib 2 after 16 iterations, $Re = 42000$, frontal view

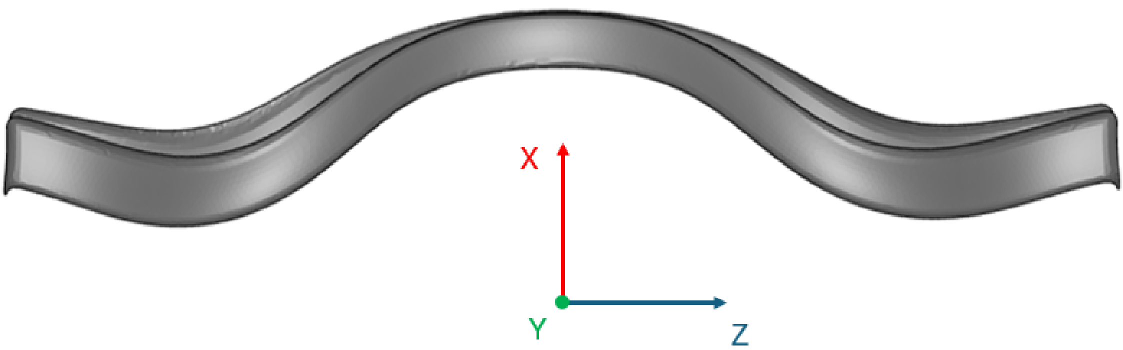

Figure 6.36: Optimized rib 3 after 16 iterations, $Re = 42000$, frontal view

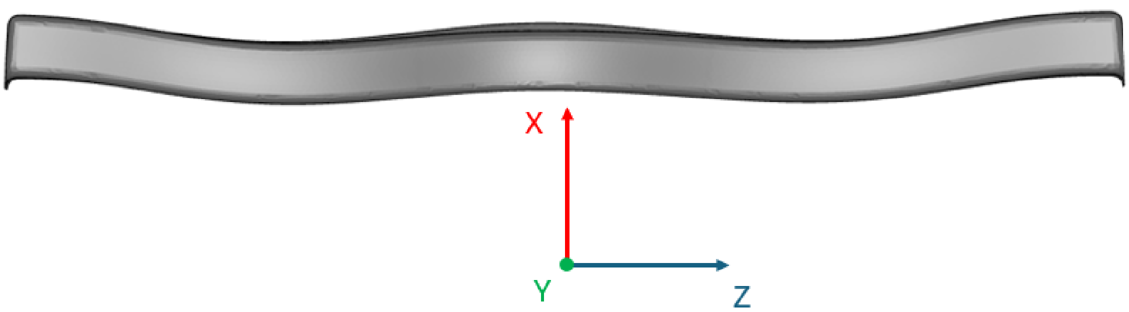

Figure 6.37: Optimized rib 4 after 16 iterations, $Re = 42000$, frontal view

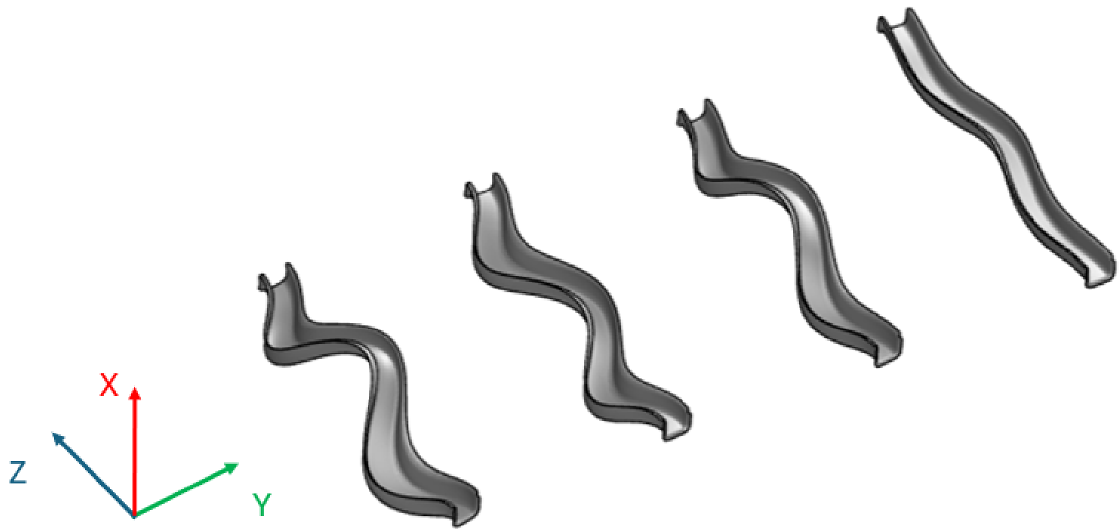

Figure 6.38: Optimized ribs after 16 iterations, $Re = 42000$, isometric view

The same shape characteristics of the $Re = 21500$ are observed in the $Re = 42000$ case. The first rib is the most deformed, because it impacts all the successive ones and the flow structure. The first and third ribs are wavier than the second and fourth ones. The central valley and the two lateral peaks of the ribs are wider compared to the $Re = 21500$ case, this was predictable for the larger flow turbulence and its consequent instability. The main features described for the previous case are visible: periodicity between ribs 1-3 and 2-4, w-shaped ribs and w-shaped channel cross section.

6.5.2 Vorticity effects on heat transfer

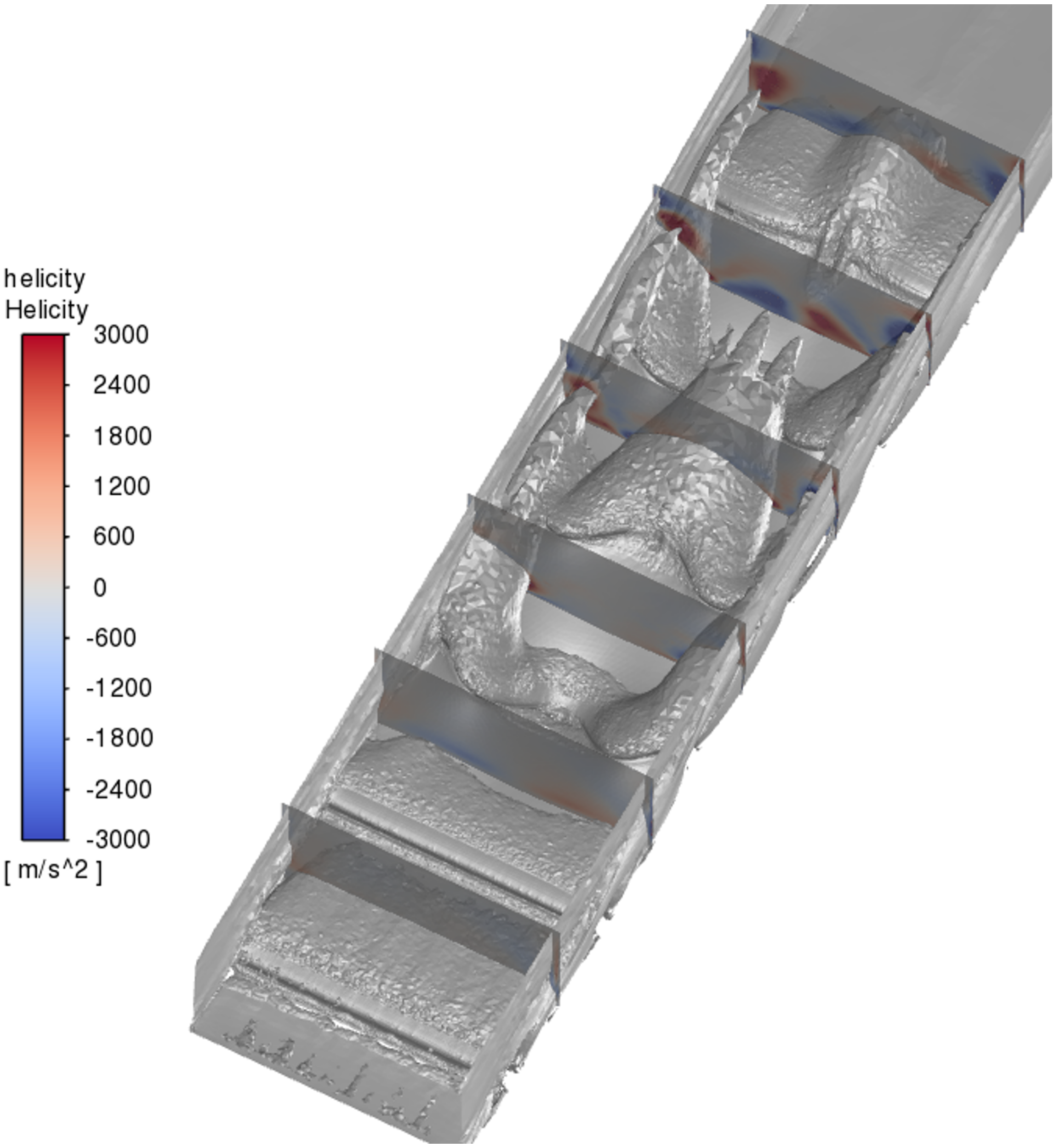

Figure 6.39: Vorticity induced by optimized ribs, 16 iterations, $Re = 42000$

The same eddies structure of the $Re = 21500$ case is observed in the $Re = 42000$ case, but this time the heat exchange is higher and the eddies are faster and more irregular. Figure 6.39 shows the eddies structure generated after the optimized ribs. In Figure 6.40, the portions where the heat exchange has maximum values are even larger in area compared to the $Re = 21500$ case, particularly the red regions achieve great heat transfer improvements. In Figures 6.41 and 6.42, the eddies in the middle of the optimized rib pitches are shown.
The impingement of the coolant is present on the smooth walls after the optimized ribs, as in the $Re = 21500$ case. It can be seen in Figure 6.41 where the heat flux is increased.

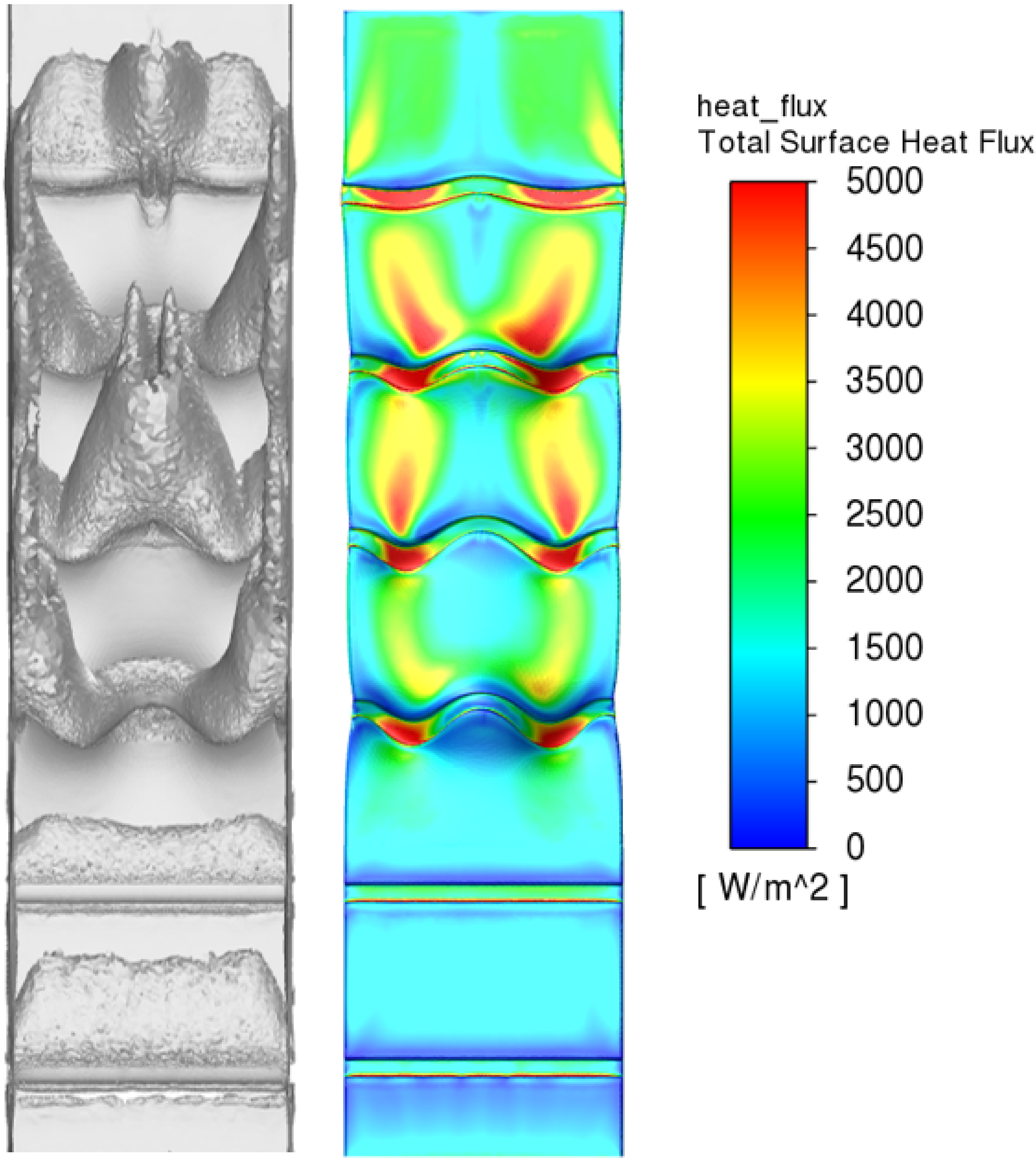

Figure 6.40: Vorticity and heat transfer enhancement induced by optimized ribs, 16 iterations, $Re = 42000$, top view

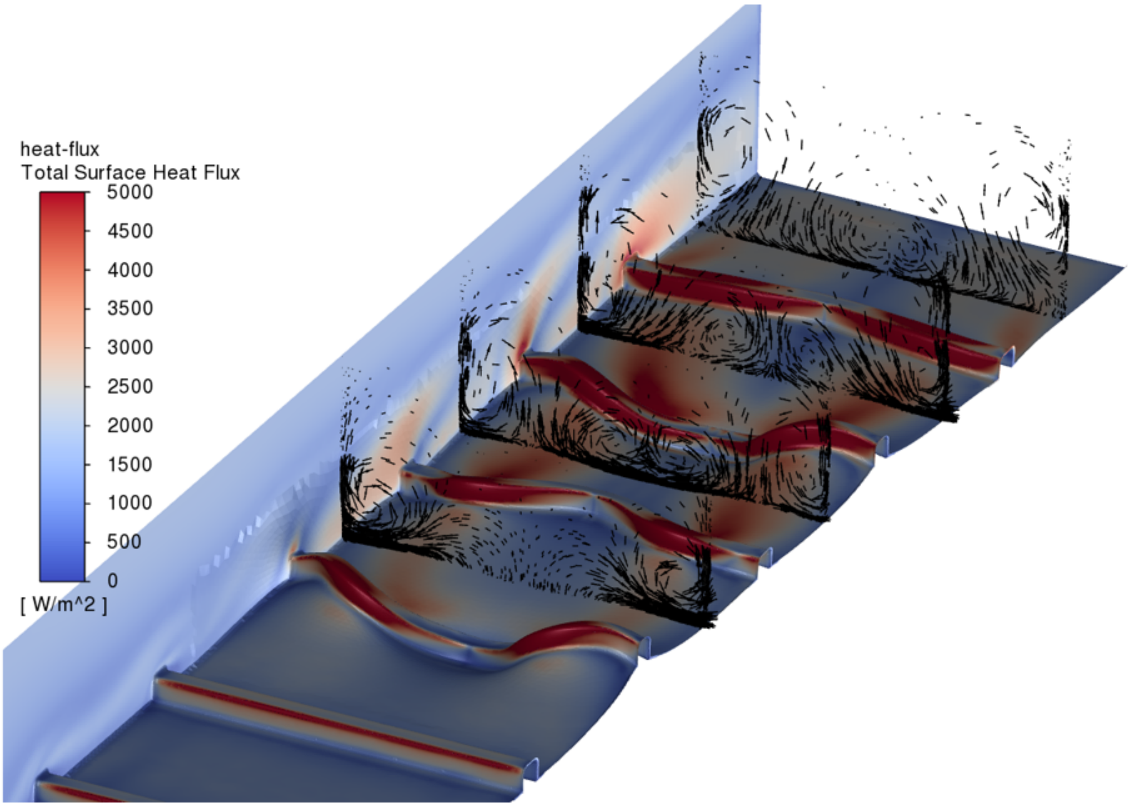

Figure 6.41: Heat transfer enhancement and eddies induced by optimized ribs, 16 iterations, $Re = 42000$

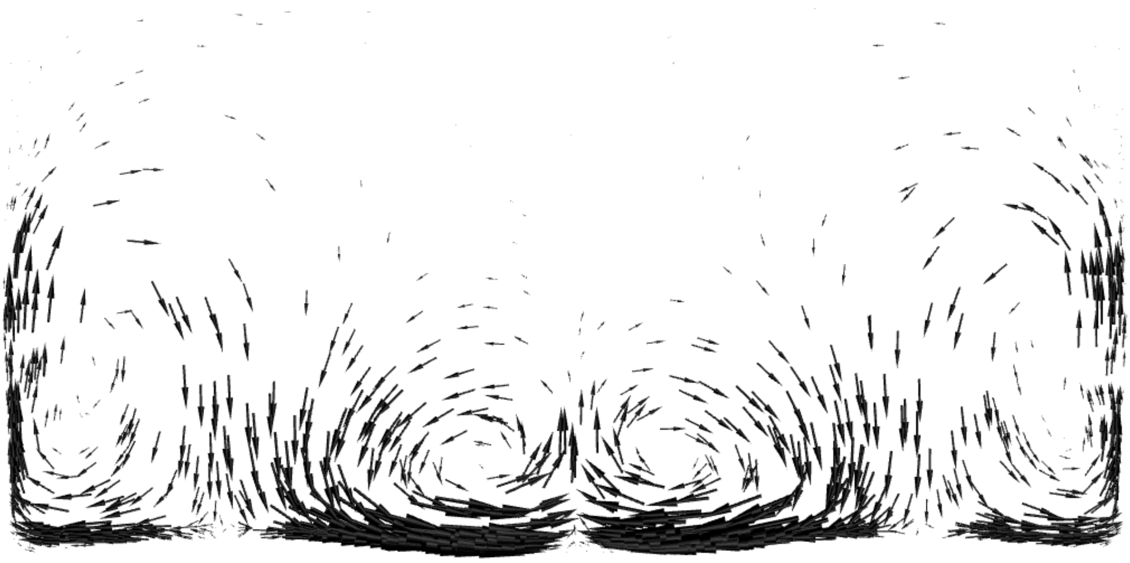

Figure 6.42: Helicity vectors in a plane perpendicular to the main flow in the middle of the interval between ribs 4-5, $y = 2.966m$, 16 iterations, $Re = 42000$

6.6 Remeshing, Re=42000, after 16 iterations

The adjoint optimization stopped after 16 iterations, as stated in the previous paragraph, not because the solver had reached an optimal solution, but because of poor mesh quality. In fact, the solution after 16 iterations has not reached convergence, but the mesh has been excessively deformed and it does not respect anymore the minimum orthogonality of 0.005 imposed before launching the optimization. Especially near the most modified ribs, the mesh elements are more irregular and perturbed compared to the baseline mesh.

Therefore, in order to proceed with further iterations and obtain better thermal performance results, the same remeshing process described for the Re = 21500 case is applied for the Re = 42000 case. The slight difference in geometry before remeshing can be seen near ribs, the surface is slightly deformed by the process of merging the STL file tetrahedrons. In Figure 6.43, the mesh before remeshing is compared to the mesh after remeshing. The elements near the ribs are now more regular, instead of the deformed mesh where some cells are almost degenerate tetrahedrons.

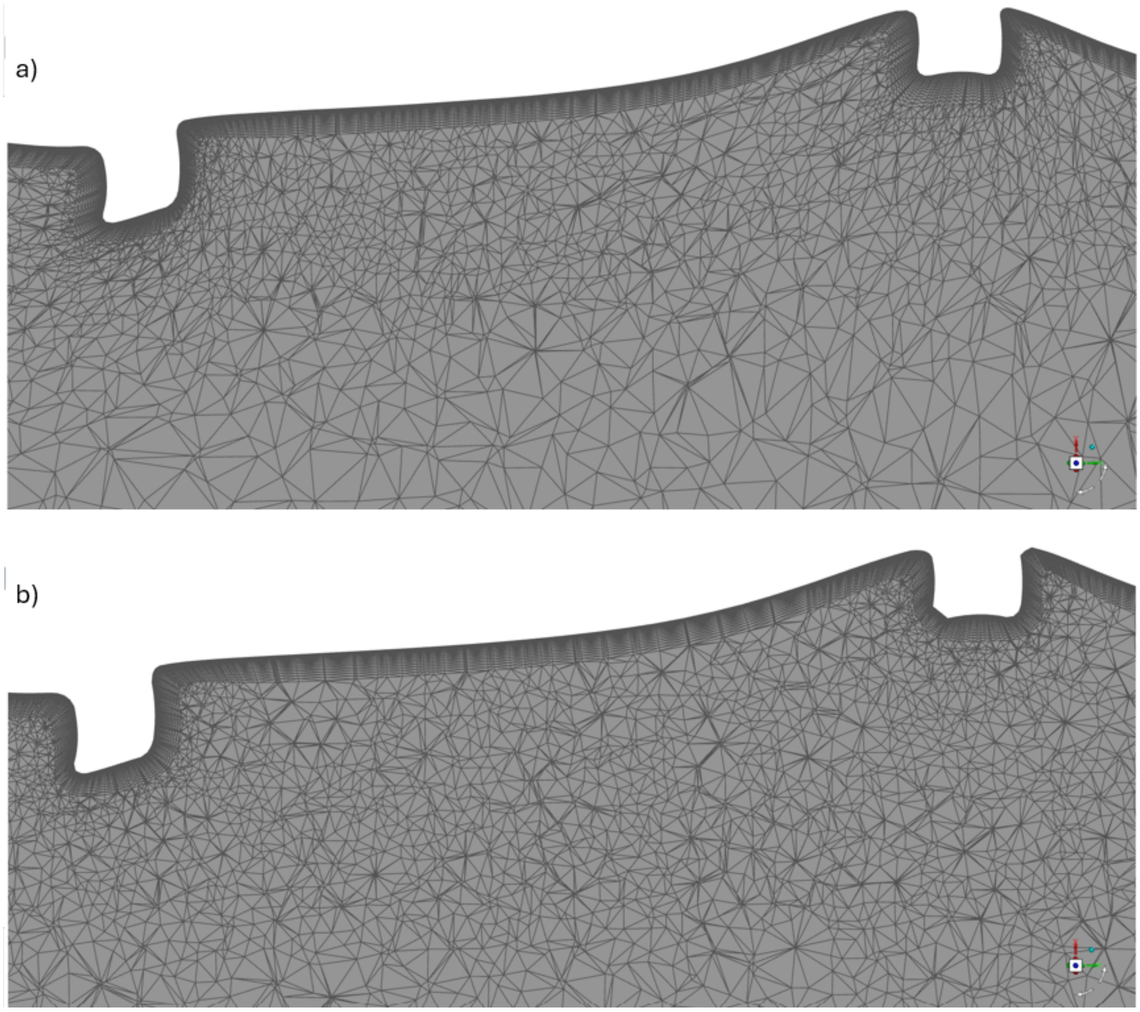

Figure 6.43: Mesh deformed before and after remeshing, Re = 42000, view of mesh near second and third optimized ribs in longitudinal XY plane (ribs plane of symmetry)

6.7 Results Re=42000, after 44 iterations

The HTC improvement at each iteration is shown in Figure 6.44:

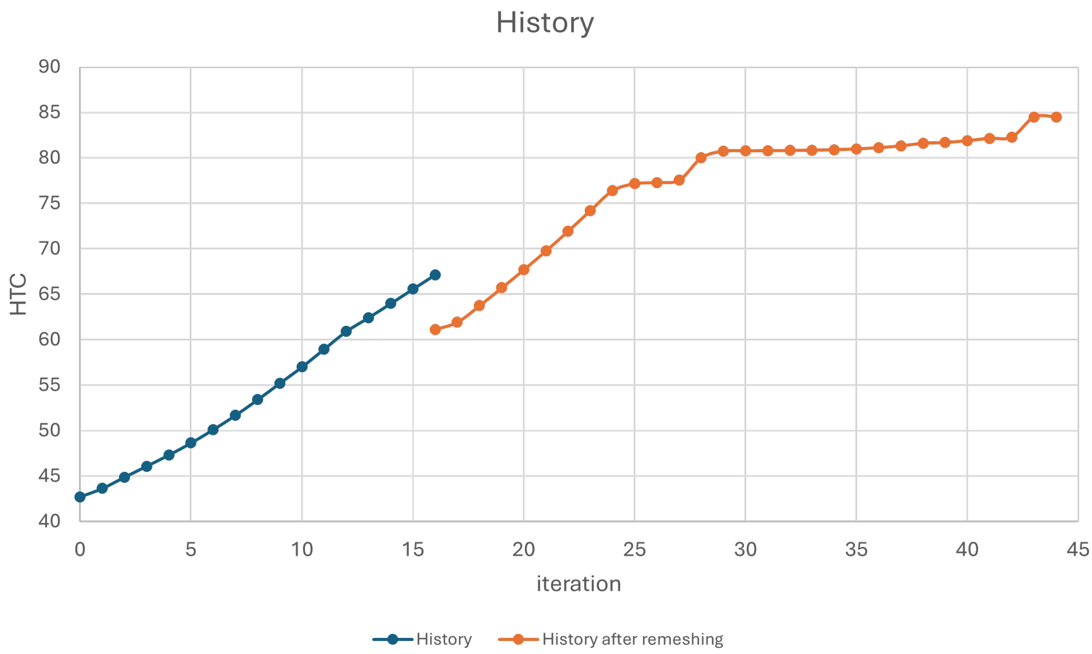

Figure 6.44: Adjoint optimization history after 44 iterations, $Re = 42000$

In Table 23, the total HTC increment is shown:

$HTC_{baseline}$ $[W/m^2K]$	$HTC_{16remeshed}$ $[W/m^2K]$	HTC_{44} $[W/m^2K]$	$HTC_{44}/HTC_{baseline}$
42.7	61.2	84.5	1.98

Table 23: HTC increment after the total 44 iterations, $Re = 42000$

As in the $Re = 21500$ case, the average HTC of the optimized region after remeshing is slightly different from the average HTC after 16 iterations. The causes are the same of the previous case.

6.7.1 Optimized geometry after 44 iterations

In Figures 6.45, 6.46 and 6.47, the optimized geometry after 19 iterations is reported in top, lateral and isometric views, respectively.
The frontal view of the four ribs is shown in Figures 6.48, 6.49, 6.50 and 6.51; an isometric view of the four ribs is reported in Figure 6.52, to better visualize their similarities and differences.
The ribs pattern is the same of the previous results, but the shape is much more deformed. The distance between the central valley and the lateral peaks is remarkable, especially in the first rib, but also in the third rib. The deformation also involves the ribbed wall surface, it can be seen in the lateral view of the optimized geometry, where the ribbed wall surface has a considerable height in proximity of the first and third ribs.

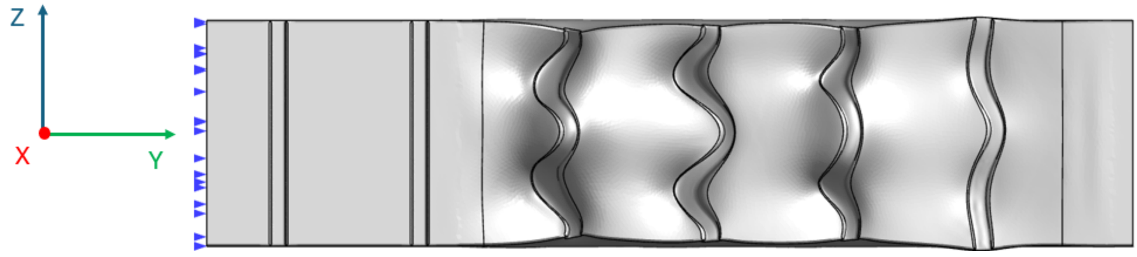

Figure 6.45: Optimized geometry after 44 iterations, $Re = 42000$, top view

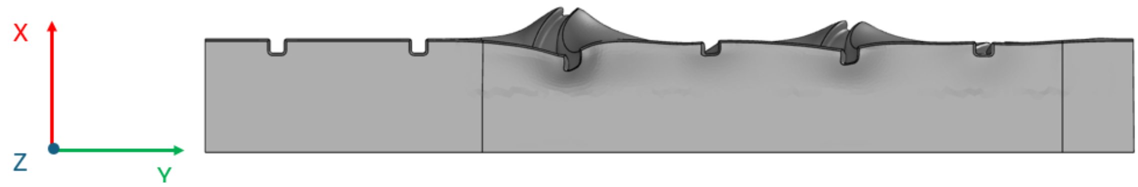

Figure 6.46: Optimized geometry after 44 iterations, $Re = 42000$, lateral view

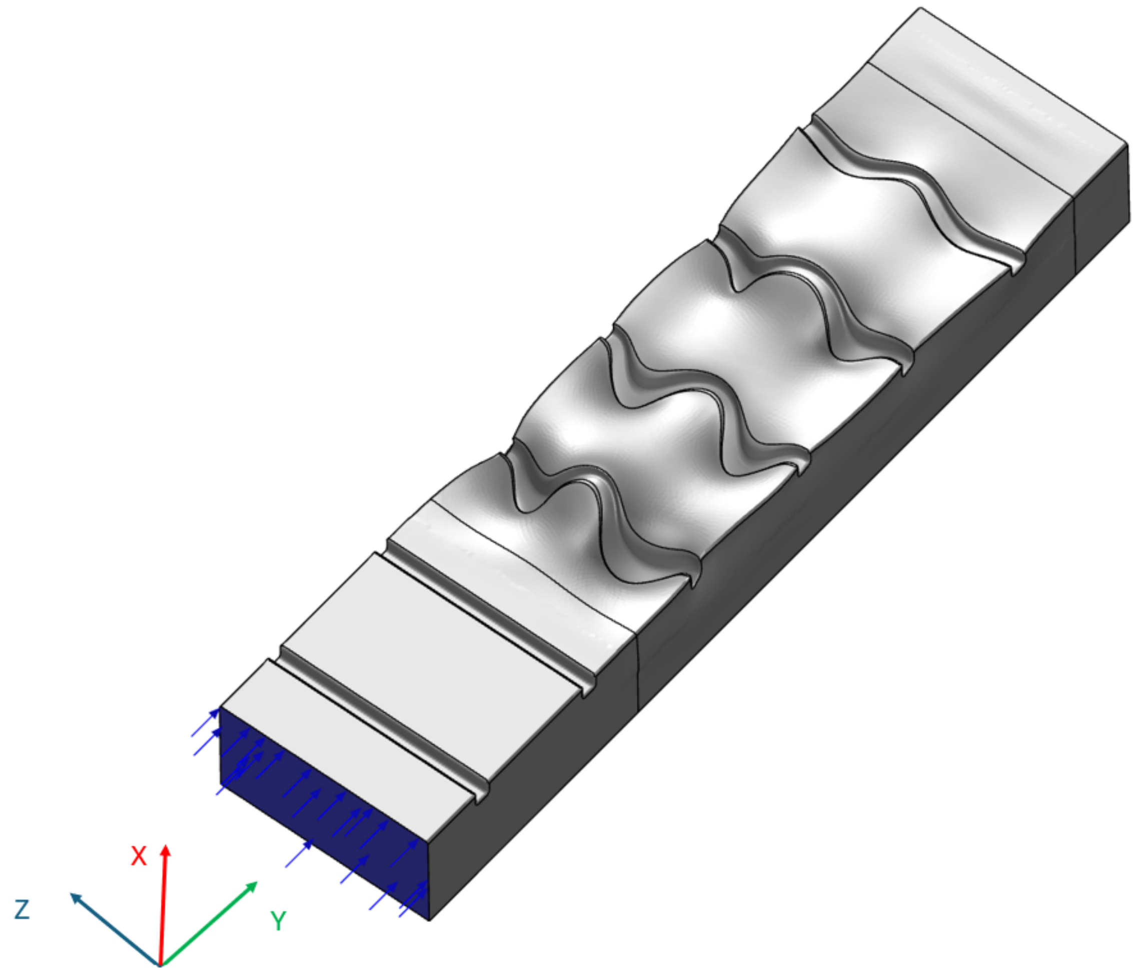

Figure 6.47: Optimized geometry after 44 iterations, $Re = 42000$, isometric view

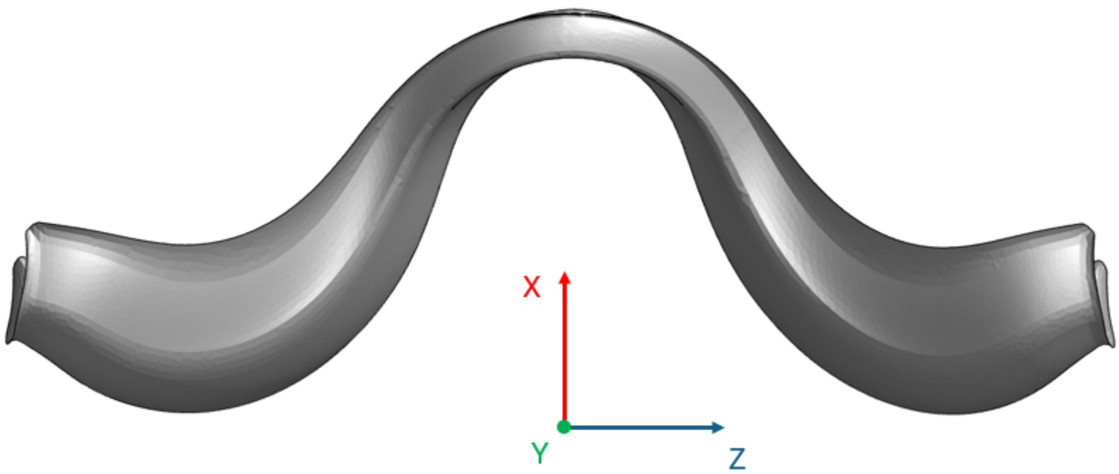

Figure 6.48: Optimized rib 1 after 44 iterations, $Re = 42000$, frontal view

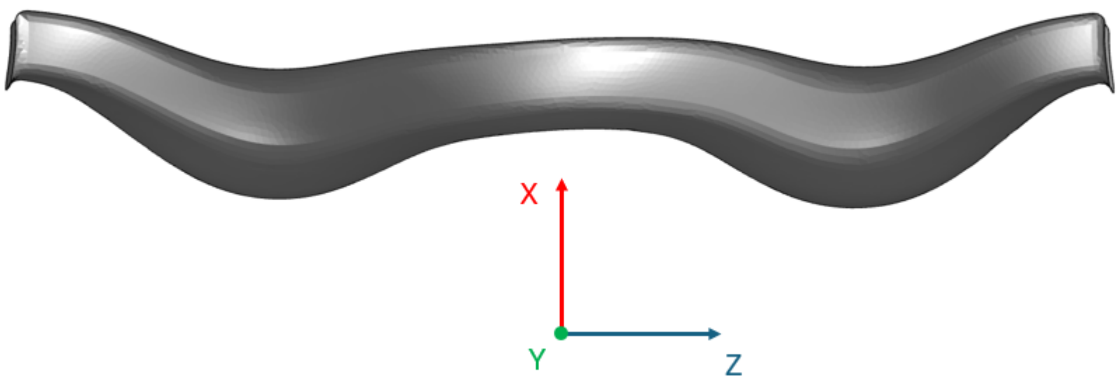

Figure 6.49: Optimized rib 2 after 44 iterations, $Re = 42000$, frontal view

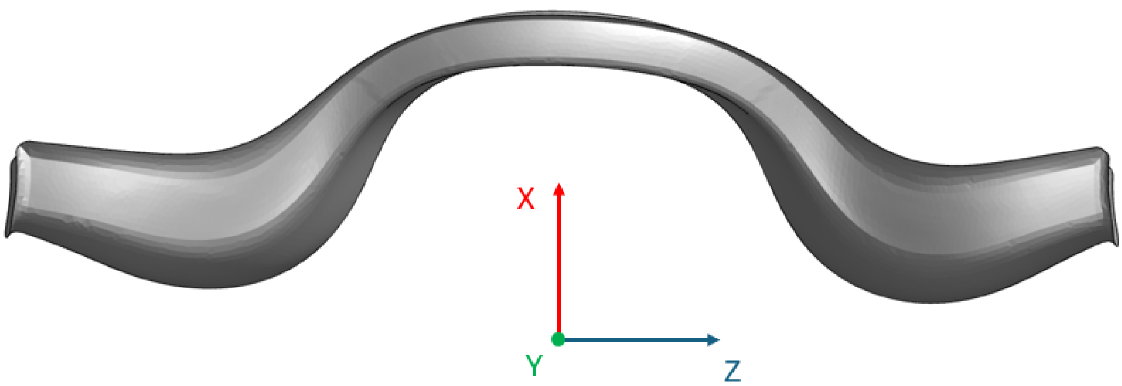

Figure 6.50: Optimized rib 3 after 44 iterations, $Re = 42000$, frontal view

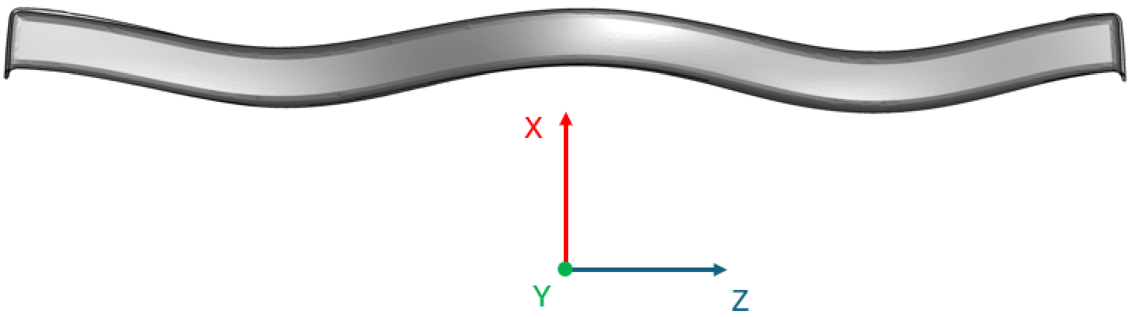

Figure 6.51: Optimized rib 4 after 44 iterations, $Re = 42000$, frontal view

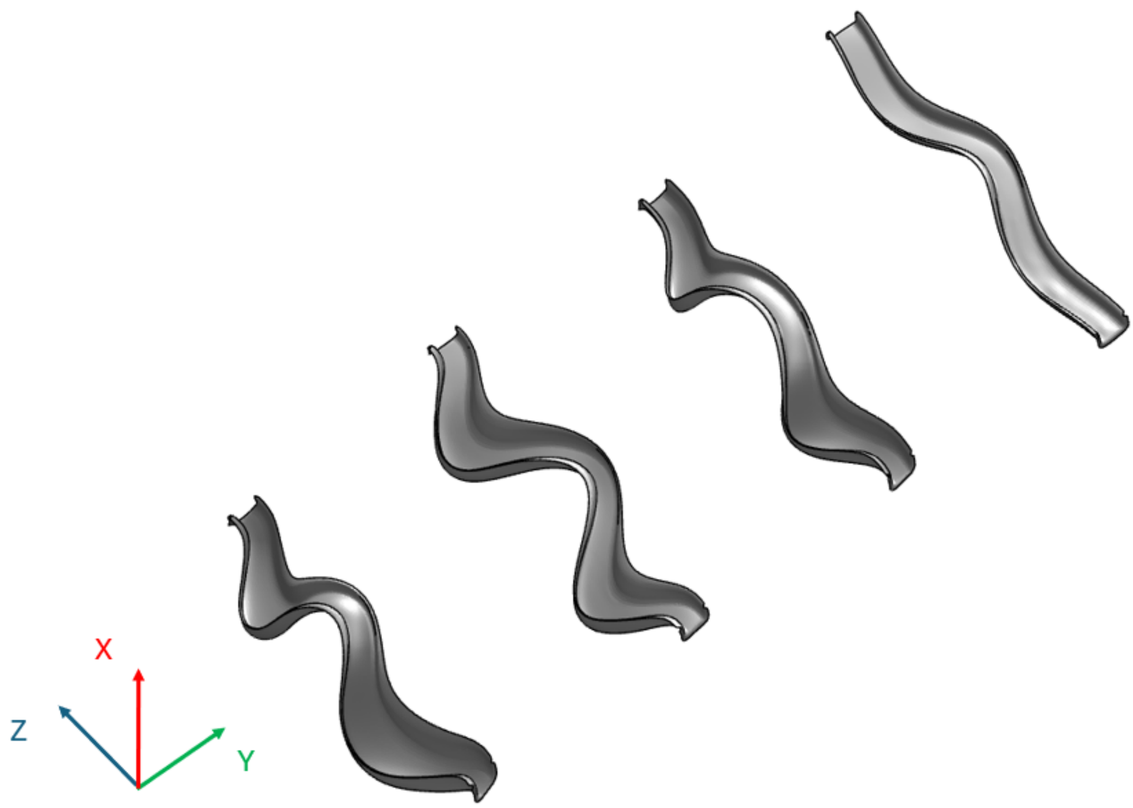

Figure 6.52: Optimized ribs after 44 iterations, $Re = 42000$, isometric view

6.7.2 Vorticity effects on heat transfer

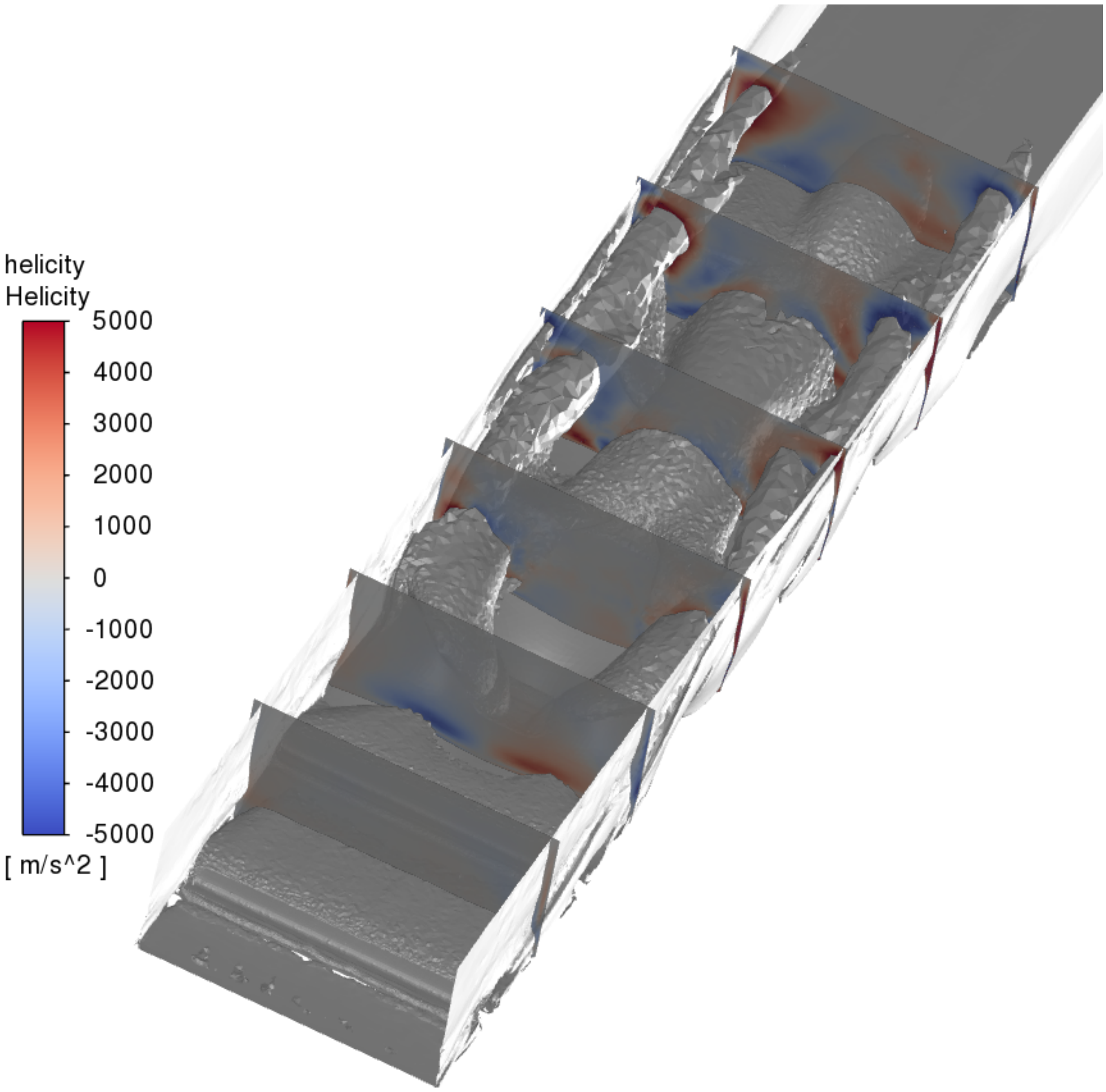

Figure 6.53: Vorticity induced by optimized ribs, 44 iterations, $Re = 42000$

In Figure 6.53, it can be seen that the helicity is much higher than in the $Re = 21500$ case and in the $Re = 42000$ case after 16 iterations. This results in a very high heat exchange, in particular in the ribbed wall. The heat flux contour, shown in Figure 6.54, has large regions where the heat flux is maximized (in red), much wider compared to the previous 16 iterations. In Figures 6.55 and 6.56, the counter rotating eddies are shown, this phenomenon is equivalent to the previous case, but in this case is more amplified by the more perturbed ribs. The thermal performance is considerably higher than in the $Re = 42000$ geometry after 16 iterations, this can be seen in the heat flux contour where in the ribbed wall between the optimized rib the red zones of maximum heat exchange are much more extended than in previous cases.
In addition, the impingement on the smooth walls is much higher than after the first 16 iterations. In Figure 6.55, it can be seen that the regions of maximum heat flux on the smooth wall are much wider than after the first iterations.

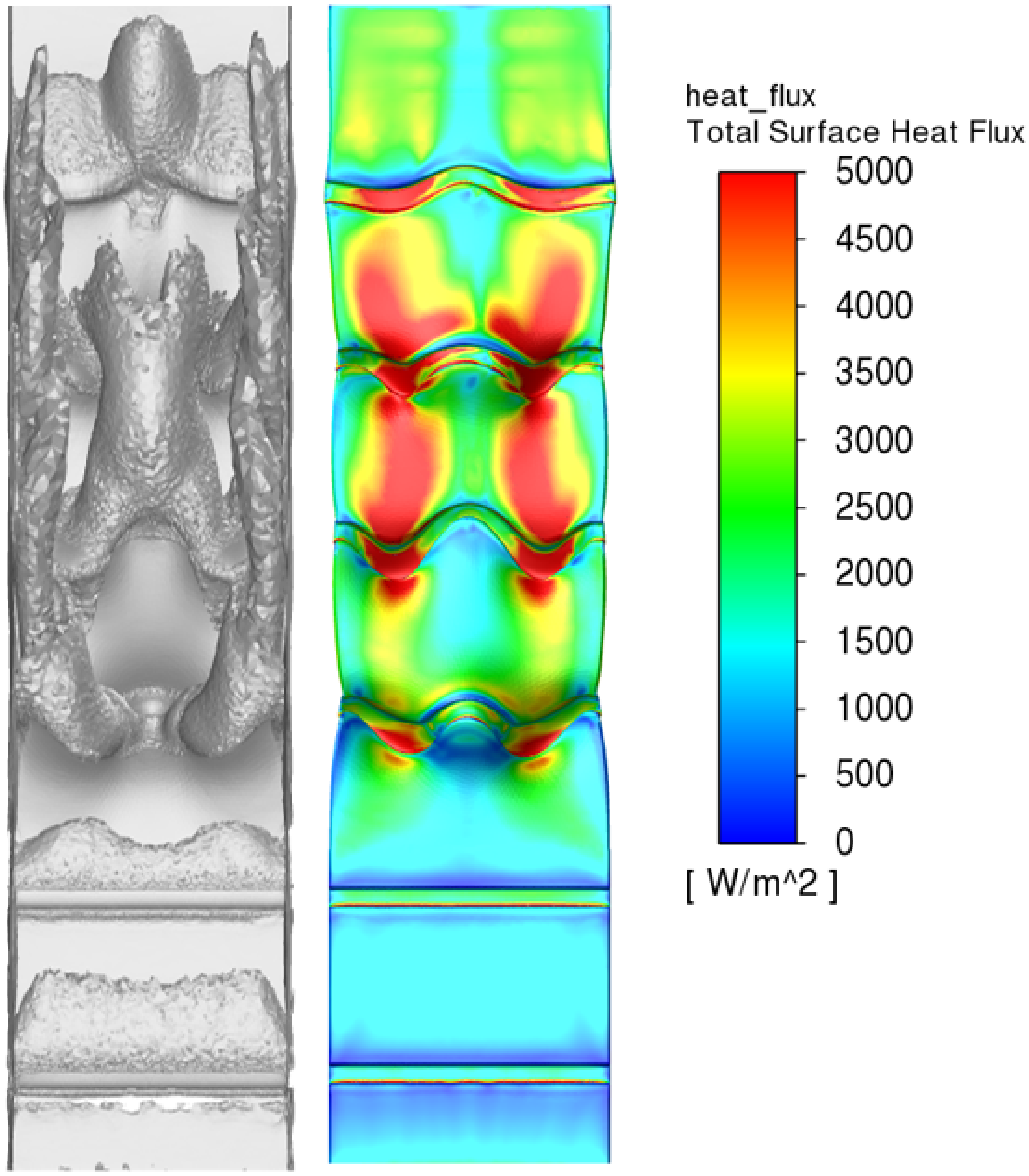

Figure 6.54: Vorticity and heat transfer enhancement induced by optimized ribs, 44 iterations, $Re = 42000$

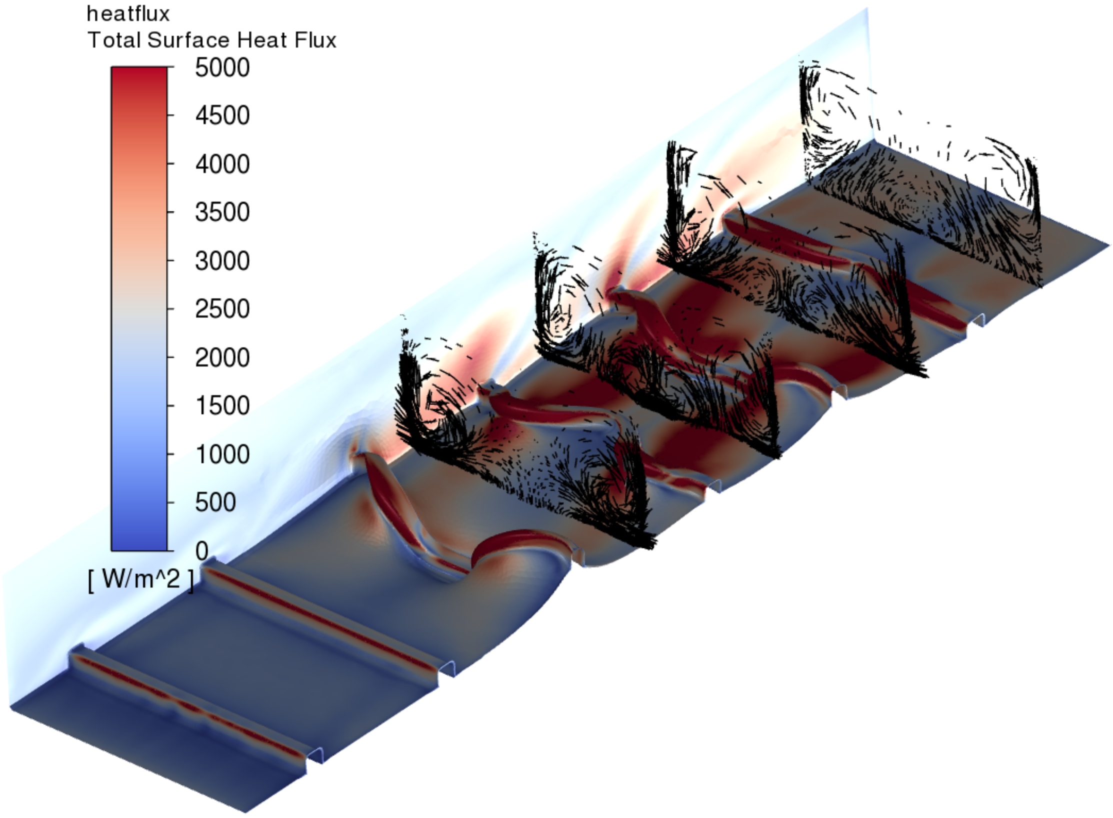

Figure 6.55: Heat transfer enhancement and eddies induced by optimized ribs, 44 iterations, $Re = 42000$

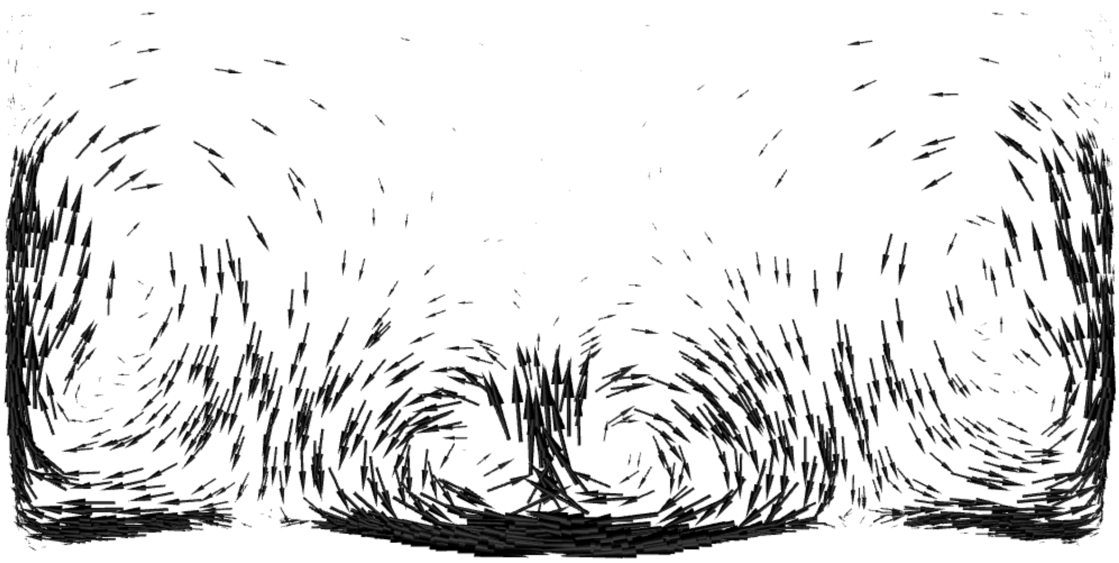

Figure 6.56: Helicity vectors in a plane perpendicular to the main flow in the middle of the interval between ribs 4-5, $y = 2.966m$, 44 iterations, $Re = 42000$

6.7.3 Heat transfer improvement relative to the baseline

In Figure 6.57, the Nusselt number ratio of the optimized domain is compared with that of the baseline domain at each axial coordinate.

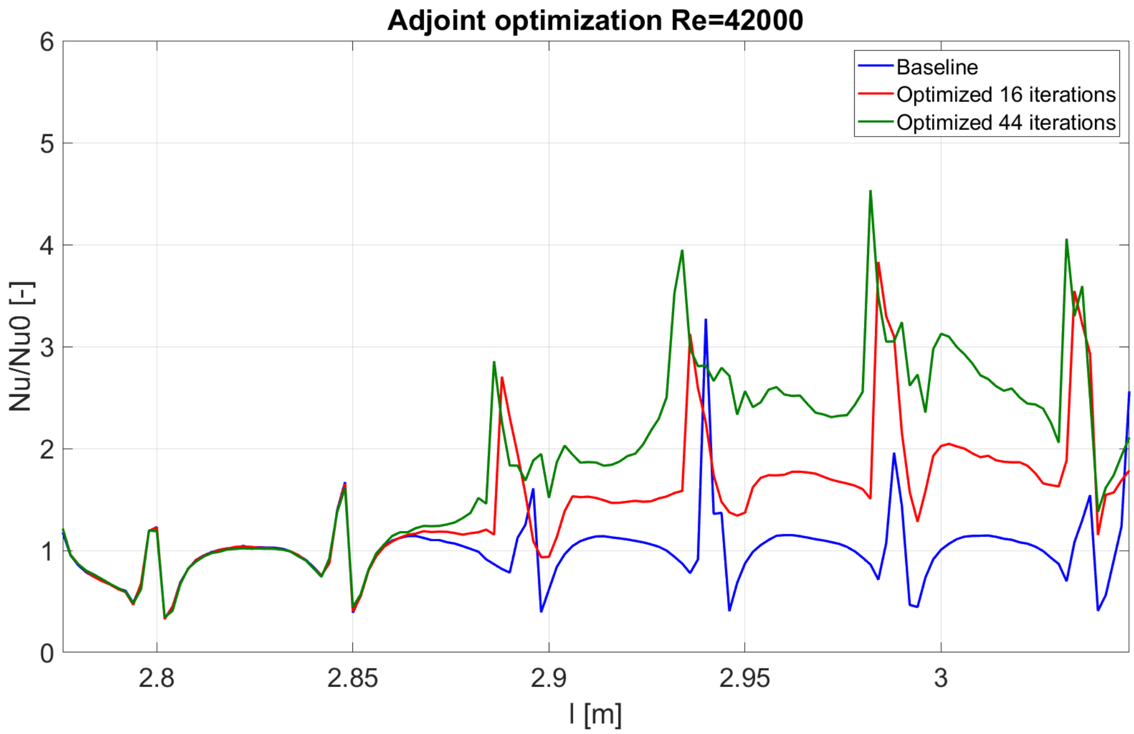

Figure 6.57: Nusselt number ratio of the optimized domain after 16 iterations, after 44 iterations and the baseline domain, $Re = 42000$

The Nusselt ratio improvement is very similar to that occurred under $Re = 21500$, both in each axial coordinate and in the average values, which are reported in the table. In Table 24, it can be seen that, after the total 44 iterations, the average Nu is more than twice the value of the baseline. Meanwhile, the friction factor increases more than the heat exchange (Table 25). Under this more turbulent flow of $Re = 42000$, this enhancement is more pronounced. Future optimizations could be performed to limit the pressure loss, together with the increase in heat transfer.

	$Nu_{baseline}$ $[-]$	$Nu_{16}/Nu_{baseline}$ $[-]$	$Nu_{44}/Nu_{baseline}[-]$
smooth sides	102.09	1.36	1.89
ribbed side	118.24	1.70	2.22
average	111.10	1.56	2.09

Table 24: Nu increment after the adjoint iterations relative to the baseline results, $Re = 42000$

$f_{baseline}[-]$	f_{16}/f_{bl} $[-]$	f_{44}/f_{bl} $[-]$
0.0162	2.88	5.79

Table 25: Friction factor increment after the adjoint iterations relative to the baseline results, $Re = 42000$

6.8 Results Re=42000, after final remeshing

The last aspect to verify the results after the optimization process is the error caused by the deformed mesh. In Figure 6.58, the results of the optimized geometry before and after remeshing are compared, as in the $Re = 21500$ channel.

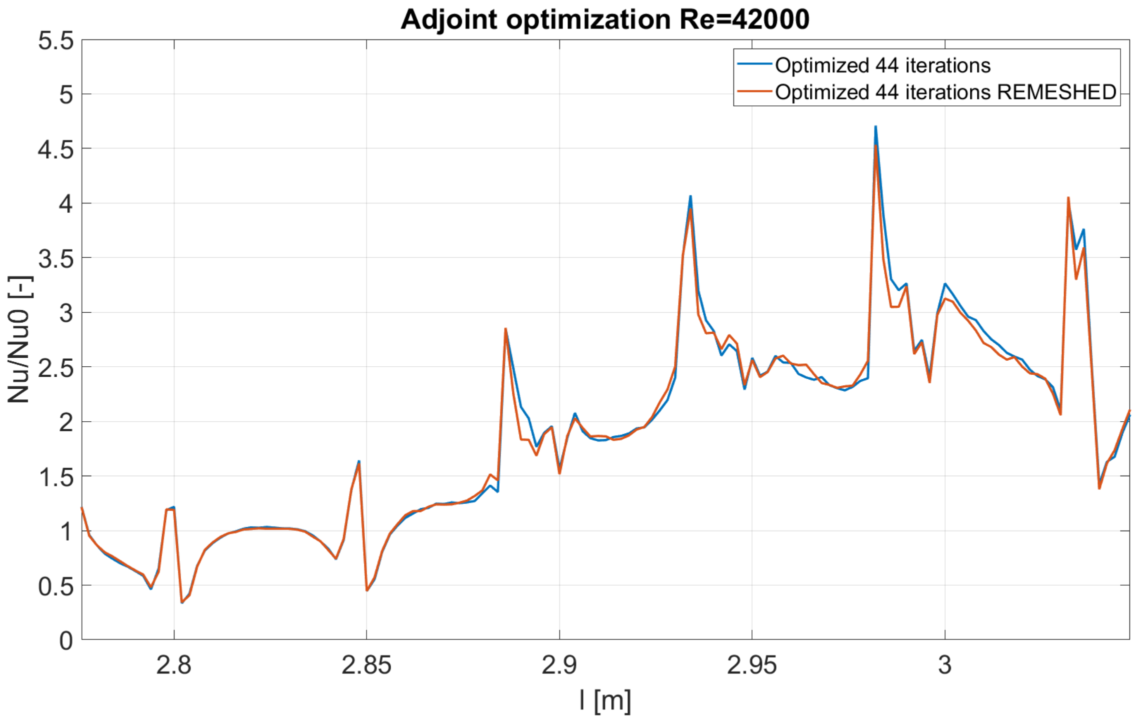

Figure 6.58: Comparison of Nu/Nu_0 along the optimization region before and after the remeshing, 44 iterations, $Re = 42000$

As shown in the Figure 6.58 and in Tables 26 and 27, the results of heat exchange and friction factor are very close with a small percentage difference; therefore, the final results of the adjoint optimization are verified.

	Nu_{44iter} $[-]$	$Nu_{44iter-remeshed}$ $[-]$	$\Delta\%$
smooth side	192.1	193.1	-0.49%
ribbed side	267.24	262.45	1.82%
average	234.96	232.62	1.01%

Table 26: Nu results after 44 iterations before and after remeshing, $Re = 42000$

f_{44iter} $[-]$	$f_{44iter-remeshed}$ $[-]$	$\Delta\%$
0.0901	0.094	-4.1%

Table 27: Friction factor results after 44 iterations before and after remeshing, $Re = 42000$

7 Conclusions

In this activity, the first part is focused on the realization of a CFD model of a rib roughened internal cooling channel, on the basis of a real channel studied by Han et al. [3-4]. Different turbulence models have been compared to verify the consistency of the model results with experimental correlations. The choice fell on the Reynolds Stress Model, which gives heat transfer and friction factor results similar to the experimental correlations. Then, the mesh independence has been studied, having defined three different meshes (fine, medium and coarse resolutions). The medium mesh has been accepted as a good compromise between accuracy and simulation time.
The main objective of this activity is to optimize the internal channel using the adjoint optimization method, described in the second part of this work. The selected domain is the last trait of the entire channel, which comprises the last six ribs of the heated region. Using this reduced domain, it has been chosen to optimize the heat transfer coefficient HTC in the region that contains the last four ribs under two flow conditions, at $Re = 21500$ and $Re = 42000$. The resulting geometry presents similar features under the two Re: w-shaped ribs; w-shaped channel cross section; periodicity between ribs 1-3 and 2-4 where the first couple has a wavier profile, while the second pair has a less perturbed shape. These particular features generate counter rotating eddies that promote heat transfer by pushing the coolant into contact with the walls. Under $Re = 42000$, the geometry has a more curved profile, due to the higher turbulence of the flow. Under both flow conditions, the first rib is very noticeable for the larger central valley and adjacent peaks.
The final geometry results have proven that adjoint optimization is a very powerful tool to obtain complex shapes and a precise path of enhancing the objective functions. In fact, after defining one or more objective functions, in this case the heat transfer coefficient HTC, the process is almost automated. The only disadvantage is that the mesh is deformed after each iteration, which requires a remeshing process after some iterations to proceed with further optimization.

7.1 Future studies

This work represents only a starting point for future improvements. In fact, several configurations and parameters of the ribs can be studied to improve thermal performance and reduce pressure losses. For example, a more complex adjoint optimization setup could be conceived to also include pressure loss reduction as an objective function and to allow more geometric changes. In this activity, the optimization process is quite simple and with few variables, but way more complex geometries and flow conditions can be treated. The final optimized geometry obtained in this work is not necessarily the absolute maximum, but is more probably a relative maximum depending on the imposed setup and solver settings, and the relative improvement percentage imposed for each iteration. With successive studies, a more comprehensive analysis could be performed to better underline the physics of the eddies structure and how the geometry parameters influence it.
More generally, adjoint optimization could be applied for designing several machines, from aircraft to wind turbines, both with built-in software and open-source frameworks, as in the work of He et al. [6].

References

[1] Bunker R., Dees J.E., Palafox P. (2014), *Impingement Cooling In Gas Turbines:Design, Applications, And Limitations*

[2] Han J.C., Dutta S., and Ekkad S.V. (2012), *Gas Turbine Heat Transfer and Cooling Technology* Taylor and Francis Group

[3] Han J.C. (1984), *Heat Transfer and Friction in Channels With Two Opposite Rib-Roughened Walls*. Mechanical Engineering Department, Texas A&M University, College Station, Texas

[4] Han J.C., Park J.S., Lei C.K. (1985), *Heat Transfer Enhancement in Channels With Turbulence Promoters*. Turbomachinery Laboratories, Mechanical Engineering Department, Texas A&M University, College Station, Texas

[5] Han J.C., Ekkad S.V. (2001), *Recent Development in Turbine Blade Film Cooling*. Turbine Heat Transfer Laboratory, Mechanical Engineering Department, Texas A&M University, College Station, TX 77843-3123, USA

[6] He Ping, Mader Charles A., Martins Joaquim R. R. A., and Maki Kevin J.(2019), *Aerothermal Optimization of a Ribbed U-Bend Cooling Channel Using the Adjoint Method*. International Journal of Heat and Mass Transfer.

[7] Ansys Fluent 12.0/12.1 Documentation

https://www.afs.enea.it/project/neptunius/docs/fluent/index.htm